TDDFT CALCULATIONS FOR EXCITATION SPECTRA OF SOLIDS AND SUPERSTRUCTURES UTILIZING MGGA

BY

ZHENHUA NING

DISSERTATION

Submitted in partial fulfillment of the requirements
for the degree of Doctor of Philosophy in Physics
in the Graduate College of the
University of Illinois at Urbana-Champaign, 2015

Urbana, Illinois

Doctoral Committee:

Professor John D. Stack, Chair
Professor Yia-Chung Chang, Director of Research
Professor André Schleife
Professor Alfred W. Hubler

Abstract

The first principles study plays a very important role in developing new generation of materials, such as organic semiconductors and long polymer chains, as well as understanding of physical properties of nanoparticles , inorganic semiconductors and semiconductor alloys. In this work, we start from the Kohn-Sham one-particle equation Schrödinger equation and solve it by expanding its eigenfunctions in terms of the linear augmented-slater-type orbits(LASTO) under full potential with the exchange-correlation potential functional given by meta-generalized gradient approximation(mGGA). Our theoretical results were compared to WIEN2K's, and good agreement was obtained. As the application, we apply TDDFT plus mGGA to calculate optical spectra for bulk solids. The result shows good agreement with experimental data.

III-V ternary alloys $A_xB_{1-x}C$ are promising materials for optoelectronic, high-speed electronic and microwave applications, such as infrared emitting diodes and detectors, high electron mobility transistors, heterojunction bipolar transistors, quantum-dot lasers, modulators and ultrafast switches. We adopted the TDDFT theory and the cluster averaging method to compute the spectra of III-V ternary alloys with arbitrary concentration x. We find great agreement between theoretical and experimental data. The success of this method is mainly because that we approximate the transition matrix elements by the LDA p-matrix elements via (mGGA) which contains the singularity of the type $f_{XC,00}(\mathbf{q}) \sim 1/q^2$ as $q \to 0$. Thus, Our studies provide some insight into the theoretical calculation of optical spectra of semiconductor alloys.

Acknowledgments

I wish to express my sincere gratitude to my advisor Prof. Yia-Chung Chang for his guidance, assistance and encouragement over the years.

I am also grateful to Dr. Ching-Tarng Liang for years of collaboration, discussion, encouragement, and providing WIEN2K data.

I acknowledge generous support from Research Center for Applied Sciences, Academia Sinica in Taiwan. Having access to their computational facility has been a great benefit to this research as well. I would like to thank Dr. Tung-Han Hsieh for his help on technical issues.

I also place on record, my sense of gratitude to one and all, who directly or indirectly, have lent their hand and encourage me to strive towards my goal.

Finally, I would like to acknowledge with my deepest appreciation, the support and love of my family. You're the source of my strength.

Table of Contents

List of Tables

List of Figures

List of Abbreviation

BSE	Bethe-Salpeter Equation
BZ	Brillouin Zone
CP	Critical-point
DFT	Density Functional Theory
HK	Hohenberg-Kohn
KS	Kohn-Sham
IBZ	Irreducible Brillouin Zone
LAPW	Linearized augmented-plane-wave
LASTO	Linearized Augmented Slater-type Orbital
LDA	Local Density Approximation
LMTO	Linearized muffin-tin-orbital
mGGA	meta-Generalized Gradient Approximation
MT	muffin tin
OTM	optical transition matrix
SO	Spin-orbit
TDDFT	Time-dependent Density Functional Theory
TDLDA	Time-dependent local density approximation

Chapter 1

Introduction

The first principles study plays a very important role in developing new generation of materials, such as organic semiconductors and long polymer chains, as well as understanding of physical properties of nanoparticles, inorganic semiconductors and semiconductor alloys. Because of inorganic semiconductors, the large scale integration becomes reality, and high-performance computer, smart phone and radio come into people's life. Nanoparticles are predicted to be the basis of another industrial revolution due to a wide range of potential applications in biomedicine, cosmetics, food packaging, clothing, and so on. R. Lam etc. [1] proved that nanodiamond based biomedical device could be used to deliver chemotherapy drugs to cancer cells without the negative effects of current delivery agents. The potential devices including organic light-emitting diodes [2,3], organic photovoltaic cells [4,5] and organic transistors [6,7] are the application of fundamental properties of organic semiconductors. A common characteristic of above materials is that they are complex many-body systems. The research of them has to take into account the interaction of particles carefully and accurately. One can't build simple models to explain them easily. Therefore, the development of them requires accurate and efficient theoretical models using ab initio methods.

The difficulty in solving a many-body system is that the Schrodinger equation is hardly soluble. W. Kohn etc. brought a breakthrough to this field when they developed the density functional theory(DFT) [8,9]. This theory uses the charge density as the basic variable and minimizes the energy with respect to the density by variational principle. It converts the many-body Schrodinger equation into a easy and soluble Kohn-Sham equation with an effective potential, a summation of the external potential, the Hartree potential and the exchange-correlation potential V_{xc}. To this extent, it's a theoretically exact method to solve a ground state problem if the form of V_{xc} is known. Unfortunately, the exchange-correlation potential doesn't have an analytic form, thus a good approximation must be used during the self-consistent solving of the Kohn-Sham equation, like local density approximation(LDA) [9], generalized gradient approximation(GGA) [10–12] or meta-generalized gradient approximation(mGGA) [13–17]. Besides this, this exact theory is just a ground state theory. The eigenvalues gotten from it are not so accurate, except for the total ground state energy is correct. Likewise, these values represent neither the genuine electron addition or subtraction energies nor

the neutral excitation energies in the corresponding interacting many-body system, and their differences are NOT excitation energies. However, physically meaningful quantities can be constructed based on the Kohn-Sham eigenfunctions and eigenvalues by some advanced approaches, such as GW approximation [18], time-dependent density functional theory(TDDFT) [19] and the Bethe-Salpeter equation(BSE) [20–26].

In this work, we pay our attention to the interaction of external electro-magnetic field with electron-hole excitations in materials since they are very demanding in technological applications. As was mentioned above, DFT doesn't solve excitation states, so an advanced method is required to fulfill this job. Therefore, we adopt time-dependent density functional theory to calculate excited states that we are interested in. The Kohn-Sham eigenfunctions are expanded in terms of the linear augmented-slater-type orbits(LASTO) [27–30] under full potential since LASTO method uses less number of basis functions than linearized augmented plane waves (LAPW) method [32] so that it speeds up the computation and can be easily scaled to systems with large number of particles without losing accuracy and efficiency significantly. For the exchange-correlation, F. Tran and P. Blaha's approximation [14] is used to do the self-consistent run to get the expansion coefficients of eigenfunctions.

This dissertation is organized as follows. In Chapter 2, a brief introduction to DFT is given first. The V_{xc} has to be approximated directly and indirectly in terms of the density and/or its derivatives. Since DFT can't solve excitation states, TDDFT is then explained in detail as a alternative. To compare the computational results later, BSE is also introduced briefly in this chapter. To see the shortcoming of LDA, the Kohn-Sham one-particle equation is solved under this approximation in Chapter 3. We also compare the band structures of some materials to those computed by the commercial package WIEN2K [46] to show the accuracy of our LASTO package. Then, in Chapter 4, we compute band structures using mGGA and see the impressive improvement of band gaps. The comparison to WIEN2k is aslo done in this chapter. As the application, we apply TDDFT under mGGA to bulk solids, semiconductors and alloys in Chapter 5 and 6. We see that mGGA shows great advantages over LDA, like correct band gaps in alloys so that one doesn't need to use the expensive GW calculation and deal with the zone folding problem. The optical spectra here support the application of mGGA. The Chapter 7 shows the application of BSE under mGGA, as a direct comparison to TDDFT. The computational parameters and details are explained and listed in the latter three chapters.

Chapter 2

Time-Dependent Density Functional Theory

To study optical properties of a novel material, it's inevitable to solve the many-body Schrodinger equation given by

$$\left[-\frac{\hbar^2}{2m_e}\sum_i \nabla_i + \widehat{H}_{Hartree} + V_{ext} + V_{core}\right]\Psi(\{\vec{r}_i\}) = E\Psi(\{\vec{r}_i\})\,, \tag{2.1}$$

where

$$\widehat{H}_{Hartree} \equiv \frac{1}{2}\sum_{i\neq j}\frac{e^2}{|\vec{r}_i - \vec{r}_j|}, \qquad V_{ext} = \sum_{i,I}\frac{Z_I e^2}{|\vec{r}_i - \vec{R}_I|}\,, \tag{2.2}$$

and

$$V_{core} = -\sum_I \frac{\hbar^2}{2M_I}\nabla_I + \frac{1}{2}\sum_{I\neq J}\frac{Z_I Z_J e^2}{|\vec{R}_I - \vec{R}_J|}\,, \tag{2.3}$$

for interacting electrons and nuclei. Here $\Psi(\{\vec{r}_i\})$ is the many-electron eigenfunction corresponding to the eigenenergy E, where $\vec{r}_i$ is the combination of spatial and spin coordinators for electrons with mass m_e and charge e, provided total N electrons, and the upper case variable $\vec{R}_I$ denotes the coordinators for nuclei with mass M_I and charge Z_I. Due to the Born-Oppenheimer approximation [33], the nuclear kinetic energy can be ignored. Therefore, the effect of the nuclei can be treated as a fixed external potential to electrons. Obviously, this equation can't be solved analytically due to the interaction of electrons. So a simple approach is to approximate this potential as some effective potential, i.e., to use independent-electron approximation. The first one to do so is D. R. Hartree [34] who thought that every electron moved in the average field of other electrons and nuclei. This is the Hartree approximation. Thus, the Schrodinger equation can be decoupled into a set of one-particle Schrodinger equation which is solvable. In this way, the many-electron eigenfunction $\Psi(\{\vec{r}_i\})$ doesn't obey the Fermi-Dirac statics. In 1930, Fock [35] developed Hartree approximation by writing the wave function as a Slater determinant which satisfied the anti-symmetrization required by the Fermi-Dirac statics. This is the so-called Hartree-Fock approximation. However, Hartree-

Fock equations are hard to solve and can only be solved in some special cases, like the homogeneous electron gas, and requires too much computational resource. Although independent-electron approximation is simple and easy, it's insufficient to describe the real electrons' movement. Furthermore, both methods require to describe the wave function $\Psi(\{\vec{r}_i\})$ precisely which is a demanding task in a many-body system.

In 1927, Thomas [36] and Fermi [37] proposed an alternative method which used the density of electrons as the basic variable. They defined the total energy of a system approximately as a functional of the local density at any given point, and didn't consider exchange and correlation between electrons. The later was revised by Dirac who added exchange, which also used the local approximation, to the functional. Although this approximation is too crude and has only limited success in computational physics, it is a breakthrough to solving the Schrodinger equation given above, and shows people how density functional theory(DFT) works. In 1964, Hohenberg and Kohn [8] constructed the powerful density functional theory based on Thomas-Fermi approximation. Now let's take a look at this beautiful theory.

2.1 Density Functional Theory

Instead of using the many-body wave functions, density functional theory determines physical quantities, like total energy, in terms of the exact ground state density based on two Hohenberg-Kohn theorems [8]. The first theorem states that there's a one-to-one mapping between a given external potential $V_{ext}(\mathbf{r})$ and the ground state electron density $n_0(\mathbf{r})$ for any interacting electrons system. This can be proved easily as the following. Given an external potential of an interacting system, it's Hamiltonian is given by

$$\widehat{H} = \widehat{T} + \hat{U}_{int}(\mathbf{r}) + \hat{V}_{ext}(\mathbf{r})\,, \tag{2.4}$$

where $\widehat{T}$ is the kinetic energy operator and U_{int} includes all internal interaction and potential. Assume that the ground state wave function is Ψ_0 with corresponding eigenenergy E_0. Then we have

$$E_0 = \langle\Psi_0|\widehat{H}|\Psi_0\rangle = \langle\Psi_0|\widehat{T} + U_{int}(\mathbf{r})|\Psi_0\rangle + \int V_{ext}(\mathbf{r})n_0(\mathbf{r})d\mathbf{r}\,. \tag{2.5}$$

Now consider another external potential $V'_{ext}(\mathbf{r})$ which differs $V_{ext}(\mathbf{r})$ by only a constant. Assume it generates the same ground state electron density $n_0(\mathbf{r})$. The corresponding Hamiltonian is similar to $\widehat{H}$ given by

$$\widehat{H}' = \widehat{T} + U_{int}(\mathbf{r}) + V'_{ext}(\mathbf{r})\,. \tag{2.6}$$

Since both external potentials are different, the Hamiltonian can't be the same, i.e., the ground state Ψ_0' of $\widehat{H}'$ is different from Ψ_0. The corresponding eigenenergy E_0' is of the form given by

$$E_0' = \langle \Psi_0' | \widehat{H} | \Psi_0' \rangle = \langle \Psi_0' | \widehat{T} + U_{int}(\mathbf{r}) | \Psi_0' \rangle + \int V_{ext}'(\mathbf{r}) n_0(\mathbf{r}) d\mathbf{r} \,. \tag{2.7}$$

Obviously, Ψ_0' is not the ground state of $\widehat{H}$. According to the Rayleigh-Ritz minimal principle, we get

$$\begin{aligned} E_0 &< \langle \Psi_0' | \widehat{H} | \Psi_0' \rangle = \langle \Psi_0' | \widehat{H}' | \Psi_0' \rangle + \int [V_{ext}(\mathbf{r}) - V_{ext}'(\mathbf{r})] n_0(\mathbf{r}) d\mathbf{r} \\ &= E_0' + \int [V_{ext}(\mathbf{r}) - V_{ext}'(\mathbf{r})] n_0(\mathbf{r}) d\mathbf{r} \,. \end{aligned} \tag{2.8}$$

Similar analogous for the state Ψ_0 leads to the inequality given by

$$E_0' < E_0 + \int [V_{ext}'(\mathbf{r}) - V_{ext}(\mathbf{r})] n_0(\mathbf{r}) d\mathbf{r} \,. \tag{2.9}$$

Sum both sides of Eqs. (2.8) and (2.9) separately and obtain

$$E_0' + E_0 < E_0 + E_0' \,. \tag{2.10}$$

The above contradiction shows that the first theorem is true.

The second theorem says that the total energy of a interacting electron system can be defined as a functional of the density, and that the exact ground state density gives the global minimum of this functional which is just the exact ground state energy. The former part of this theorem is easy to understand. The total energy is the expectation value of the Hamiltonian in Eq. (2.4). Assume that its ground state is Ψ_0 and the corresponding ground state density is $n_0(\mathbf{r})$. Then the total ground state energy is given by

$$E_0 = \langle \Psi_0 | \widehat{H} | \Psi_0 \rangle = \frac{1}{2} \int |\nabla \Psi_0|^2 d\mathbf{r} + \int [U_{int}(\mathbf{r}) + V_{ext}(\mathbf{r})] n_0(\mathbf{r}) d\mathbf{r} \,. \tag{2.11}$$

Here the first term is the kinetic energy which is a functional of the wave function Ψ_0 which, in turn, is a functional of the density $n_0(\mathbf{r})$. We can see that other terms are also functional of the density. This tells that the total energy is a functional of the density. Now let's consider an arbitrary state Ψ which is different from the ground state Ψ_0, then the density $n(\mathbf{r})$ must be different from $n_0(\mathbf{r})$. According to the Rayleigh-Ritz minimal principle, we obtain

$$E_0 < \langle \Psi | \widehat{H} | \Psi \rangle = E \,. \tag{2.12}$$

Therefore the exact ground state energy minimizes the total energy functional and gives the ground state wave function. Hohenberg and Kohn separated the long-range Coulomb interaction from U_{int} and wrote the total energy in the form of functional given by

$$E_0[n_0(\mathbf{r})] = G[n_0(\mathbf{r})] + \frac{1}{2}\int \frac{n_0(\mathbf{r})n_0(\mathbf{r}')}{|\mathbf{r}-\mathbf{r}'|}d\mathbf{r}d\mathbf{r}' + \int V_{ext}(\mathbf{r})n_0(\mathbf{r})d\mathbf{r}\,. \tag{2.13}$$

where $G[n_0(\mathbf{r})]$ includes the kinetic energy, all internal interaction and potential energy except for the classic Coulomb energy, and the second term is the classic Coulomb energy, also called Hartree energy.

Armed with Hohenberg-Kohn theorems, one still can't solve the many-body Schrodinger equation easily since it needs the knowledge of $G[n_0(\mathbf{r})]$ which isn't easy to obtain. The advantage of these theorems is that the density becomes the basic variable which requires less detail than the wave function, and that one can write the Hamiltonian as a functional in terms of the density. In 1965, Kohn and Sham [9] reduced this difficulty by their ansatz.

2.2 The Kohn-Sham Theory

In the Kohn-Sham theory [9], a non-interacting electrons system is chosen to have the same density $n_0(\mathbf{r})$ and the effective potential, which includes the Hartree potential, the external potential and the exchange-correlation potential, of the interacting electrons system. Firstly, the functional $G[n_0(\mathbf{r})]$ is written as

$$G[n_0(\mathbf{r})] = T[n_0(\mathbf{r})] + E_{xc}[n_0(\mathbf{r})]\,. \tag{2.14}$$

where $T[n_0(\mathbf{r})]$ is the kinetic energy of the non-interacting electrons system and $E_{xc}[n_0(\mathbf{r})]$ is the exchange-correlation energy of the interacting system. Then the total energy functional can be rewritten as

$$E_0[n_0(\mathbf{r})] = T[n_0(\mathbf{r})] + \frac{1}{2}\int \frac{n_0(\mathbf{r})n_0(\mathbf{r}')}{|\mathbf{r}-\mathbf{r}'|}d\mathbf{r}d\mathbf{r}' + \int V_{ext}(\mathbf{r})n_0(\mathbf{r})d\mathbf{r} + E_{xc}[n_0(\mathbf{r})]\,. \tag{2.15}$$

The stationary points of $E_0[n_0(\mathbf{r})]$ give the equations which are satisfied by $n_0(\mathbf{r})$. Since the total number of electrons is constant, the constraint on the variation is given by

$$n_0(\mathbf{r}) = \int \delta n_0(\mathbf{r})d\mathbf{r}\,. \tag{2.16}$$

Therefore, the density can be obtained by solving the one-particle Schrodinger equation

$$\left[-\frac{\hbar^2}{2m_e}\nabla + V_{eff}(\mathbf{r})\right]\psi_i(\mathbf{r}) = \epsilon_i\psi_i(\mathbf{r})\,, \tag{2.17}$$

where

$$V_{eff}(\mathbf{r}) = H_{Hartree}(\mathbf{r}) + V_{xc}(\mathbf{r}) + V_{ext}(\mathbf{r})\,, \tag{2.18}$$

and the exchange-correlation potential

$$V_{xc}(\mathbf{r}) = \frac{\delta E_{xc}[n_0(\mathbf{r})]}{\delta n_0(\mathbf{r})}\,. \tag{2.19}$$

Here $\psi_i(\mathbf{r})$ is called Kohn-Sham orbitals corresponding to eigenenergy ϵ_i. The density is constructed by Kohn-Sham orbitals as

$$n_0(\mathbf{r}) = \sum_i^N |\psi_i(\mathbf{r})|^2\,, \tag{2.20}$$

where N is the total number of electrons. Now one can theoretically solve all many-body problems through solving the Kohn-Sham one-particle Schrodinger equation self-consistently as the flow chart in Fig. 2.1. However, technically speaking , the exchange-correlation potential $V_{xc}(\mathbf{r})$ needs more work before this self-consistent job is done since the exact form of $V_{xc}(\mathbf{r})$ is unknown. This will be explained in the next section.

2.3 The Exchange-Correlation Energy

An important part of the effective potential is the exchange-correlation potential V_{xc} which can be constructed from the exchange-correlation energy, whose exact form remains unknown, by Eq. (2.19). Thus, an appropriate approximation must be chosen for it. In general, people think that E_{xc} is a functional in terms of the density. For a system with slowly varying density, $E_{xc}(\mathbf{r})$ at a spacial position $\mathbf{r}$ can be approximated as a function of the density at $\mathbf{r}$. People call this approximation the local density approximation(LDA). It can generate reliable results for electronic structure properties for many materials. However, serious problems exist in it, for instance, underestimated band gaps compared to experiment for semiconductors and insulators [38,39]. Based on LDA, people import the gradient of the density into the dependence of E_{xc}, that is, expanding E_{xc} in terms of the density and the gradient of it $|\nabla n|$. This is the so called generalized-gradient approximation(GGA). Although the GGA has notable improvement over LDA in many cases, it

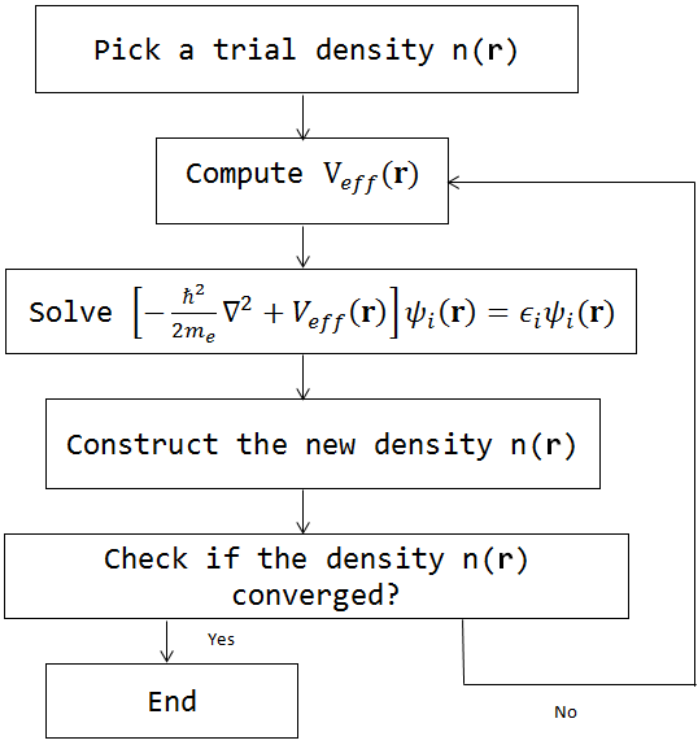

Figure 2.1: Flow chart describing the self-consistent procedure for solving the one-particle Kohn-Sham equation.

also has the underestimated band gap problem. To improve the lower band gaps, the kinetic energy density (and sometimes $\nabla^2 n$) is adopted, in addition to the GGA ingredients, in the expansion of E_{xc}. This extended approximation is named meta-GGA(mGGA). Our current work mainly focuses on LDA and mGGA.

2.3.1 The Local Density Approximation

LDA is a very simple approximation which expands the exchange-correlation(XC) energy $E_{xc}(\mathbf{r})$ only in terms of the density $n(\mathbf{r})$ for a slowly varying density system, such as sp-bonded metals and molecules with covalent and/or ionic bonding. For this kind of system, the XC energy is of the form given by

$$E_{xc}(\mathbf{r}) = \int n(\mathbf{r})\varepsilon_{xc}(\mathbf{r})d\mathbf{r}\,, \tag{2.21}$$

where $\varepsilon_{xc}(\mathbf{r})$ is the exchange-correlation energy per particle of a uniform electron gas with the same density $n(\mathbf{r})$. Here the exchange energy per particle $\varepsilon_x(\mathbf{r})$ has an analytical form, while the correlation energy per particle $\varepsilon_c(\mathbf{r})$ uses the approximation proposed by L. Hedin etc. [40]. It will be explained in section 3.2.

Besides of the LDA by L. Hedin etc., people can also use the one proposed by S.H. Vosko etc. [41]. The latter uses Pade approximant to interpolate the monte-carlo results for para- and ferro-magnetic limits of Ceperley and Alder [42].

2.3.2 The meta-Generalized Gradient Approximation

To improve accuracy, meta-generalized gradient approximation(mGGA) expands the exchange-correlation potential not only in terms of the density and the gradient of the density $\nabla n_\sigma(\mathbf{r})$ but also in terms of the kinetic energy density $\tau(\mathbf{r})$ and(or) $\nabla^2 n_\sigma(\mathbf{r})$, so it is of the form given by

$$E_{xc} = \int \varepsilon_{xc}(n(\mathbf{r}), |\nabla n(\mathbf{r})|, \tau(\mathbf{r}), \nabla^2 n_\sigma(\mathbf{r}))d\mathbf{r}\,, \tag{2.22}$$

where $\tau(\mathbf{r})$ is the kinetic energy density. Here one can think that depending on the kinetic energy density is an implicit way to expand in terms of the density since it can be constructed by the wavefunctions which, in turn, is a functional of the density. This work uses the one proposed by Tran and Blaha(TB09) [14] to solve the Kohn-Sham one particle equation (2.17) self-consistently. TB09 will be elaborated in section 4.1.

2.4 Time-Dependent Density Functional Theory

As was mentioned before, density functional theory is a ground state theory whose eigenvalues are not accurate and their difference are NOT excitation energies, that is, the Kohn-Sham approach can't properly describe excitations. This problem can be solved by the time-dependent density functional theory(TDDFT). Runge and Gross [19] proved that, for a fixed initial state, there existed a one-to-one mapping between the time-dependent external potential and the time-dependent density. Firstly, they showed that two time-dependent external potential, which differed by more than a time-dependent constant, generated different time-dependent current densities. Then they proved that different time-dependent current densities correspond to different time-dependent densities through the continuity equation.

Thus one can study a system by adding a weak perturbation to it, then measures the response of it to the perturbation. This measurement yields excitonic information about electrons and holes, and about their interaction, i.e., the electronic structure of the system. Theoretically, the information is contained in the complex dielectric function $\varepsilon_M(\mathbf{q}, \omega)$ via the response function χ given by

$$\frac{1}{\varepsilon_M(\mathbf{q}, \omega)} = 1 + \frac{4\pi e^2}{q^2}\chi_{00}(\mathbf{q}, \omega)\,, \tag{2.23}$$

where the response function χ can be built from the frequency-dependent, dynamical exchange-correlation(XC) kernel $f_{XC}(\mathbf{r}, \mathbf{r}', t - t')$ defined as

$$f_{XC}(\mathbf{r}, \mathbf{r}', t - t') = \frac{\delta^2 E_{XC}[n]}{\delta n(\mathbf{r}, t)\delta n(\mathbf{r}', t')} = \frac{\delta V_{XC}[n(\mathbf{r}, t)]}{\delta n(\mathbf{r}', t')}\,, \tag{2.24}$$

where $V_{XC}[n(\mathbf{r}, t)]$ is the time-dependent XC potential which is a functional of the particle density $n(\mathbf{r}, t)$. Therefore, the key quantity is the time-dependent XC potential V_{XC} or its functional derivative, the XC kernel f_{XC}.

For the most general case, one doesn't know whether there exists a scalar XC kernel f_{XC} within linear response theory. E.K.U. Gross et al. [53] derived a formal representation of f_{XC} in terms of response functions. Consider an unperturbed inhomogeneous interacting electronic system under the static external potential $v_{ext}(\mathbf{r})$. This is a static problem, so one can easily use DFT to compute the ground state density $n_0(\mathbf{r})$. Then add a small perturbing potential $v_1(\mathbf{r}, \omega)e^{-i\omega t}$ to the system. The corresponding density response $n_1(\mathbf{r}, \omega)$ is given by

$$n_1(\mathbf{r}, \omega) = \int d\mathbf{r}' \chi(\mathbf{r}, \mathbf{r}', \omega) v_1(\mathbf{r}', \omega). \tag{2.25}$$

R. van Leeuwen [54] proved that there exists a non-interacting system which can reproduce a given interacting evolution $n(\mathbf{r}, t)$, so one can reproduce the system above by a noninteracting electronic system under an effective single-particle potential $v_0^{eff} + v_1^{eff}$. Here v_1^{eff} is defined by the equation

$$v_1^{eff}(\mathbf{r}, \omega) = v_1(\mathbf{r}, \omega) + \int \frac{n_1(\mathbf{r}', \omega)}{\mathbf{r} - \mathbf{r}'} d\mathbf{r}' + v_{1XC}(\mathbf{r}, \omega), \tag{2.26}$$

where $v_{1XC}(\mathbf{r}, \omega)$ is the XC potential. Thus the response density can be calculated by

$$n_1(\mathbf{r}, \omega) = \int d\mathbf{r}' \chi_{KS}(\mathbf{r}, \mathbf{r}', \omega) v_1^{eff}(\mathbf{r}', \omega), \tag{2.27}$$

where $\chi_{KS}(\mathbf{r}, \mathbf{r}', \omega)$ is the Kohn-Sham(KS) response function of the ground state of the noninteracting system corresponding to v_1^{eff}. In the linear response theory, one seek a solution of the XC potential $v_{1XC}(\mathbf{r}, \omega)$ of the form

$$v_{1XC}(\mathbf{r}, \omega) = \int d\mathbf{r}' f_{XC}(\mathbf{r}, \mathbf{r}', \omega) n_1(\mathbf{r}', \omega). \tag{2.28}$$

According to Eqs. (2.25), (2.26), (2.27) and (2.28), one can easily find that f_{XC} is of the form [53]

$$f_{XC}(\mathbf{r}, \mathbf{r}', \omega) = \chi_{KS}^{-1}(\mathbf{r}, \mathbf{r}', \omega) - \chi^{-1}(\mathbf{r}, \mathbf{r}', \omega) - \frac{e^2}{|\mathbf{r} - \mathbf{r}'|}, \tag{2.29}$$

where $\chi(\mathbf{r},\mathbf{r}',\omega)$ is the longitudinal density response function and $\chi_{KS}(\mathbf{r},\mathbf{r}',\omega)$ is its single-particle Kohn-Sham counterpart. The existence of the inverse of them is discussed by E. Runge et al and E.K.U. Gross [19]. Here $\chi_{KS}(\mathbf{r},\mathbf{r}',\omega)$ can be built by the KS orbitals. This will be discussed later.

The attraction of TDDFT is that it provides a powerful tool for studying excitations in these systems which can't be done within the ordinary static density functional theory(DFT). One key quantity in TDDFT is the XC kernel $f_{XC}(\mathbf{r},\mathbf{r}',t-t')$ which includes all the many-body effects beyond the Hartree approximation. In principle, excitonic effects and self-energy correction are exactly contained in the TDDFT equations if the exact XC potential V_{xc} and kernel f_{xc} are used [55]. Almost all calculations under TDDFT today use an "adiabatic local density approximation(ALDA)" [56] to evaluate V_{XC} since the exact form of the XC potential as a functional of the density remains unknown. It assumes that the time-dependent XC potential has the functional form of the static local density approximation (LDA), only with a time-dependent density

$$V_{XC}^{ALDA}(n(\mathbf{r},t)) = \frac{d}{dn}\epsilon_{XC}^{h}(n(\mathbf{r},t))\,, \tag{2.30}$$

where $\epsilon_{XC}^{h}(n(\mathbf{r},t))$ is the XC energy of the homogeneous electron gas of density $n(\mathbf{r},t)$. One has to admit that ALDA leads to many useful results. However, the XC potential has a memory(nonlocality in time), i.e., $V_{XC}[n(\mathbf{r},t)]$, which depends on the density on the earlier times t'. The memory implies nonlocality of the XC potential in space since a small volume element of the system located at $\mathbf{r}$ was situated at a different position $\mathbf{r}'$. Due to the nonlocality, the direct electron-hole interaction effects are only partially described in finite systems, and in general still out of reach of todays TDDFT calculations for solids [55]. In 1994, Dobson found that results obtained from the use of LDA violate the so called harmonic potential theorem (HPT) [57]. To conquer this problem, one has to adopt the adiabatic meta-generalized gradient approximation expands(AMGGA) [58]. The XC energy within MGGA is written as

$$E_{XC} = \int d\mathbf{r}\epsilon_{XC}[n(\mathbf{r}),\nabla n(\mathbf{r}),\tau(\mathbf{r})]\,, \tag{2.31}$$

where ϵ_{XC} is the XC energy density functional. Here Voorhis and Scuseria's approximation(VS98) [15] is used, so the functional doesn't depend on the laplacian of the density. The second functional derivative of

E_{XC} gives,

$$\begin{aligned} f_{XC}(\mathbf{r},\mathbf{r}') &= \frac{\partial^2\epsilon_{XC}}{\partial n^2}(\mathbf{r})\delta(\mathbf{r}-\mathbf{r}') - \left[\nabla\frac{\partial^2\epsilon_{XC}}{\partial n\partial\nabla n}\right](\mathbf{r})\delta(\mathbf{r}-\mathbf{r}') - \left[\nabla_i\frac{\partial^2\epsilon_{XC}}{\partial\nabla_i n\partial\nabla_j n}\right](\mathbf{r})\nabla_j\delta(\mathbf{r}-\mathbf{r}') \\ &+ \frac{\partial^2\epsilon_{XC}}{\partial n\partial\tau}(\mathbf{r})\frac{\partial\tau(\mathbf{r})}{\partial n(\mathbf{r}')} + \frac{\partial^2\epsilon_{XC}}{\partial n\partial\tau}(\mathbf{r}')\frac{\partial\tau(\mathbf{r}')}{\partial n(\mathbf{r})} - \nabla\frac{\partial^2\epsilon_{XC}}{\partial n\partial\tau}(\mathbf{r})\frac{\partial\tau(\mathbf{r})}{\partial n(\mathbf{r}')} - \nabla'\frac{\partial^2\epsilon_{XC}}{\partial n\partial\tau}(\mathbf{r}')\frac{\partial\tau(\mathbf{r}')}{\partial n(\mathbf{r})} \\ &+ \int d\mathbf{r}''\frac{\partial^2\epsilon_{XC}}{\partial\tau^2}(\mathbf{r}'')\frac{\partial\tau(\mathbf{r}'')}{\partial n(\mathbf{r})}\frac{\partial\tau(\mathbf{r}'')}{\partial n(\mathbf{r}')} + \int d\mathbf{r}''\frac{\partial\epsilon_{XC}}{\partial\tau}(\mathbf{r}'')\frac{\partial^2\tau(\mathbf{r}'')}{\partial n(\mathbf{r})\partial n(\mathbf{r}')}\,. \end{aligned} \tag{2.32}$$

Ignoring those terms, which don't have the singularity of the type $f_{XC,00}(\mathbf{q}) \sim 1/q^2$ as $q \to 0$ in the reciprocal space, in the above equation, one can obtain

$$f^{xc}_{\mathbf{G},\mathbf{G}'} \approx -\overline{\frac{\partial\epsilon_{xc}}{\partial\tau}}\chi^{-1}_{KS,s}(\mathbf{G},\mathbf{G}')\,, \tag{2.33}$$

where

$$\chi_{KS}(\mathbf{r},\mathbf{r}') = \sum_{\nu,\nu',\sigma}\frac{f_\nu - f_{\nu'}}{\epsilon_\nu - \epsilon_{\nu'} + i\eta}\psi^*_{\nu,\sigma}(\mathbf{r})\psi_{\nu',\sigma}(\mathbf{r})\psi^*_{\nu',\sigma}(\mathbf{r}')\psi_{\nu,\sigma}(\mathbf{r}')\,, \tag{2.34}$$

and $\psi_{\nu,\sigma}$, ϵ_ν and f_ν are KS wave functions, KS eigenenergies and occupation numbers with quantum numbers ν and spin quantum number σ.

2.5 The Bethe-Salpeter Approach

One can also solve the excitonic effects by the Bethe-Salpeter approach [20–26]. The Bethe-Salpeter approach(BSA), which is a Green's-function-based many-body approach, solves the Bethe-Salpeter equation for the irreducible vertex function $\tilde{\Gamma}$ given by

$$\tilde{\Gamma}(12,3) = \delta(1,2)\delta(1,3) + iW(1,2)\int d6\int d7G(1,6)G(7,2)\tilde{\Gamma}(67,3), \tag{2.35}$$

where G is the Green's function and $W(1,2) = \int d3\varepsilon^{-1}(1,3)v_{ee}(3,2)$ is the screened electron-electron interaction. Here v_{ee} is the bare Coulomb potential. Then, insert the vertex $\tilde{\Gamma}$ into the response function given by

$$\chi(1,2) = \tilde{\chi}(1,2) + \int d3\int d4\tilde{\chi}(1,3)v_{ee}(3,4)\chi(4,2), \tag{2.36}$$

where the irreducible response function is given by

$$\tilde{\chi}(1,2) \equiv -i \int d3 \int d4 G(1,3) G(4,1) \tilde{\Gamma}(34,2). \tag{2.37}$$

Finally, one gets the response function (thus for ε) by the way described above. This approach interprets correctly the excitonic effects for a wide range of materials. In 2002, P. Pusching et al. used the BSA to calculate the excitonic effects. However, the BSA needs the GW correction, that they didn't use, to generate accurate result. Moreover,the GW correction is hard to implement. On the other hand, the BSA doesn't explain how vertex corrections and dynamical screening to be included consistently [55]. In addition to these, BSA is a big time consumer during computation. For a big system, it takes more than one month to finish. This work focuses on TDDFT which can reduce the time to several hours.

Chapter 3

Solve the Kohn-Sham One-Particle Equation with LDA

In general, a Schrodinger equation can be solved either directly or indirectly depending on the potential. For simple potentials, like those of the simple harmonic oscillator, 1D infinite well and the hydrogen atom, people can solve them easily and successfully. While for a complicated potential, like the Kohn-Sham's effective potential mentioned before, one has to expand the eigenfunctions in terms of a complete basis set. The simplest basis set is the plane waves set with a big shortcoming that it requires huge number of plane waves to describe the activities of electrons in the region around the atoms that demands very heavy computational resources. So a modified model was proposed by Slater who thought that people should treat the region around the atomic nuclei different from the region outside of it [59]. He used atomic-like functions in this region while he still kept the plane waves outside. Based on this, Anderson proposed the linearized augmented plane waves (LAPW) method [32]. This work uses the Linear augmented Slater-type orbital method which was developed by Davenport et al. [27–30] based on Andersons linearized augmented plane waves (LAPW) method but used Slater type orbitals in the interstitial region.

3.1 The Linear augmented Slater-type orbital method

In this method, a unit cell is divided into the muffin-tin region, the non-overlapping spheres around the atoms, and the interstitial region, see Fig.3.1. The basis functions $\psi_{\mathbf{k},N}(\mathbf{r})$ are chosen differently in these two regions. In the interstitial region, basis functions are chosen to be the Slater-type orbitals(STO) centered at site $\{R_i\}$ given by [60]

$$\psi_{\mathbf{k},N}(\mathbf{r}) = \frac{1}{\sqrt{N_c}} \sum_i e^{i\mathbf{k}\cdot\mathbf{R}_i} \phi_N(\mathbf{r}_i), \tag{3.1}$$

where N is composite index of n,l,m, N_c is the number of atoms in the unit cell and

$$\phi_N(\mathbf{r}_i) = r_i^{n-1} e^{-\varsigma r_i} Y_L(\widehat{\mathbf{r}}_i). \tag{3.2}$$

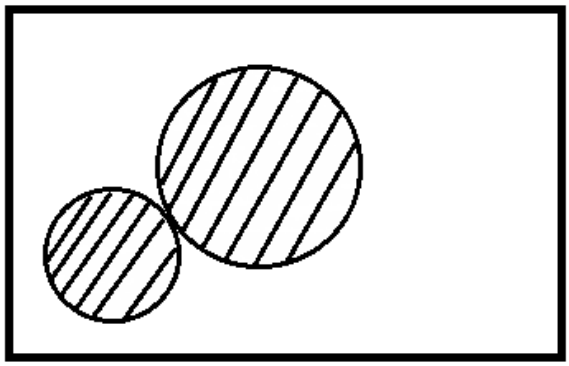

Figure 3.1: The division of a 2D unit cell into the sphere region and the interstitial region, where the shaded spheres are the sphere region where the atomic nuclei is located.

where L is the composite index of l,m and $\mathbf{r}_i = \mathbf{r} - \mathbf{R}_i$. The Fourier transform of the Slater-type orbital can be computed analytically given by

$$\tilde{\phi}_N(\mathbf{q}) = \frac{4\pi(-i)^l Y_L(\widehat{\mathbf{q}})}{V_c} \int_0^\infty d\mathbf{r} j_l(qr) r^{n+1} e^{-\zeta_{nl} r}, \tag{3.3}$$

where V_c is the volume of the unit cell and $\mathbf{q} = \mathbf{k} + \mathbf{G}$, where $\mathbf{G}$ denotes a reciprocal lattice vector. The parameter ζ controls the width of the orbital;large ζ gives more localized function than small ζ. STOs are used because they decay exponentially as the distance from the nuclei and accurately describe the long-range overlap between atoms compared to plane waves, see Fig. 3.2. While within the *ith* muffin-tin sphere, the basis functions are linear combinations of atomic radial functions and spherical harmonics given by

$$\begin{aligned} \psi_{\mathbf{k},N}(\mathbf{r}) &= \frac{1}{\sqrt{N_c}} \sum_{\tilde{N}} e^{i\mathbf{k}\cdot\mathbf{R}_i} \left[A_{N,\tilde{N}}(\mathbf{k}) u_l(r_i) + B_{N,\tilde{N}}(\mathbf{k}) \dot{u}_l(r_i) \right] Y_L(\hat{\mathbf{r}}_i) \\ &= \frac{1}{\sqrt{N_c}} \sum_{\tilde{N}} e^{i\mathbf{k}\cdot\mathbf{R}_i} \Lambda_{N,\tilde{N}}(r_i) Y_L(\hat{\mathbf{r}}_i) \end{aligned} \tag{3.4}$$

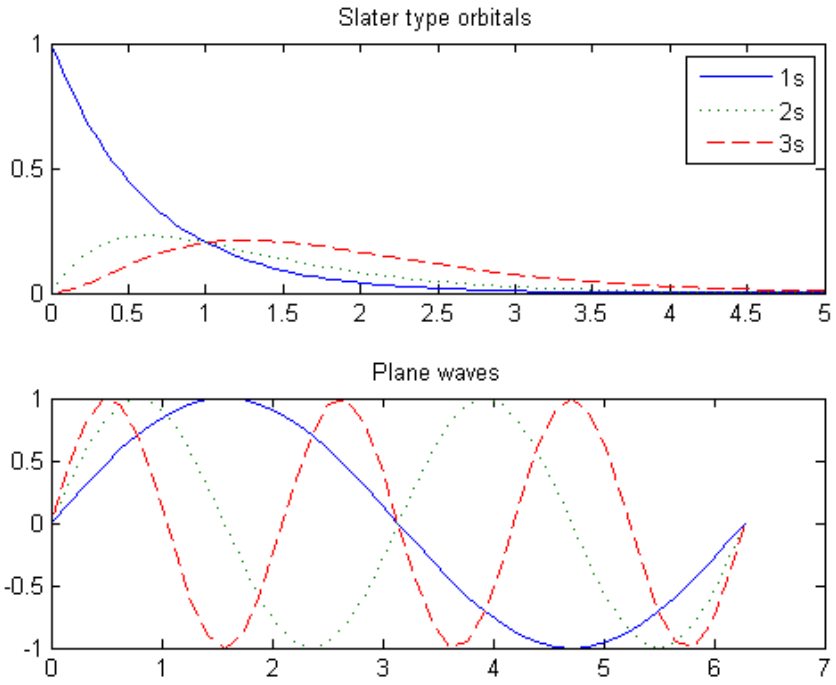

Figure 3.2: Comparison of Slater type orbitals and Plane waves.For STOs, (n=1,l=0),(n=2,l=0) and (n=3,l=0) waves are plotted.

where

$$\Lambda_{N,\tilde{N}}(r_i) = \left[A_{N,\tilde{N}}(\mathbf{k})u_l(r_i) + B_{N,\tilde{N}}(\mathbf{k})\dot{u}_l(r_i)\right] , \tag{3.5}$$

and $\tilde{N}$ is a composite index for $\{\tilde{i}, \tilde{l}, \tilde{m}\}$. Here u's are normalized within the spheres,

$$\int_0^{R_s} r^2 u_l^2(r) dr = 1 , \tag{3.6}$$

and u_l and $\dot{u}_l$ are orthogonal,

$$\int_0^{R_s} r^2 u_l(r)\dot{u}_l dr = 0 . \tag{3.7}$$

According to the one-particle Kohn-Sham equation, they should satisfy the radial equations given by

$$\begin{aligned} h_r u_l &= \epsilon u_l \\ h_r \dot{u}_l &= \epsilon \dot{u}_l + u_l , \end{aligned} \tag{3.8}$$

where h_r is the scalar relativistic Hamiltonian,

$$h_r = -\frac{\hbar^2}{2M}\left[\frac{d^2}{dr^2} + \frac{2}{r}\frac{d}{dr} - \frac{l(l+1)}{r^2}\right] - \frac{\hbar^2}{2M}\frac{1}{2Mc^2}\frac{dV_{eff}}{dr}\frac{d}{dr} + V_{eff}\,, \tag{3.9}$$

and $\dot{u}_l$ is the derivative of u_l with respect to ϵ. The effective mass is defined as $M = m[1 + (\epsilon - V)/2mc^2]$. A and B are coefficients to be determined by matching the wave functions and their derivatives inside the spheres and in the interstitial region. Then the Kohn-Sham orbitals are expanded in terms of these basis functions given by

$$\Psi_{\nu\mathbf{k}} = \sum_N C_{\nu\mathbf{k}}(N)\psi_{\mathbf{k},N}(\mathbf{r})\,, \tag{3.10}$$

where ν labels the Kohn-Sham eigenfunctions. Note that $\dot{u}_l$ is adopted in the basis functions. In the augmented plane wave(APW) method [31], the basis function is expanded in terms of only the atomic radial function u_l which depends on energy. Thus one has to guess a initial energy, followed by a self-consistent run to get the true u_l corresponding to the real energy. This costs a lot of computational source and time. In 1975, Andersen [32] proved that the linear combination $\Phi(u, \dot{u})$ of u_l, corresponding to a given arbitrary but fixed energy E_a, and its energy derivative $\dot{u}_l$, matching continuously and differentiably onto the wave functions in the interstitial region, gives energy E with error of order $(E - E_a)^4$ while the difference between $\Phi(u, \dot{u})$ and the correct wave function $\phi(E)$ is order $(E - E_a)^2$. Therefore, this linear combination can reach the correct wave function faster.

3.2 The Local Density Approximation

In LDA, the exchange energy per particle $\varepsilon_x(\mathbf{r})$ has an analytical form given by

$$\varepsilon_x(\mathbf{r}) = -\frac{3}{4}\left(\frac{3}{2\pi}\right)^{2/3}\frac{1}{r_s}\,, \tag{3.11}$$

where the density parameter r_s is defined by

$$r_s = \left[\frac{3}{4\pi n(\mathbf{r})}\right]^{1/3}\,, \tag{3.12}$$

while the correlation energy per particle $\varepsilon_c(\mathbf{r})$ uses the approximation proposed by L. Hedin etc. [40] given by

$$\varepsilon_c(\mathbf{r}) = -\mathcal{C}\left[(1+x^3)\ln\left(1+\frac{1}{x}\right) + \frac{x}{2} - x^2 - \frac{1}{3}\right]\,, \tag{3.13}$$

where the coefficient $\mathcal{C} = 0.045$ and $x = r_s/\mathcal{A}$ with $\mathcal{A} = 21$. Therefore the exchange potential is given by

$$v_x(\mathbf{r}) = -\left(\frac{3}{2\pi}\right)^{2/3} \frac{1}{r_s}\,, \tag{3.14}$$

while the correlation can be obtained by [39]

$$v_c(\mathbf{r}) = -\mathcal{C}\ln\left(1+\frac{1}{x}\right)\,. \tag{3.15}$$

When to solve the Kohn-Sham one particle equation (2.17) self-consistently, Eqs. (3.14) and (3.15) will be used to calculate the effective potential.

3.3 Computational parameters

Now we can compute the band structures for Si,Ge, GaAs, GaP, InAs and InP using LASTO with LDA. All of them are zincblende structures with two atoms in the unit cell. The primitive vectors are chosen to be

$$\begin{aligned} \mathbf{a}_1 &= (0, 0.5, 0.5)a_0, \\ \mathbf{a}_2 &= (0.5, 0, 0.5)a_0, \\ \mathbf{a}_3 &= (0.5, 0.5, 0)a_0\,, \end{aligned} \tag{3.16}$$

where a_0 is the lattice constants(atomic units) at low temperature(0K), listed in Table 3.1. These values were extrapolated at 0K, see Ref. [45]. For the position of the atoms in the unit cell, We put one atom at (0,0,0)a_0,

Table 3.1: Lattice constants(atomic units)at low temperature(0K)

Si	Ge	GaAs	InAs	InP
10.23287	10.65617	10.65239	11.42151	11.06624

Table 3.2: Electron configuration(EC), the muffin tin radius and the atomic number(Z) of elements.

	Si	Ge	Ga	P	As	In
Z	14	32	31	15	33	49
EC	[Ne]$3s^2 3p^2$	[Ar] $3d^{10}4s^2 4p^2$	[Ar]$3d^{10}4s^2 4p^1$	[Ne]$3s^2 3p^3$	[Ar]$3d^{10}4s^2 4p^3$	[Kr]$4d^{10}5s^2 5p^1$
r_s	2.215	2.3	2.306	2.242	2.425	2.52

Table 3.3: Optimized ζ values

Si		Ge		GaAs			
				Ga		As	
3s	1.23514	4s	2.315	4s	1.210614	4s	1.210614
3p	1.95005	4p	2.369	4p	1.513267	4p	1.513267
3d	1.57	3d	1.51	3d	1.913267	3d	1.613267
3s	0.945	4s	1.210	4s	1.815921	4s	1.815921
3p	1.26	4p	1.51	4p	2.269901	4p	2.269901
InAs				InP			
In		As		In		P	
5s	1.411365	4s	1.129092	5s	1.456675	3s	0.874005
5p	1.693638	4p	1.411365	5p	1.748010	3p	1.165340
4d	1.793638	3d	1.411365	4d	2.548010	3d	1.456675
5s	0.940910	4s	1.567818	5s	0.971117	3s	1.311008
5p	1.129092	4p	2.117048	5p	1.165340	3p	1.748010

and the other at $(1/4,1/4,1/4)a_0$. To find the basis set, we need the outermost electron configuration for atoms Si, Ge, Ga, As, P, In, see Table 3.2. From the table, we can determine the basis set for those elements, that is, 3s and 3p for Si, 4s and 4p for Ge, 4s and 4p for Ga, 2s and 2p for P, 4s and 4p for As and 5s and 5p for In. The ζ values for the STOs of the basis set by the rule that the first zeta values are given by $(n+l)/r_s$, then adjust them by matching the band gaps to experimental results. Here n is the principal quantum number, l is the orbital angular momentum quantum number and r_s is the muffin tin radius. The optimized ζ values are listed in Table 3.3. The special $\mathbf{k}$ points in the Brillouin-zone are generated by Monkhorst-Pack special points scheme [61, 62].

3.4 Computational results

Armed with above parameters, band structures and LDA dielectric functions are computed. The results are compared to those calculated by WIEN2K [46] and experimental results.

3.4.1 Band structures

The LDA band structures of Si,Ge, GaAs, InAs and InP are plotted, see Figs.3.3,3.4,3.5,3.6,3.7. The band gaps are listed in Table 3.4. We can see that both LASTO and WIEN2K generate similar band structures although they use different basis set in the interstitial region. From the table, Si's direct gap is lower than the experimental direct gap. This confirms that LDA underestimates band gaps. Moreover, Ge's direct gap is 0ev, while the experiment gap is 0.74ev. The LDA's gap for Ge is inconsistent with the fact that Ge is a

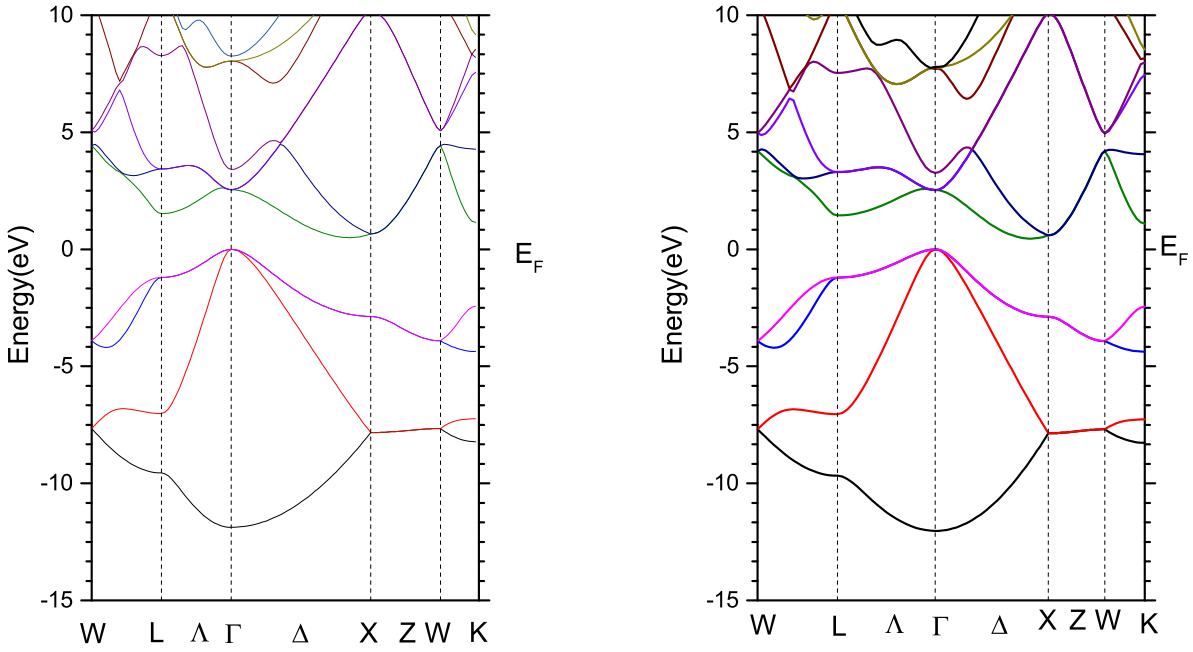

(a) Computed by LASTO

(b) Computed by WIEN2K

Figure 3.3: The LDA band structure of Si

semiconductor.

Table 3.4: Comparison of LDA Band gaps of materials from LASTO, WIEN2K and experiment. Those marked with * are direct band gap while those with ♭ are indirect band gap.

	Si		Ge	GaAs	InAs	InP
LASTO	2.5476_*	$0.4978_♭$	0.0304	0.3590	-0.7179	0.4057
WIEN2K	2.5326_*	$0.4594_♭$	-0.1116	0.3420	-0.4389	0.4870
Exp	3.34^a_*	$1.17^b_♭$	0.898^c_*	1.5191^d	0.4105^e	1.4236^f

[a] Reference [47] [b] Reference [48] [c] Reference [49] [d] Reference [50] [e] Reference [51] [e] Reference [52]

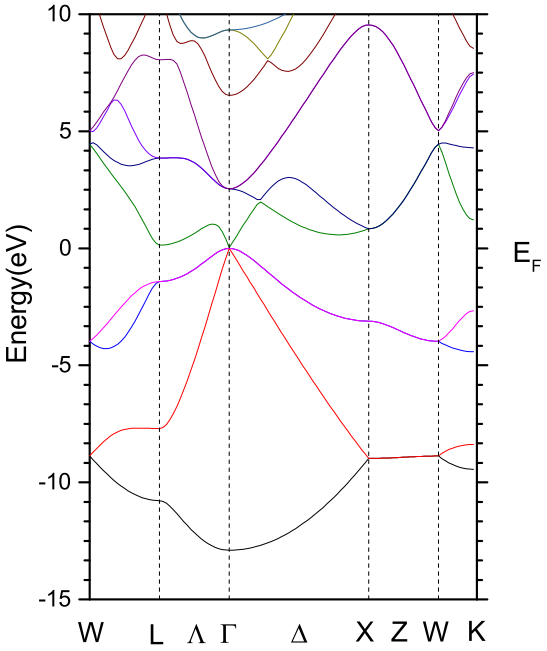

(a) Computed by LASTO

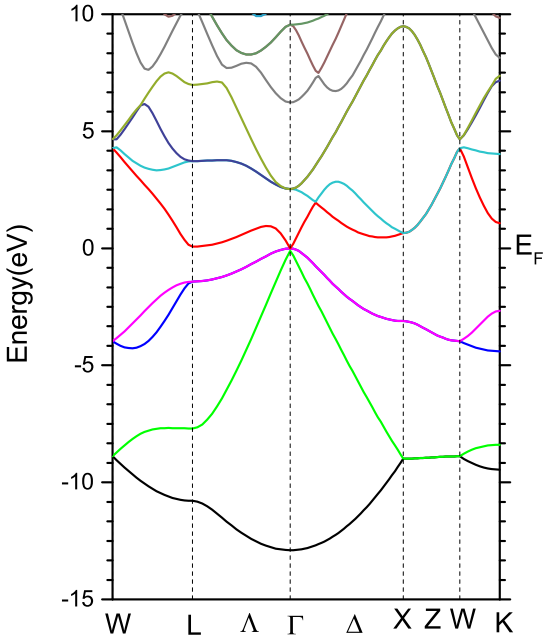

(b) Computed by WIEN2K

Figure 3.4: The LDA band structure of Ge

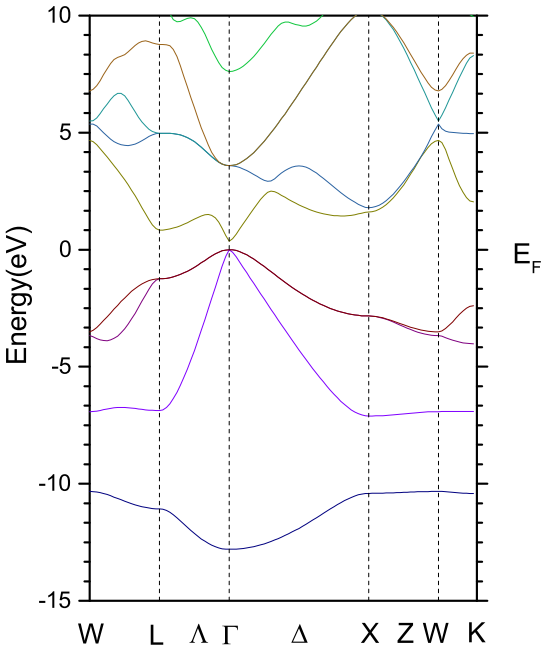

(a) Computed by LASTO

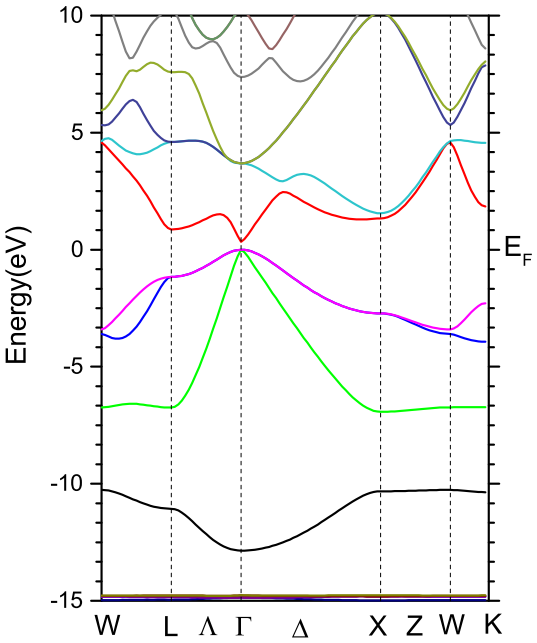

(b) Computed by WIEN2K

Figure 3.5: The LDA band structure of GaAs

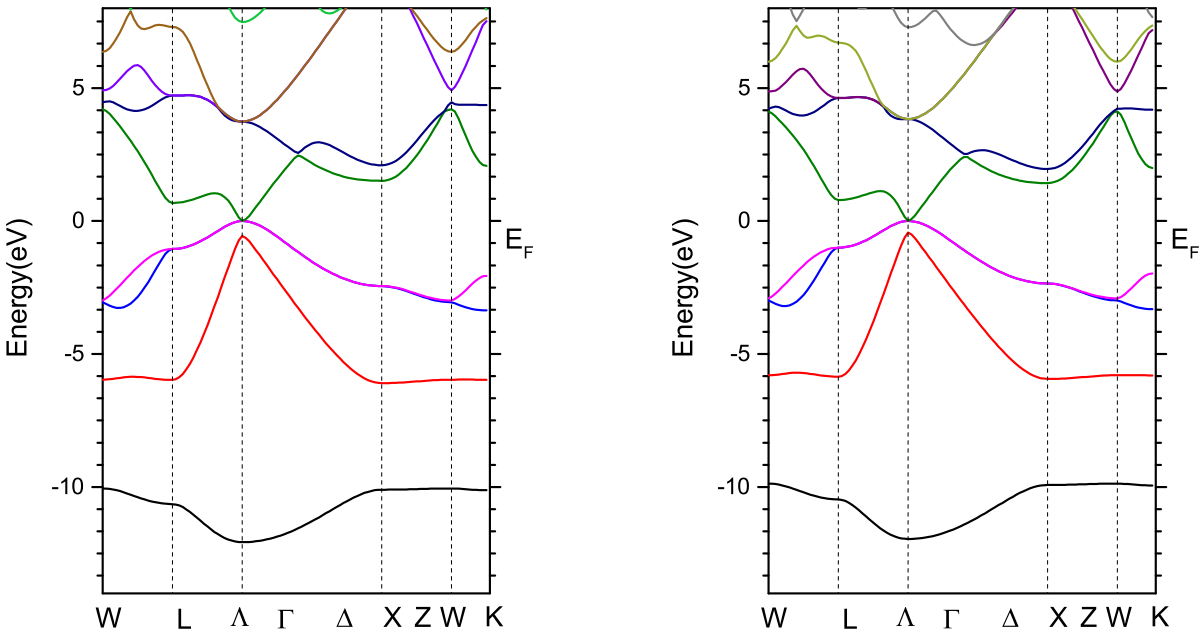

(a) Computed by LASTO

(b) Computed by WIEN2K

Figure 3.6: The LDA band structure of InAs

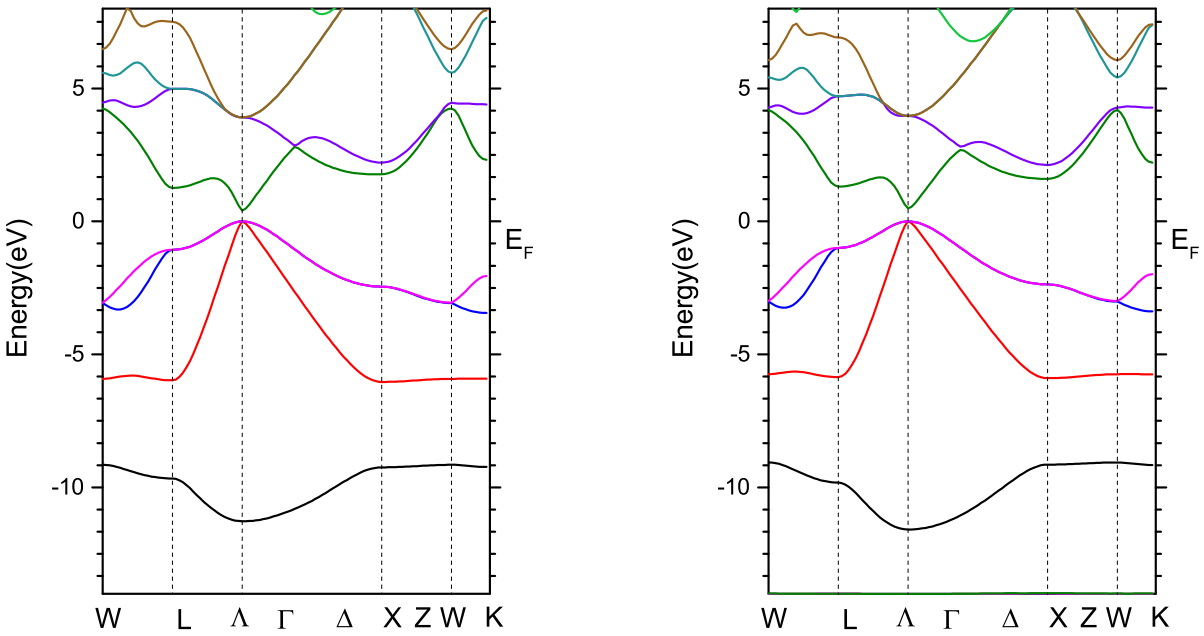

(a) Computed by LASTO

(b) Computed by WIEN2K

Figure 3.7: The LDA band structure of InP

Chapter 4

Solve the Kohn-Sham One-Particle Equation with MGGA

In the previous chapter, we solved the Kohn-Sham One-Particle Equation with LDA and confirmed that LDA leaded to underestimated or even disappeared band gaps, like Si and Ge. This notorious problem can be fixed by meta-generalized gradient approximation(mGGA). A better mGGA, used by most computational package to do self-consistent computation, is the one proposed by Tran and Blaha(TB09) [14] which will be elaborated in section 4.1. Then the implementation of TB09 will be explained in section 4.2. Band structures and gaps calculated by LASTO with TB09 will be listed thereafter.

4.1 The meta-Generalized Gradient Approximation

In TB09, the exchange-correlation energy is expanded in terms of the density, the gradient of the density $n_\sigma(\mathbf{r})$, the kinetic energy density and the laplacian of the density $\nabla^2 n_\sigma(\mathbf{r})$, i.e.,

$$E_{xc} = \int \varepsilon_{xc}(n(\mathbf{r}), |\nabla n(\mathbf{r})|, \tau(\mathbf{r}), \nabla^2 n_\sigma(\mathbf{r}))d\mathbf{r}\,. \tag{4.1}$$

The exchange potential is written as

$$v^{TB}_{x,\sigma}(\mathbf{r}) = cv^{BR}_{x,\sigma}(\mathbf{r}) + (3c-2)\frac{1}{\pi}\sqrt{\frac{5}{12}}\sqrt{\frac{\tau_\sigma(\mathbf{r})}{n_\sigma(\mathbf{r})}}\,, \tag{4.2}$$

where the Becke-Roussel(BR) [43] potential $v^{BR}_{x,\sigma}$ is of the form given by

$$v^{BR}_{x,\sigma}(\mathbf{r}) = -\frac{1}{b_\sigma(\mathbf{r})}\left[1 - e^{x_\sigma(\mathbf{r})} - \frac{1}{2}x_\sigma(\mathbf{r})e^{x_\sigma(\mathbf{r})}\right]\,, \tag{4.3}$$

the kinetic energy density is defined by

$$\tau_\sigma(\mathbf{r}) = \sum_{i,\sigma}^{occp.} |\nabla\psi_{i,\sigma}(\mathbf{r})|^2\,, \tag{4.4}$$

the parameter b is defined by

$$b_\sigma(\mathbf{r}) = \frac{x_\sigma(\mathbf{r})e^{-x_\sigma(\mathbf{r})}}{8\pi n_\sigma(\mathbf{r})}\,, \tag{4.5}$$

and the parameter c depends linearly on the square root of the average of $|n_\sigma(\mathbf{r})|/n_\sigma(\mathbf{r})$ given by [14]

$$c = \alpha + \beta(\frac{1}{\Omega_{cell}}\int_{cell}\frac{|\nabla n_\sigma(\mathbf{r}')|}{n_\sigma(\mathbf{r}')}d^3r')^{1/2}\,, \tag{4.6}$$

where the quantity Ω_{cell} is the unit cell volume and α and β are two free parameters. Here the parameter $x_\sigma(\mathbf{r})$ has to be solved self-consistently by [43]

$$\frac{x_\sigma(\mathbf{r})e^{-2x_\sigma(\mathbf{r})/3}}{x_\sigma(\mathbf{r})-2} = \frac{2}{3}\pi^{2/3}\frac{n_\sigma(\mathbf{r})^{5/3}}{Q_\sigma(\mathbf{r})}\,, \tag{4.7}$$

where

$$Q_\sigma(\mathbf{r}) = \frac{1}{6}\nabla^2 n_\sigma(\mathbf{r}) - 2\gamma D_\sigma(\mathbf{r})\,, \tag{4.8}$$

and

$$D_\sigma(\mathbf{r}) = \tau_\sigma(\mathbf{r}) - \frac{1}{4}\frac{(\nabla n_\sigma(\mathbf{r})^2)}{n_\sigma(\mathbf{r})}\,. \tag{4.9}$$

The parameter $\gamma = 0.8$ is chosen to precisely recover the exchange potential of the uniform electron gas.

During the computation, the kinetic energy constructed by wave functions in Eq. (4.4) is a time consumer. Instead of using this equation, people can compute the kinetic energy density by

$$\tau_\sigma(\mathbf{r}) = \frac{1}{2}\sum_{i,\sigma}^{occp.}|\nabla\psi_{i,\sigma}(\mathbf{r})|^2 = \sum_{i_\sigma\mathbf{k}} f_{i_\sigma\mathbf{k}}\epsilon_{i_\sigma\mathbf{k}}|\psi_{i_\sigma\mathbf{k}}(\mathbf{r})|^2 - V_{\text{eff}}(\mathbf{r})n_\sigma(\mathbf{r}) + \tfrac{1}{4}\nabla^2 n_\sigma(\mathbf{r})\,, \tag{4.10}$$

where $f_{i_\sigma\mathbf{k}}$ is the occupation number. This can be derived based on the one particle Kohn-Sham equation as the following.

$$\begin{aligned}\nabla^2 n_\sigma(\mathbf{r}) &= \sum_{i,\sigma}^{occp.}\left[\psi_{i,\sigma}(\mathbf{r})\nabla^2\psi^*_{i,\sigma}(\mathbf{r}) + \psi^*_{i,\sigma}(\mathbf{r})\nabla^2\psi_{i,\sigma}(\mathbf{r}) + 2|\nabla\psi_{i,\sigma}(\mathbf{r})|^2\right] \\ &= \sum_{i,\sigma}^{occp.}\left[4(V_{\text{eff}}(\mathbf{r}) - \epsilon_{i_\sigma\mathbf{k}})\psi_{i,\sigma}(\mathbf{r})\psi^*_{i,\sigma}(\mathbf{r}) + 2|\nabla\psi_{i,\sigma}(\mathbf{r})|^2\right]\,.\end{aligned} \tag{4.11}$$

TB09 [14] is a very good approximation to produce accurate results well agreed with experiment for a band of solids considered, such as wide band gap insulators, sp semiconductors, and strongly correlated 3d transition-metal oxides. Please note that Tran and Blaha optimized α and β using WIEN2K [46] with the mGGA by matching the band gap of Si to the experiment exactly whereas minimizing the mean absolute relative error for band gaps of other materials. If one needs accurate band gap for other materials, α and β must be readjusted to match the experiment. Please note that TB09 includes only the exchange part. For the correlation part, we use the LDA correlation potential proposed by Pewdew and Wang [44].

4.2 Implementation of TB09

To calculate the exchange-correlation potential, we have to compute the gradient of the density $n_\sigma(\mathbf{r})$ and the kinetic energy density $\tau(\mathbf{r})$ first. Since $\tau(\mathbf{r})$ depends on the laplacian of the density $\nabla^2 n(\mathbf{r})$, this quantity should also be prepared for the calculation. In the interstitial region, LASTO package stores the Fourier coefficients of the density $n(\mathbf{r})$. Thus we can easily get the $\nabla n(\mathbf{r})$ and $\nabla^2 n(\mathbf{r})$ given by

$$\nabla n(\mathbf{r}) = \nabla \sum n(\mathbf{G}) e^{i\mathbf{G}\cdot\mathbf{r}} = \sum [i\mathbf{G} n(\mathbf{G})] e^{i\mathbf{G}\cdot\mathbf{r}} \,. \tag{4.12}$$

$$\nabla^2 n(\mathbf{r}) = \nabla^2 \sum n(\mathbf{G}) e^{i\mathbf{G}\cdot\mathbf{r}} = -\sum [|\mathbf{G}|^2 n(\mathbf{G})] e^{i\mathbf{G}\cdot\mathbf{r}}, \tag{4.13}$$

Inside the muffin tin spheres, LASTO package stores the density in a little complicated way which divides

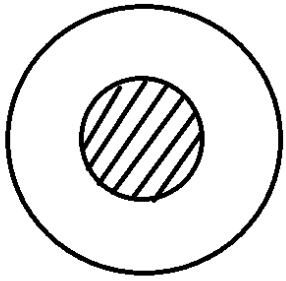

Figure 4.1: The division of a 2D muffin tin sphere. The shaded region is the one with sphereical symmetry while the unshaded region is the shell.

the sphere into a small sphere with spherical symmetry and the shell region between the small sphere and

the muffin tin sphere, see Fig. 4.1. So the density in the small sphere is written as

$$n(\mathbf{r}) = n_{00}(r)Y_{00}\,, \tag{4.14}$$

while in the shell region, the density

$$n(\mathbf{r}) = \sum_l \tilde{n}_l(r)K_l(\mathbf{r}) = \sum_{lm} \widetilde{n}_l(r)c_{lm}Y_{lm}(\mathbf{r}) = \sum_{lm} n_{lm}(r)Y_{lm}(\mathbf{r})\,, \tag{4.15}$$

where $K_l(\mathbf{r})$ is the lattice harmonics which is of the form given by

$$K_l(\mathbf{r}) = \sum_m c_{lm}Y_{lm}(\mathbf{r})\,, \tag{4.16}$$

and

$$n_{lm}(r) \equiv c_{lm}\widetilde{n}_l\,. \tag{4.17}$$

Therefore, $\nabla n(\mathbf{r})$ and $\nabla^2 n(\mathbf{r})$ in the muffin tin sphere can be calculated by the equation given below.

$$\begin{aligned}\nabla_\mu n_{lm}(r)Y_{lm}(\hat{\mathbf{r}}) \quad &= \sqrt{\tfrac{l+1}{2l+3}}C(l,1,l+1|m,\mu,m+\mu)Y_{l+1m+\mu}(\hat{\mathbf{r}})\left(\tfrac{d}{dr}-\tfrac{l}{r}\right)n_{lm}(r)\\ &-\sqrt{\tfrac{l}{2l-1}}C(l,1,l-1|m,\mu,m+\mu)Y_{l-1,m+\mu}(\hat{\mathbf{r}})\left(\tfrac{d}{dr}+\tfrac{l+1}{r}\right)n_{lm}(r)\,,\end{aligned} \tag{4.18}$$

where $\mu = -1, 0, +1$, the gradient of the coefficient $n_{lm}(r)$ is given by

$$\begin{aligned}\left(\frac{d}{dr}-\frac{l}{r}\right)n_{lm}(r) &= B_{i,L}(u'-\frac{l}{r}u)+A_{i,L}(\dot{u}'-\frac{l}{r}\dot{u})\\ \left(\frac{d}{dr}+\frac{l+1}{r}\right)n_{lm}(r) &= B_{i,L}(u'+\frac{l+1}{r}u)+A_{i,L}(\dot{u}'+\frac{l+1}{r}\dot{u})\,,\end{aligned} \tag{4.19}$$

and the coefficient C is the Clebsch-Gordan coefficient defined by,

$$C(J_1J_2J_3|m_1m_2m_3) = (-1)^{J_1-J_2+m_3}\sqrt{2J_3+1}\begin{pmatrix} J_1 & J_2 & J_3\\ m_1 & m_2 & -m_3\end{pmatrix}\,, \tag{4.20}$$

where

$$\begin{pmatrix} j_1 & j_2 & j_3 \\ m_1 & m_2 & m_3 \end{pmatrix} =$$

$$(-1)^{j1+j2+m3}\sqrt{\frac{(j_1+m_1)!\,(j_2+m_2)!\,(j_3+m_3)!\,(j_3-m_3)!\,(j_1-m_1)!\,(j_2-m_2)!}{(j_2-j_1+j_3)!\,(j_1-j_2+j_3)!\,(j_1+j_2-j_3)!\,(1+j_1+j_2+j_3)!}}\sum_k(-1)^k$$

$$\frac{(j_2-j_1+j_3)!\,(j_1-j_2+j_3)!\,(j_1+j_2-j_3)!}{(j_3-j_1-m_2+k)!\,(j_3-j_2+m_1+k)!\,(j_1+j_2-j_3-k)!\,k!\,(j_1-m_1-k)!\,(j_2+m_2-k)!}\,.$$

Here B and A are expansion coefficients of the eigenfunctions of the Hamiltonian in the muffin-tin sphere, defined in section 3.1. The gradient operator ∇_μ is defined in terms of the spherical unit vectors $\hat{\mathbf{e}}_\mu$:

$$\hat{\mathbf{e}}_{+1} = -\frac{\hat{\mathbf{x}}+i\hat{\mathbf{y}}}{\sqrt{2}}, \qquad \hat{\mathbf{e}}_0 = \hat{\mathbf{z}}, \qquad \hat{\mathbf{e}}_{-1} = \frac{\hat{\mathbf{x}}-i\hat{\mathbf{y}}}{\sqrt{2}}, \tag{4.21}$$

i.e.,

$$\nabla_{+1} = -\frac{\partial_x + i\partial_y}{\sqrt{2}}, \qquad \nabla_0 = \partial_z, \qquad \nabla_{-1} = \frac{\partial_x - i\partial_y}{\sqrt{2}}. \tag{4.22}$$

The laplacian $\nabla^2 n(\mathbf{r})$ in the muffin tin sphere is given by

$$\begin{aligned} \nabla^2\rho(\mathbf{r}) &= \sum_l\{[\frac{\partial^2}{\partial r^2}+\frac{2}{r}\frac{\partial}{\partial r}]\widetilde{\rho}_l(r) - \frac{l(l+1)}{r^2}\widetilde{\rho}_l(r)\}K_l(\hat{\mathbf{r}}) \\ &= \sum_{lm}\{[\frac{\partial^2}{\partial r^2}+\frac{2}{r}\frac{\partial}{\partial r}]\widetilde{\rho}_l(r) - \frac{l(l+1)}{r^2}\widetilde{\rho}_l(r)\}c_{lm}Y_{lm}(\mathbf{r})\,, \end{aligned} \tag{4.23}$$

where $K_l(\hat{\mathbf{r}})$ is a eigenfunction of ∇^2 since

$$\nabla^2 = \frac{\partial^2}{\partial r^2}+\frac{2}{r}\frac{\partial}{\partial r}+\frac{1}{r^2}[\frac{1}{sin^2\phi}\frac{\partial^2}{\partial\theta^2}+\frac{cos\phi}{sin\phi}\frac{\partial}{\partial\phi}+\frac{\partial^2}{\partial\phi^2}]\,, \tag{4.24}$$

and

$$[\frac{1}{sin^2\phi}\frac{\partial^2}{\partial\theta^2}+\frac{cos\phi}{sin\phi}\frac{\partial}{\partial\phi}+\frac{\partial^2}{\partial\phi^2}+l(l+1)]Y_{lm} = 0\,. \tag{4.25}$$

Please note that LASTO package usually stores $y = r^2\widetilde{\rho}_l(r)$. When to calculate the laplacian $\nabla^2 n(\mathbf{r})$, one has to use the following equations.

$$\begin{aligned} \frac{\partial}{\partial r}\widetilde{\rho}_l(r) &= \frac{1}{r^3}(\frac{\partial y}{\partial x}-2y) \\ \frac{\partial^2}{\partial r^2}\widetilde{\rho}_l(r) &= \frac{1}{r}[(\frac{\partial^2 y}{\partial x^2}-4y)\frac{1}{r^3}-5\frac{\partial}{\partial r}\widetilde{\rho}_l(r)]\,. \end{aligned} \tag{4.26}$$

The kinetic energy density is usually defined as $|\sum_{lm} \nabla^s_\mu \Lambda_{lm}(r) Y_{lm}(\hat{\mathbf{r}})|^2/2$. However, it is a time consumer to use the definition to construct it directly. Instead of using this definition, one can use Eq. (4.10) to compute the kinetic density.

4.3 Computational parameters

Now Let's compute the band structures for Si,Ge, GaAs, GaP, InAs and InP using LASTO with mGGA. Those parameters in section 3.3, like primitive vectors, basis set, ζ values and k-points, will be used here. Besides of these parameters, one very important parameter is the constant c defined by Eq. (4.6). Here the free parameters α and β will use the same values, -0.012 and 1.023, optimized by Tran and Blaha in Reference [14]. The c's used in LASTO for these bulk materials are listed in Table 4.1.

Table 4.1: Lattice constants c for bulk solids

Si	Ge	GaAs	GaP	InAs	InP
10.65617	10.23287	10.65595	10.2741	11.42533	11.06994

4.4 Compare data with WIEN2K

In this section, we compare the density, the gradient of the density, the laplacian of the density and the kinetic energy density for Si between LASTO and WIEN2K. Our package uses the LASTO method, while WIEN2K uses the LAPW method. Both methods divide the unit cell in the same way: a spherical region and a interstitial region. Let's compare those quantities from both packages in the spherical region first. In the spherical region, datum are stored in terms of the spherical harmonics. The angles are generated by Gaussian quadrature rule, while the radius uses a homogeneous log mesh given by

$$r_i = r_0 e^{(i-1)\Delta x}, \tag{4.27}$$

where $i = 1...N_r$ when N_r of r mesh is used to describe the radial function in the muffin tin(MT) sphere. Here r_0 is determined by the MT radius r_s and N_r with the condition $r_s = r_0 \exp[(N_r - 1)\Delta x]$. To compare, one specific space angle should be specified. Here we use the first space angle, generated by WIEN2K, with $\theta = 0.05754 rad$ and $\phi = 0.16554 rad$. The number of r mesh $N_r = 431$ is used. The datum generated by both packages are plotted in Figs. 4.2, 4.3, 4.4 and 4.5. We can see that both packages generated the

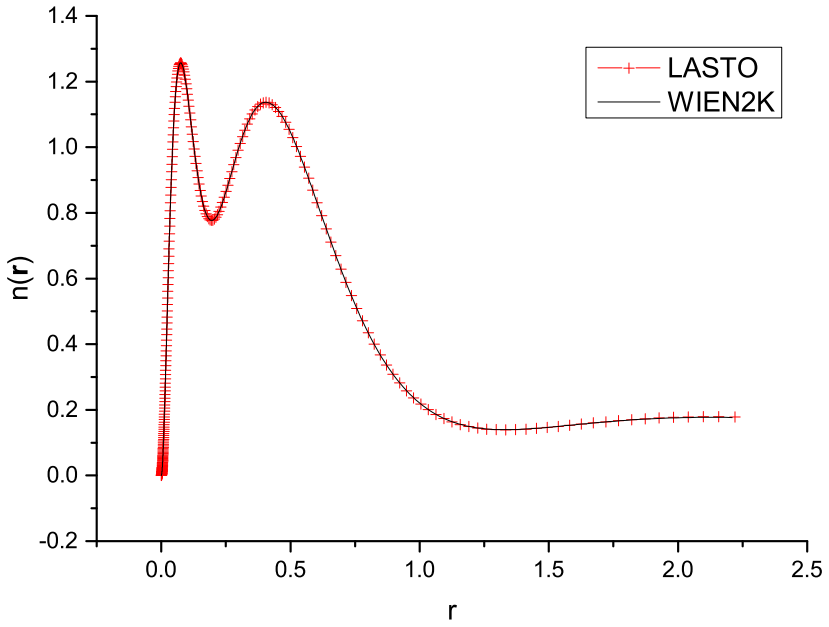

Figure 4.2: Comparison of the density computed by LASTO and WIEN2K

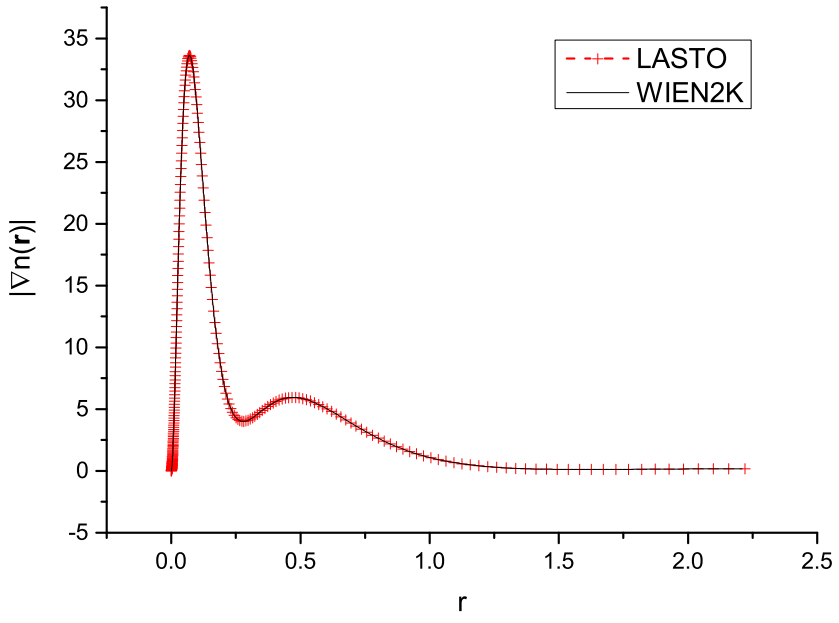

Figure 4.3: Comparison of the gradient of the density computed by LASTO and WIEN2K

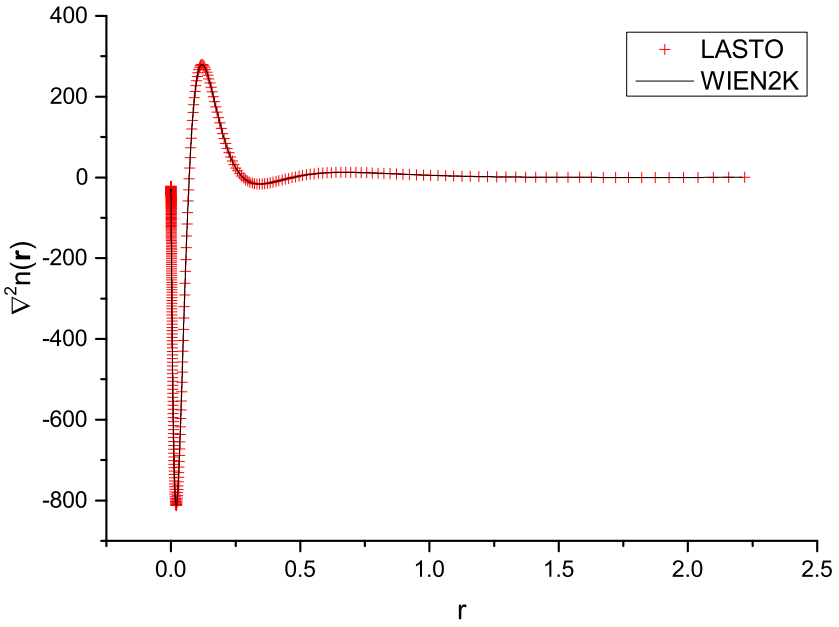

Figure 4.4: Comparison of the laplacian of the density computed by LASTO and WIEN2K

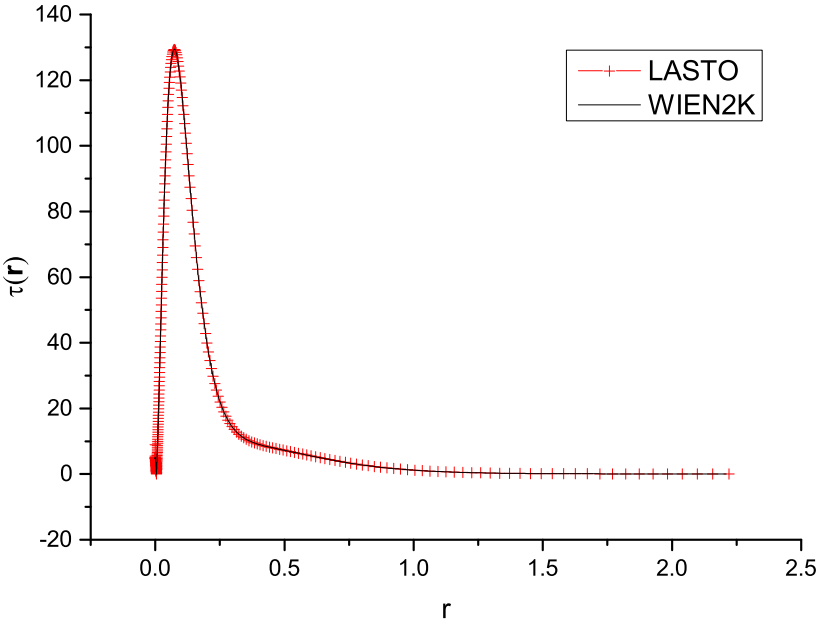

Figure 4.5: Comparison of the kinetic energy density computed by LASTO and WIEN2K

same densities and the same kinetic energy densities. Of course, other quantities related only to the density should also be the same. This is for sure since both packages uses the same basis set in the MT sphere.

The interstitial region uses a homogeneous $32\times32\times32$ cubic mesh with basis vectors defined by Eq. (3.16) for Si. It's better to plot 3D figure for this region. Please note that the density is constructed by the STO's in the full unit cell, so those points reside in the MT spheres are included. To exclude them, we adopt the step function

$$\Theta(\mathbf{r}) = \begin{cases} 1, & \text{if } |\mathbf{r}_i - \mathbf{R}_\alpha| > r_s; \\ 0, & \text{elsewhere.} \end{cases} , \tag{4.28}$$

to do this job. Here $\mathbf{R}_\alpha$ are the position vectors of the atoms with α up to the second neighbors of the unit cell, and $\mathbf{r}_i$ are position vectors of the points of the cubic mesh. When we plot, we choose those datum at $z = 9$, i.e., at xy-plane only. Let's first take a look at what the step function looks like in this plane, see Fig. 4.6. Here a 64×64 mesh points are plotted. We can see that there're two big holes in the center which

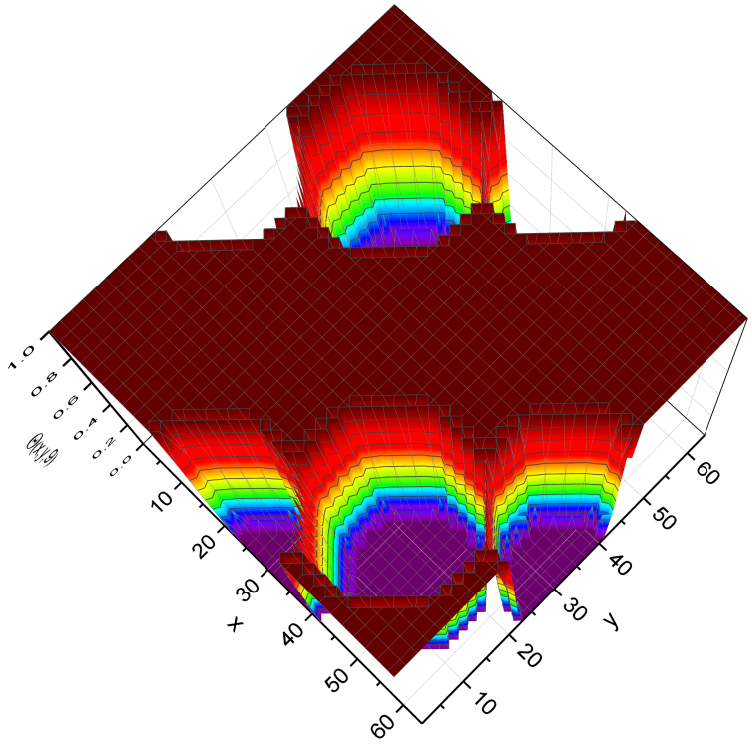

Figure 4.6: Plot the step function in real space

is because of the Si atom sitting at $(0,0,0)a_0$ and its neighbor. The bites on the edge of the figure come

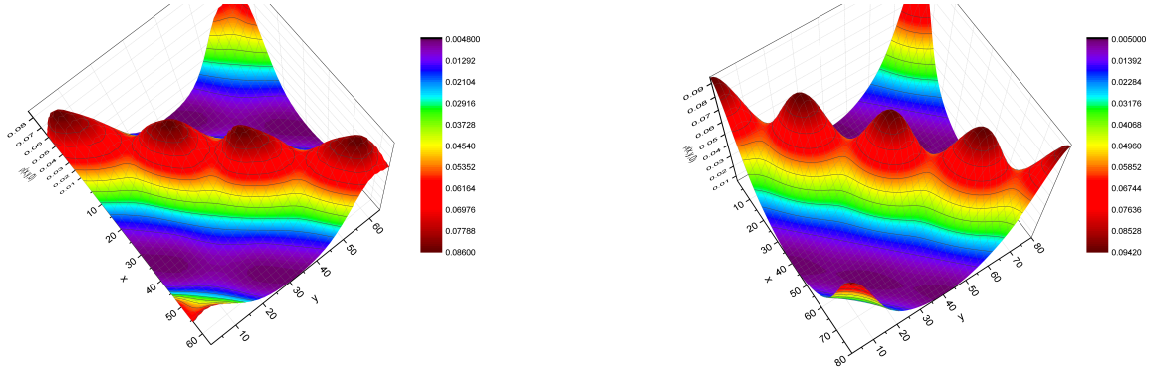

(a) Computed by LASTO (b) Computed by WIEN2K

Figure 4.7: Plot the density of Si in the interstitial region

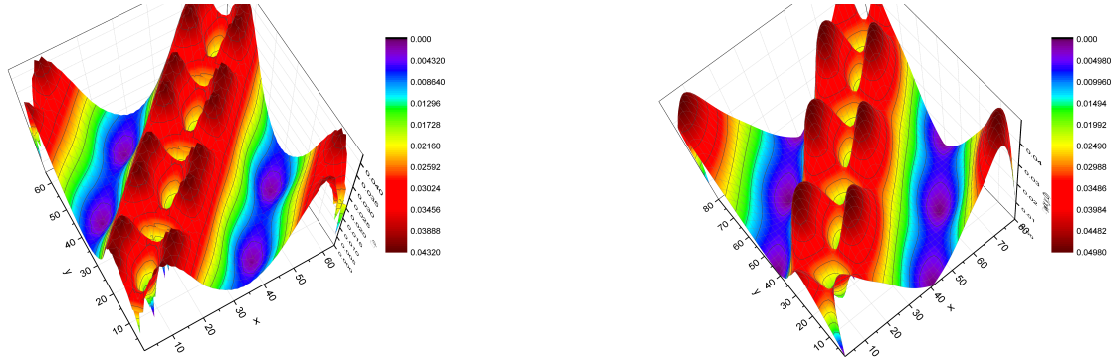

(a) Computed by LASTO (b) Computed by WIEN2K

Figure 4.8: Plot the gradient of the density of Si in the interstitial region

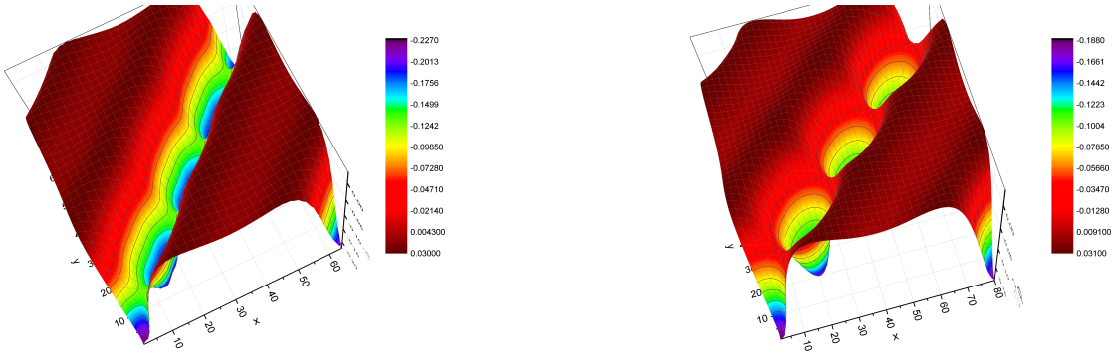

(a) Computed by LASTO (b) Computed by WIEN2K

Figure 4.9: Plot the laplacian of the density of Si in the interstitial region

from the atoms sitting at$(1/4,1/4,1/4)a_0$ and its neighbor. Then let's compare the density, the gradient of the density, the laplacian of the density and the kinetic energy density from LASTO and WIEN2K in the interstitial region, see Figs. 4.7, 4.8, 4.9 and 4.10. We can see that both packages generated similar

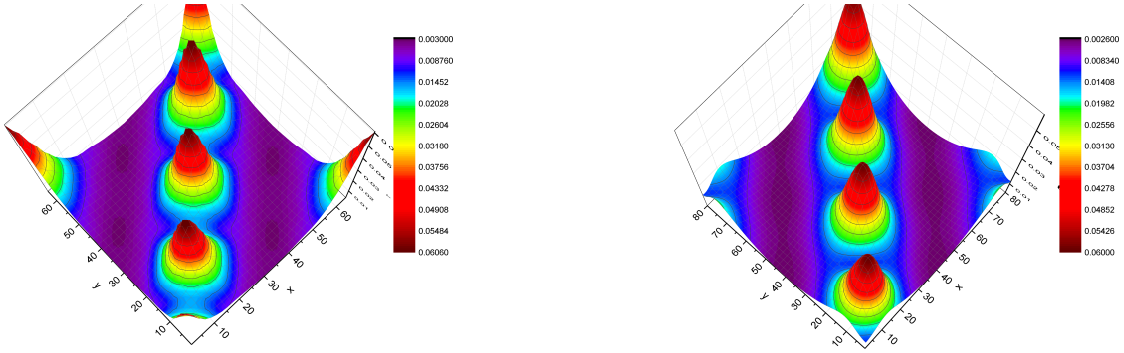

(a) Computed by LASTO

(b) Computed by WIEN2K

Figure 4.10: Plot the kinetic energy density of Si in the interstitial region

quantities in this region with a little difference on the values.

4.5 Computational results

With MGGA, LASTO can generate good band structures with correct band gap compared to experimental results for solids. We can check this for Si,Ge, GaAs, GaP, InAs and InP, and compare the band structures to those computed by WIEN2K, see Figs.4.11,4.12,4.13,4.14,4.15.The band gaps are listed in Table 4.2. We can see that both LASTO and WIEN2K generate similar band structures although they use different basis set in the interstitial region. From the table, we can confirm that MGGA can fix the band gap errors caused by LDA.

Table 4.2: Comparison of mGGA Band gaps of materials from LASTO, WIEN2K and experiment.Those marked with * are direct band gap while those with ♭ are indirect band gap.

	Si		Ge		GaAs	InAs	InP
LASTO	3.0186_*	$1.170_\flat$	1.054_*	$0.8122_\flat$	1.6643	0.4268	1.6497
WIEN2K	3.0987_*	$1.1262_\flat$	1.11_*	$0.8823_\flat$	1.7002	0.696	1.6365
Exp	3.34^a_*	$1.17^b_\flat$	0.898^c_*	$0.744^c_\flat$	1.5191^d	0.4105^e	1.4236^f

[a] Reference [47] [b] Reference [48] [c] Reference [49] [d] Reference [50] [e] Reference [51] [e] Reference [52]

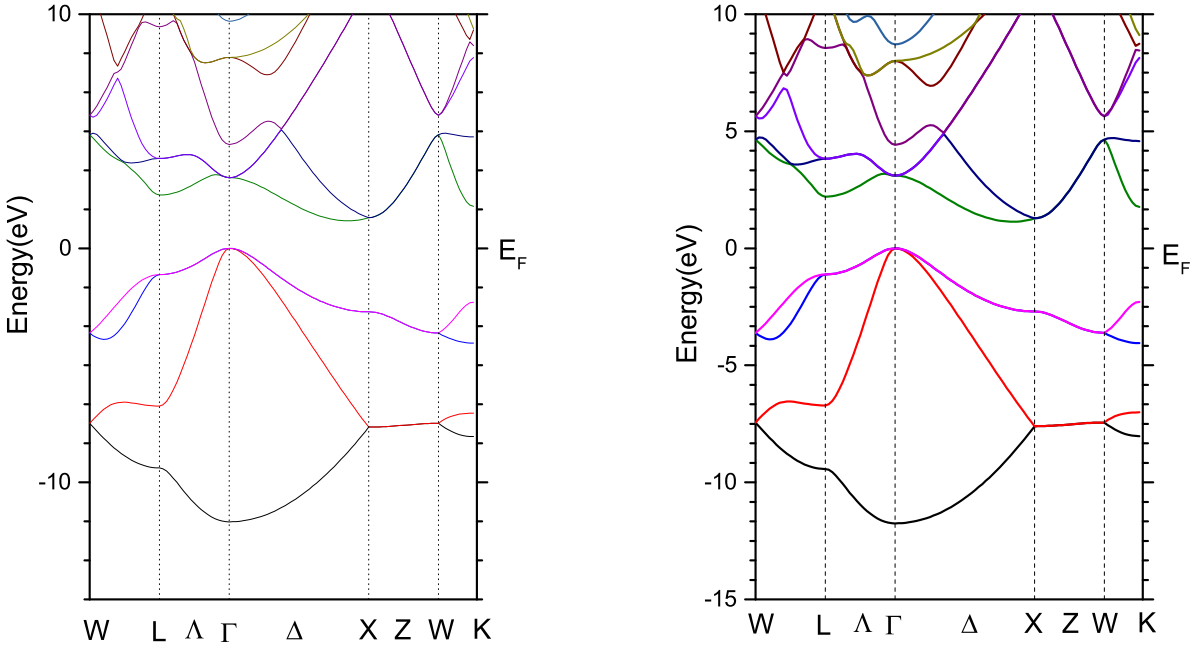

(a) Computed by LASTO

(b) Computed by WIEN2K

Figure 4.11: The MGGA band structure of Si

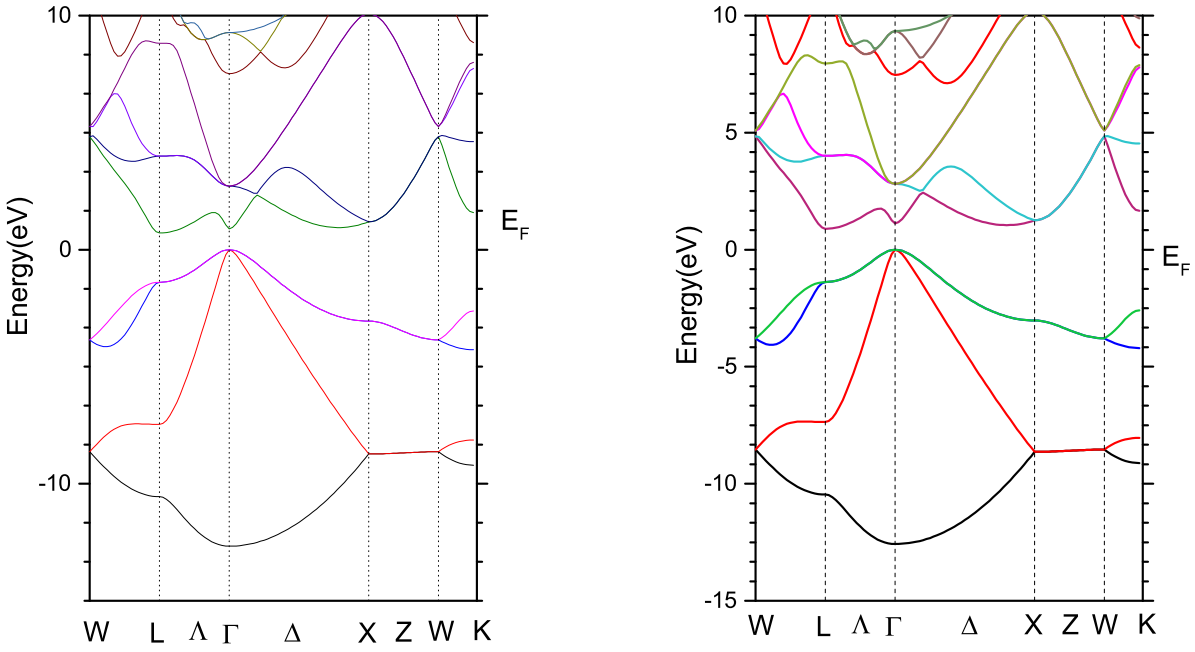

(a) Computed by LASTO

(b) Computed by WIEN2K

Figure 4.12: The MGGA band structure of Ge

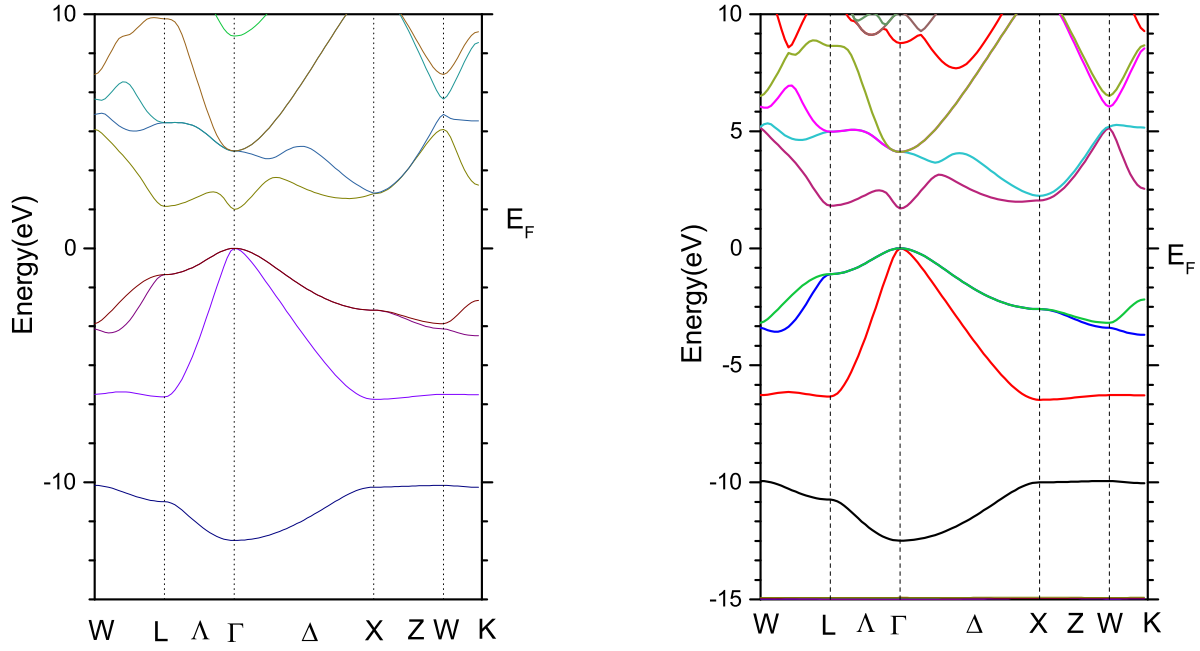

(a) Computed by LASTO

(b) Computed by WIEN2K

Figure 4.13: The MGGA band structure of GaAs

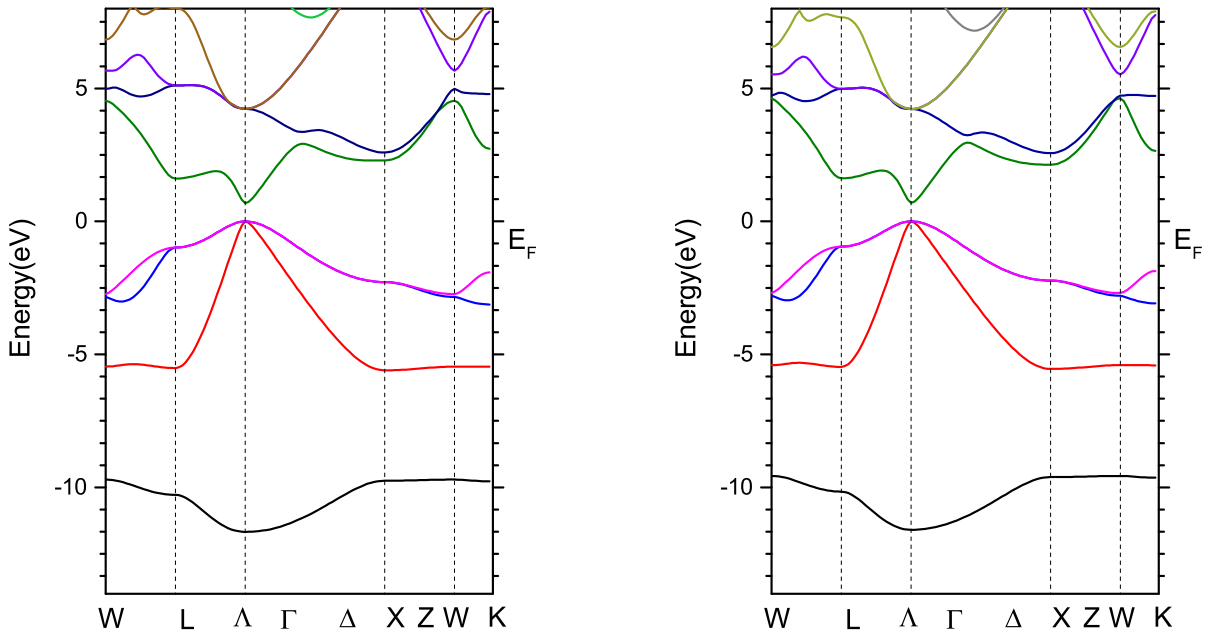

(a) Computed by LASTO

(b) Computed by WIEN2K

Figure 4.14: The MGGA band structure of InAs

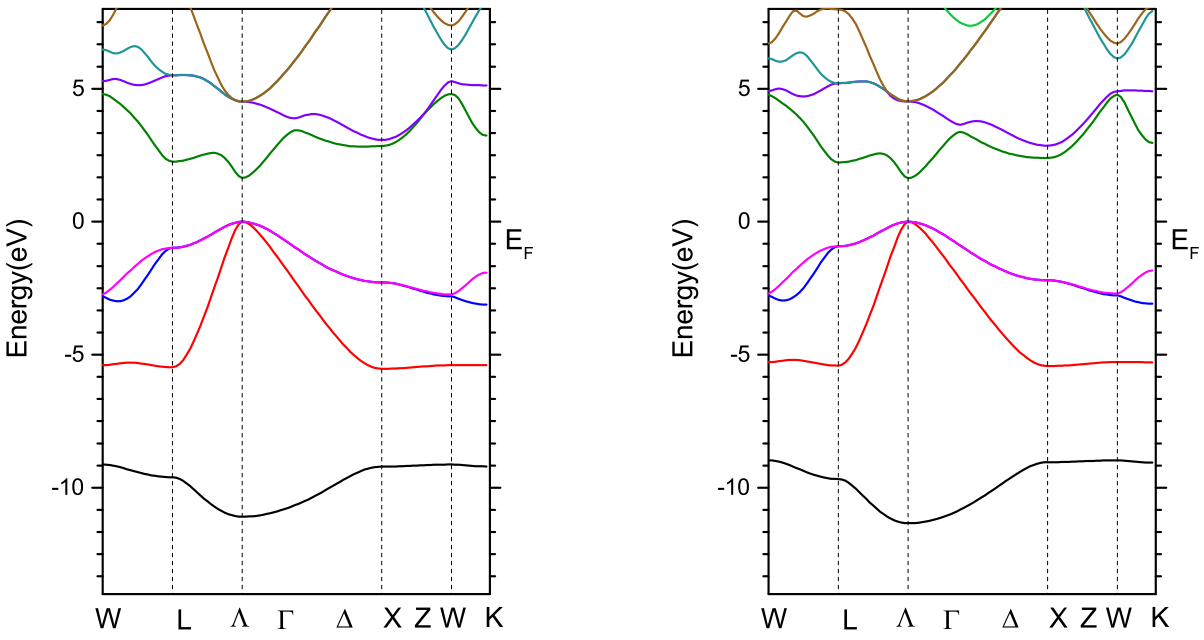

(a) Computed by LASTO

(b) Computed by WIEN2K

Figure 4.15: The MGGA band structure of InP

Chapter 5

Optical properties of Solids with MGGA

In that Kohn-Sham eigenvalues can't represent either the genuine electron addition/subtraction energies or the neutral excitation energies for a interacting many-body system, and their differences are NOT excitation energies, people alternatively use the dielectric function whose poles are located at the exact excitation energies and which can be constructed by Kohn-Sham eigenfunctions and eigenvalues through Eq. (2.23), (2.29), (2.33) and (2.34). The optical spectra of Si,Ge, GaAs, InAs and InP and other materials were calculated by different methods, like the pseudopotential method [63, 64], projector-augmented-wave method [65] and the LAPW method [66]. These results have peaks neither at the correct excitation energies nor with correct strength. It is primarily due to the failure of the independent-particle approximation. However, the XC potential has a memory(nonlocality in time), i.e., $V_{XC}[n(\mathbf{r},t)]$, which depends on the density on the earlier times t'. The memory implies nonlocality of the XC potential in space since a small volume element of the system located at $\mathbf{r}$ was situated at a different position $\mathbf{r}'$. Due to the nonlocality, the direct electron-hole interaction effects are only partially described in finite systems, and in general still out of reach of todays calculations utilizing LDA for solids [55]. In 1994, Dobson found that results obtained from the use of LDA violate the so called harmonic potential theorem (HPT) [57]. A good news is that it has been shown that the inclusion of electron-hole interactions via the time-dependent density functional theory(TDDFT) significantly improves the optical spectra [58].

In this chapter, we first explain how to compute the dielectric function in one-electron picture and including electron-hole interactions effects via TDDFT in the reciprocal space. The implementation of the dielectric function based on the LASTO basis set is shown next. Then, computational details, the convergence tests and results are discussed.

5.1 MGGA dielectric function in Reciprocal space

Now we can start the calculation of the dielectric function for bulk systems. To facilitate the computation, it's better to do the calculation in the reciprocal space to take advantage of the translational invariance in

bulk systems. We know that f_{XC} has a singularity at $\mathbf{G} = 0$ or $\mathbf{G'} = 0$ when $q \to 0$. To avoid this problem during calculation, define a new quantity given by

$$Y_{\mathbf{G},\mathbf{G}'}(\omega) = \delta_{\mathbf{G},\mathbf{G}'} + \frac{1}{4\pi e^2} \lim_{q\to 0} f^{xc}_{\mathbf{G},\mathbf{G}'}(\mathbf{q}) \mid \mathbf{G}+\mathbf{q} \mid\mid \mathbf{G}'+\mathbf{q} \mid, \tag{5.1}$$

where $f^{xc}_{\mathbf{G},\mathbf{G}'}$ can be calculated by $\chi^{KS}_{\mathbf{G},\mathbf{G}'}$ given by [58]

$$f^{xc}_{\mathbf{G},\mathbf{G}'} \approx -\overline{\frac{\partial \epsilon_{xc}}{\partial \tau}} \chi^{-1}_{KS,s}(\mathbf{G},\mathbf{G}') \,. \tag{5.2}$$

Do the same thing to the scalar KS response function, then another new quantity is defined by

$$X_{\mathbf{G},\mathbf{G}'}(\omega) = \lim_{q\to 0} \frac{4\pi e^2 \chi^{KS}_{\mathbf{G},\mathbf{G}'}(\mathbf{q},\omega)}{\mid \mathbf{G}+\mathbf{q} \mid\mid \mathbf{G}'+\mathbf{q} \mid}. \tag{5.3}$$

Here

$$\chi^{KS}_{\mathbf{G},\mathbf{G}'}(\mathbf{q},\omega) \quad = \quad \sum_{\nu,\nu',\sigma} \frac{f_{\nu,\mathbf{k}} - f_{\nu',\mathbf{k}+\mathbf{q}}}{\omega - \epsilon_{\nu',\mathbf{k}} + \epsilon_{\nu,\mathbf{k}} + i\eta} U_{\mathbf{G},\mathbf{G}'} \,, \tag{5.4}$$

where

$$U_{\mathbf{G},\mathbf{G}'} \equiv \langle \Psi_{\nu,\sigma,\mathbf{k}}(\mathbf{r}) \mid e^{-i(\mathbf{G}+\mathbf{q})\cdot\mathbf{r}} \mid \Psi_{\nu',\sigma,\mathbf{k}}(\mathbf{r}) \rangle \langle \Psi_{\nu',\sigma,\mathbf{k}}(\mathbf{r}') \mid e^{i(\mathbf{G}'+\mathbf{q})\cdot\mathbf{r}} \mid \Psi_{\nu,\sigma,\mathbf{k}}(\mathbf{r}') \rangle \,, \tag{5.5}$$

and $\psi_{\nu,\sigma}$, ϵ_ν and f_ν are KS wave functions, KS eigenenergies and occupation numbers with quantum numbers ν and spin quantum number σ. Therefore, the dielectric function can be calculated by the equation below,

$$\varepsilon_M(\omega) = \frac{1}{1 + \{[X^{-1}(\omega) - Y(\omega)]^{-1}\}_{0,0}}. \tag{5.6}$$

This equation can be derived by inserting the above defined quantities into Eq. (2.23) and

$$\chi^{-1} = \chi^{-1}_{KS} - (C + f_{XC}) \,, \tag{5.7}$$

where C is given by

$$C_{\mathbf{G},\mathbf{G}'}(\mathbf{q}) = \frac{4\pi}{\mid \mathbf{G}+\mathbf{q} \mid^2} \delta_{\mathbf{G},\mathbf{G}'} \,. \tag{5.8}$$

Here we need to consider several special cases with $G = 0$ and/or $G' = 0$. When $G = 0$ and $G' = 0$,

$$\begin{aligned} X_{0,0}(\omega) &= \lim_{q\to 0} \frac{4\pi e^2 \widehat{\chi}^{KS}_{0,0}(\mathbf{q},\omega)}{|\mathbf{q}^2|} \\ &= \lim_{q\to 0} \sum_{\nu\nu'\sigma} \frac{4\pi e^2 (f_\nu - f_{\nu'}) \langle \Psi_{\nu\sigma\mathbf{k}}(\mathbf{r}) \mid e^{-i\mathbf{q}\cdot\mathbf{r}} \mid \Psi_{\nu'\sigma\mathbf{k}}(\mathbf{r})\rangle \langle \Psi_{\nu'\sigma\mathbf{k}}(\mathbf{r}') \mid e^{i\mathbf{q}\cdot\mathbf{r}'} \mid \Psi_{\nu\sigma\mathbf{k}}(\mathbf{r}')\rangle}{(\omega - \epsilon_{\nu',\mathbf{k}+\mathbf{q}} + \epsilon_{\nu,\mathbf{k}} + i\eta)|\mathbf{q}^2|} \\ &= \lim_{q\to 0} \sum_{\nu\nu'\sigma} \frac{4\pi e^2 (f_\nu - f_{\nu'}) \langle \Psi_{\nu\sigma\mathbf{k}}(\mathbf{r}) \mid \mathbf{v}_i \mid \Psi_{\nu'\sigma\mathbf{k}}(\mathbf{r})\rangle \langle \Psi_{\nu'\sigma\mathbf{k}}(\mathbf{r}') \mid \mathbf{v}'_i \mid \Psi_{\nu\sigma\mathbf{k}}(\mathbf{r}')\rangle}{(\omega - \epsilon_{\nu',\mathbf{k}+\mathbf{q}} + \epsilon_{\nu,\mathbf{k}} + i\eta)(\epsilon_{\nu',\mathbf{k}+\mathbf{q}} - \epsilon_{\nu,\mathbf{k}})^2}, \end{aligned} \tag{5.9}$$

according to the identity

$$\langle \nu\mathbf{k} \mid e^{-i\mathbf{q}\cdot\mathbf{r}} \mid \nu'\mathbf{k}\rangle = \frac{1}{\epsilon^{QP}_{\nu',\mathbf{k}} - \epsilon^{QP}_{\nu,\mathbf{k}}} \langle \nu\mathbf{k} \mid \mathbf{q}\cdot\mathbf{v} \mid \nu'\mathbf{k}\rangle^{QP}. \tag{5.10}$$

Here $i = x, y, z$. The wave number q is of the magnitude of that of visible light. In general, $q \sim 1/500nm$ and the Brillouin zone is of size around $1/0.5nm$, so q can be $0.001 \cdot 2\pi/a$ where a is the lattice constant. Please note that the optical transition matrix(OTM) elements in the right-hand side of the identity (7.17) can't be calculated directly. Alternatively, as mentioned by Rohlfing and Louie [64], one can evaluate the transition matrix elements by

$$q\langle \nu\mathbf{k} \mid \hat{\mathbf{e}}_i \cdot \mathbf{v} \mid \nu'\mathbf{k}\rangle^{QP} = (\epsilon^{QP}_{c\mathbf{k}} - \epsilon^{QP}_{\nu\mathbf{k}}) \langle \nu\mathbf{k} \mid e^{-iq\hat{\mathbf{e}}_i\cdot\mathbf{r}} \mid \nu', \mathbf{k}+\mathbf{q}\rangle, \tag{5.11}$$

A little trouble is that one has to calculate the wave functions explicitly at the shifted wave vectors $\mathbf{k} + q\mathbf{e}_i$. Here three directions of the photon momentum $\mathbf{q}$ has to be considered to include the angular dependence.

On the other hand, we found the mGGA V_{xc} distorted the KS eigenfunctions so that it affected the evaluation of the optical transition matrix elements. Therefore, we present a new method to calculate the OTM elements. Similar to the discussion by Rohlfing and Louie, we approximate the OTM elements under mGGA by

$$\langle \nu\mathbf{k} \mid \mathbf{v} \mid \nu'\mathbf{k}\rangle^{QP} = \frac{E^{QP}_{\nu'\mathbf{k}} - E^{QP}_{\nu\mathbf{k}}}{E^{LDA}_{\nu'\mathbf{k}} - E^{LDA}_{\nu\mathbf{k}}} \langle \nu\mathbf{k} \mid \mathbf{v} \mid \nu'\mathbf{k}\rangle^{LDA}, \tag{5.12}$$

since the calculation of KS eigenfunctions under LDA is very stable and, theoretically speaking, mGGA only modifies the band structure to generate correct band gap instead of the p-matrix. One problem arises from the above equation for the materials with zero band gap or negative band gap. We might set a energy cut around $0.5eV$ since the experiment mostly measures excitation spectra above $1eV$. During the calculation of spectra, mGGA eigenenergies are still used since they are correct QP energies. Similarly, When $G = 0$

and $G' \neq 0$,

$$
\begin{aligned}
X_{0,\mathbf{G}'}(\omega) &= [X_{\mathbf{G},0}(\omega)]^* = \lim_{q\to 0} \frac{4\pi e^2 \widehat{\chi}^{KS}_{0,\mathbf{G}'}(\mathbf{q},\omega)}{|\mathbf{q}||\mathbf{G}'+\mathbf{q}|} \qquad (5.13)\\
&= \lim_{q\to 0} \sum_{\nu,\nu',\sigma} \frac{4\pi e^2 (f_\nu - f_{\nu'}) \langle \Psi_{\nu,\sigma,\mathbf{k}}(\mathbf{r}) \mid e^{-i\mathbf{q}\cdot\mathbf{r}} \mid \Psi_{\nu',\sigma,\mathbf{k}}(\mathbf{r})\rangle \langle \Psi_{\nu',\sigma,\mathbf{k}}(\mathbf{r}') \mid e^{i(\mathbf{G}'+\mathbf{q})\cdot\mathbf{r}'} \mid \Psi_{\nu,\sigma,\mathbf{k}}(\mathbf{r}')\rangle}{(\omega - \epsilon_{\nu',\mathbf{k}+\mathbf{q}} + \epsilon_{\nu,\mathbf{k}} + i\eta)|\mathbf{q}||\mathbf{G}'+\mathbf{q}|}\\
&= \lim_{q\to 0} \sum_{\nu,\nu',\sigma} \frac{4\pi e^2 (f_\nu - f_{\nu'}) \langle \Psi_{\nu,\sigma,\mathbf{k}}(\mathbf{r}) \mid q\hat{\mathbf{e}}_i\cdot\mathbf{v} \mid \Psi_{\nu',\sigma,\mathbf{k}}(\mathbf{r})\rangle \langle \Psi_{\nu',\sigma,\mathbf{k}}(\mathbf{r}') \mid e^{i(\mathbf{G}'+\mathbf{q})\cdot\mathbf{r}'} \mid \Psi_{\nu,\sigma,\mathbf{k}}(\mathbf{r}')\rangle}{(\omega - \epsilon_{\nu',\mathbf{k}+\mathbf{q}} + \epsilon_{\nu,\mathbf{k}} + i\eta)(\epsilon_{\nu',\mathbf{k}+\mathbf{q}} - \epsilon_{\nu,\mathbf{k}})|\mathbf{G}'+\mathbf{q}|}
\end{aligned}
$$

5.2 The derivative of E_{xc} with respect to the kinetic energy density

An important quantity in Eq. (5.2) is the derivative of E_{xc} with respect to the kinetic energy density $\overline{\frac{\partial \epsilon_{xc}}{\partial \tau}}$. Since the TB09 doesn't provides an approximation for E_{xc}, other mGGA should be adopted to do this job. Voorhis and Scuseria's approximation(VS98) [15] was reported to be a good one to do the derivative [58], so we're going to use it in this work.

5.2.1 Implementation of VSxc

VS98 [15] have developed a new exchange-correlation functional based on the density matrix expansion(DME). In this approximation, both the exchange energy and the correlation energy used the same general form,derived from DME, for the nonlocal part, while they take that of the uniform electron gas as the local part. The exchange energy functional is given by

$$
e_x = \rho^{4/3}\left[\frac{a}{\gamma(x,z)} + \frac{bx^2+cz}{\gamma^2(x,z)} + \frac{dx^4+ex^2z+fz^2}{\gamma^3(x,z)}\right] \equiv \rho^{4/3} f(x,z)\,, \qquad (5.14)
$$

where

$$
f(x,z) \equiv \frac{a}{\gamma(x,z)} + \frac{bx^2+cz}{\gamma^2(x,z)} + \frac{dx^4+ex^2z+fz^2}{\gamma^3(x,z)}, \qquad (5.15)
$$

$$
\gamma(x,z) = 1 + \alpha(x^2+z)\,, \qquad (5.16)
$$

with x and z defined by

$$
x = \frac{|\nabla\rho|}{\rho^{4/3}}, \qquad z = \frac{\tau}{\rho^{5/3}} - C_F\,. \qquad (5.17)
$$

Here C_F is the Fermi constant given by

$$C_F = \frac{3}{5}(3\pi^2)^{2/3}\,.$$

and a, b, c, d, e, f and α are some constants(see table I in Ref. [15]). For the spin-polarized case, e_x is given by

$$e_x(\rho_\sigma) = \rho_\sigma^{4/3}\left[\frac{a}{\gamma(x_\sigma,z_\sigma)} + \frac{bx_\sigma^2 + cz_\sigma}{\gamma^2(x_\sigma,z_\sigma)} + \frac{dx_\sigma^4 + ex_\sigma^2 z_\sigma + fz_\sigma^2}{\gamma^3(x_\sigma,z_\sigma)}\right]. \tag{5.18}$$

where x_σ and z_σ have the same form as x and z but evaluated at ρ_σ. The same-spin and opposite-spin correlation functionals are given by

$$e_c^{\sigma\sigma} = \rho f(x_\sigma,z_\sigma) D_\sigma e_{c\sigma\sigma}^{LDA}\,, \tag{5.19}$$

and

$$e_c^{\sigma\sigma'}(\rho_\sigma,\rho_{\sigma'}) = \rho f(x,z) e_{c\sigma\sigma'}^{LDA}\,, \tag{5.20}$$

where

$$x^2 \equiv x_\uparrow^2 + x_\downarrow^2, \qquad z \equiv z_\uparrow + z_\downarrow, \qquad D_\sigma \equiv 1 - \frac{x_\sigma^2}{4(z_\sigma + C_F)}\,. \tag{5.21}$$

The derivatives of exchange-correlation energy over density, $\nabla\rho$ and τ can be computed according to equations above. We obtain

$$\frac{\partial f}{\partial \gamma} = -\frac{a}{\gamma^2(x,z)} - 2\frac{bx^2+cz}{\gamma^3(x,z)} - 3\frac{dx^4+ex^2z+fz^2}{\gamma^4(x,z)} \tag{5.22}$$

$$\frac{\partial f}{\partial x} = \frac{2bx}{\gamma^2(x,z)} + \frac{4dx^3+2exz}{\gamma^3(x,z)} + \frac{\partial f}{\partial \gamma}(2\alpha x)\,, \tag{5.23}$$

$$\frac{\partial f}{\partial z} = \frac{c}{\gamma^2(x,z)} + \frac{ex^2+2fz}{\gamma^3(x,z)} + \frac{\partial f}{\partial \gamma}(\alpha)\,, \tag{5.24}$$

$$\frac{\partial(D_\sigma f^{\sigma\sigma})}{\partial x_\sigma} = D_\sigma\left[\frac{2bx_\sigma}{\gamma^2(x_\sigma,z_\sigma)} + \frac{4dx_\sigma^3+2ex_\sigma z_\sigma}{\gamma^3(x_\sigma,z_\sigma)} + \frac{\partial f}{\partial\gamma}(2\alpha x_\sigma)\right] - f(x_\sigma,z_\sigma)\frac{x_\sigma}{2\frac{\tau}{\rho_\sigma^{5/3}}}\,, \tag{5.25}$$

$$\frac{\partial(D_\sigma f^{\sigma\sigma})}{\partial z_\sigma} = D_\sigma\left[\frac{c}{\gamma^2(x_\sigma,z_\sigma)} + \frac{ex_\sigma^2+2fz_\sigma}{\gamma^3(x_\sigma,z_\sigma)} + \frac{\partial f}{\partial\gamma}(\alpha)\right] + f(x_\sigma,z_\sigma)\frac{x_\sigma^2}{4(\frac{\tau}{\rho_\sigma^{5/3}})^2}\,. \tag{5.26}$$

Thus we get,

$$\frac{\partial e_x(x,z)}{\partial \rho} = \rho^{1/3}\left[\frac{4}{3}(f(x,z) - x\frac{\partial f}{\partial x}) - \frac{5}{3}(\frac{\tau}{\rho^{5/3}}\frac{\partial f}{\partial z})\right], \tag{5.27}$$

$$\frac{\partial e_c^{\sigma\sigma}}{\partial \rho} = f(x_\sigma, z_\sigma)D_\sigma e_{c\sigma\sigma}^{LDA} + \rho f(x_\sigma, z_\sigma)D_\sigma\frac{\partial e_{c\sigma\sigma}^{LDA}}{\partial \rho} - \rho e_{c\sigma\sigma}^{LDA}\left[\frac{4}{3}x_\sigma\frac{\partial(D_\sigma f^{\sigma\sigma})}{\partial x_\sigma} + \frac{5}{3}\frac{\tau}{\rho^{5/3}}\frac{\partial(D_\sigma f^{\sigma\sigma})}{\partial z_\sigma}\right], \tag{5.28}$$

$$\frac{\partial e_c^{\sigma\sigma'}}{\partial \rho} = f(x,z)e_{c\sigma\sigma'}^{LDA} + \rho f(x,z)\frac{\partial e_{c\sigma\sigma'}^{LDA}}{\partial \rho} - \rho e_{c\sigma\sigma'}^{LDA}\left[\frac{4}{3}\frac{\partial f}{\partial x}\frac{(x_\sigma^2)^2}{x} + \frac{5}{3}\frac{\tau}{\rho_\sigma^{5/3}}\frac{\partial f}{\partial z_\sigma}\right], \tag{5.29}$$

and

$$\frac{\partial e_x(x,z)}{\partial \tau} = \rho^{-1/3}\frac{\partial f}{\partial z}, \tag{5.30}$$

$$\frac{\partial e_c^{\sigma\sigma}}{\partial \tau} = e_{c\sigma\sigma}^{LDA}\frac{1}{\rho^{2/3}}\frac{\partial(D_\sigma f^{\sigma\sigma})}{\partial z_\sigma}, \tag{5.31}$$

$$\frac{\partial e_c^{\sigma\sigma'}}{\partial \tau} = e_{c\sigma\sigma'}^{LDA}\rho\frac{\partial f}{\partial z_\sigma}\frac{1}{\rho_\sigma^{5/3}}. \tag{5.32}$$

The exchange-correlation potential is then given by

$$V_{xc} = \frac{\partial e_x(x,z)}{\partial \rho} + \frac{\partial e_c^{\sigma\sigma}}{\partial \rho} + \frac{\partial e_c^{\sigma\sigma'}}{\partial \rho}. \tag{5.33}$$

5.2.2 LDA correlation energy density by Stoll

The parallel correlation energy density $e_{c\sigma\sigma}^{LDA}$ in Eq. (5.27) is given by [67]

$$e_{c\uparrow\uparrow}^{LDA} = \rho_\uparrow \varepsilon_{c\uparrow\uparrow}(\rho_\uparrow, 0), \tag{5.34}$$

$$e_{c\downarrow\downarrow}^{LDA} = \rho_\downarrow \varepsilon_{c\downarrow\downarrow}(0, \rho_\downarrow). \tag{5.35}$$

The total density parameter r_s and relative spin polarization ζ are of the form given by

$$r_s = \left(\frac{3}{4\pi\rho}\right)^{1/3}, \qquad \zeta = \frac{\rho_\uparrow - \rho_\downarrow}{\rho_\uparrow + \rho_\downarrow}. \tag{5.36}$$

Then we have

$$\rho_\uparrow = \frac{1+\zeta}{2}\rho, \qquad \rho_\downarrow = \frac{1-\zeta}{2}\rho. \tag{5.37}$$

The new density parameter r_s' is defined by

$$r_s' = \left(\frac{3}{4\pi\rho_s}\right)^{1/3} = \left(\frac{2}{1\pm\zeta}\right)^{1/3} r_s, \qquad \zeta_s' = \pm 1\,. \tag{5.38}$$

The derivative of $\partial e_{c\sigma\sigma}^{LDA}/\partial\rho$ needs the following derivatives

$$\frac{1}{\rho}\frac{\partial e_{c\sigma\sigma}^{LDA}}{\partial r_s} = \frac{\partial \varepsilon_{c\sigma\sigma}}{\partial r_s'}\frac{\partial r_s'}{\partial r_s}\frac{1\pm\zeta}{2}\,, \tag{5.39}$$

and

$$\frac{1}{\rho}\frac{\partial e_{c\sigma\sigma}^{LDA}}{\partial \zeta} = \pm\frac{\varepsilon_{c\sigma\sigma}}{2} + \frac{\partial \varepsilon_{c\sigma\sigma}}{\partial r_s'}\frac{\partial r_s'}{\partial \zeta}\frac{1\pm\zeta}{2}\,, \tag{5.40}$$

where

$$\frac{\partial r_s'}{\partial \zeta} = \mp\frac{r_s'}{3(1\pm\zeta)}\,. \tag{5.41}$$

5.3 Implementation of dielectric function

To calculate the exciton in the dielectric function, Eq. (5.6), we follow the implementation on the LAPW method [66] closely, since the LASTO basis functions are linear combinations of LAPWs. The transition matrix element, $\mathcal{T}_{\nu\nu'}(\mathbf{k},\mathbf{q})$, which is frequently used in calculating the electron-hole interaction kernel and KS response function, can be written as follows,

$$\begin{aligned}
\mathcal{T}_{\nu\nu'}(\mathbf{k},\mathbf{G}) &= < \nu\mathbf{k}|e^{-i(\mathbf{q}+\mathbf{G})\cdot\mathbf{r}}|\nu'\mathbf{k}' > \\
&= \int_V d\mathbf{r}\Psi_{\nu\mathbf{k}}^*(\mathbf{r})e^{-i(\mathbf{q}+\mathbf{G})\cdot\mathbf{r}}\Psi_{\nu'\mathbf{k}'}(\mathbf{r}) \\
&= \frac{V}{V_c}\int_{V_c} d\mathbf{r}\Psi_{\nu\mathbf{k}}^*(\mathbf{r})e^{-i(\mathbf{q}+\mathbf{G})\cdot\mathbf{r}}\Psi_{\nu'\mathbf{k}'}(\mathbf{r})
\end{aligned} \tag{5.42}$$

where $\mathbf{k}' = \mathbf{k}+\mathbf{q}$. Plug Eq.(3.10) into Eq.(5.42),

$$\begin{aligned}
\mathcal{T}_{\nu\nu'}(\mathbf{k},\mathbf{G}) &= \sum_{NN'} C_{\nu\mathbf{k}}C_{\nu'\mathbf{k}'}\frac{V}{V_c}\int_{V_c} d\mathbf{r}\psi_{\mathbf{k}N}^*(\mathbf{r})e^{-i(\mathbf{q}+\mathbf{G})\cdot\mathbf{r}}\psi_{\mathbf{k}'N'}(\mathbf{r}) \\
&= \sum_{NN'} C_{\nu\mathbf{k}}C_{\nu'\mathbf{k}'}t_{NN'}(\mathbf{k},\mathbf{q},\mathbf{G})
\end{aligned} \tag{5.43}$$

where

$$t_{NN'}(\mathbf{k},\mathbf{q},\mathbf{G}) \equiv \frac{V}{V_c}\int_{V_c} d\mathbf{r}\psi^*_{\mathbf{k}N}(\mathbf{r})e^{-i(\mathbf{q}+\mathbf{G})\cdot\mathbf{r}}\psi_{\mathbf{k}'N'}(\mathbf{r}) \tag{5.44}$$

The matrix element $t_{\mathbf{G}\mathbf{G}'}(\mathbf{k},\mathbf{q},\mathbf{G})$ can be computed in the interstitial region and the muffin-tin region separately.

In the interstitial region, the contribution to the matrix element $t_{NN'}(\mathbf{k},\mathbf{q},\mathbf{G})$ is given by

$$\begin{aligned} t_{NN'}(\mathbf{k},\mathbf{q},\mathbf{G}) &= \frac{1}{V_c}\int_{V_c} d\mathbf{r}\psi^*_{\mathbf{k}N}(\mathbf{r})\Theta(\mathbf{r})e^{-i(\mathbf{q}+\mathbf{G})\cdot\mathbf{r}}\psi_{\mathbf{k}'N'}(\mathbf{r}) \\ &= \frac{1}{V_c}\sum_{\mathbf{G}'\mathbf{G}''\mathbf{K}}\int_{V_c} d\mathbf{r}\phi^*_{\mathbf{k}}(\mathbf{G}')\Theta(\mathbf{K})e^{-i(\mathbf{G}'+\mathbf{G}-\mathbf{G}''-\mathbf{K})\cdot\mathbf{r}}\phi_{\mathbf{k}'}(\mathbf{G}'') \\ &= \sum_{\mathbf{G}'\mathbf{G}''}\phi^*_{\mathbf{k}}(\mathbf{G}')\Theta(\mathbf{G}'+\mathbf{G}-\mathbf{G}'')\phi_{\mathbf{k}'}(\mathbf{G}'') \end{aligned} \tag{5.45}$$

where $\Theta(\mathbf{r})$ is the step function defined by

$$\Theta(\mathbf{r}) \equiv \begin{cases} 1, \mathbf{r} \in \text{interstitial region} \\ 0, \mathbf{r} \ni \text{interstitial region} \end{cases}, \tag{5.46}$$

and $\Theta(\mathbf{G})$ is $\Theta(\mathbf{r})$'s Fourier coefficients which can be analytically computed by

$$\Theta(\mathbf{G}) = \begin{cases} 1 - \sum_i \frac{4\pi R_1^3}{3V_c}, \mathbf{G} = 0 \\ -\frac{4\pi}{V_c|\mathbf{G}|}\sum_i j_l(|\mathbf{G}|R_1)R_1^2 e^{i\mathbf{G}\mathbf{R}_1}, \mathbf{G} \neq 0 \end{cases}. \tag{5.47}$$

In the muffin-tin region, the contribution to the matrix element $t_{NN'}(\mathbf{k},\mathbf{q},\mathbf{G})$ comes from the integrals over those spheres in the unit cell given by

$$\begin{aligned} t_{NN'}(\mathbf{k},\mathbf{q},\mathbf{G}) &= \frac{1}{V_c}\sum_i e^{-i(\mathbf{q}+\mathbf{G})\cdot\mathbf{R}_i}\int_{MT_i} d\mathbf{r}\psi^*_{\mathbf{k}N}(\mathbf{r})e^{-i(\mathbf{q}+\mathbf{G})\cdot\mathbf{r}}\psi_{\mathbf{k}'N'}(\mathbf{r}) \\ &= \frac{1}{V_c}\sum_i e^{-i(\mathbf{q}+\mathbf{G})\cdot\mathbf{R}_i}\mathcal{I}_{NN'}(\mathbf{k},\mathbf{q},\mathbf{G}) \end{aligned} \tag{5.48}$$

where

$$\mathcal{I}_{NN'}(\mathbf{k},\mathbf{q},\mathbf{G}) \equiv \int_{MT_i} d\mathbf{r}\psi^*_{\mathbf{k}N}(\mathbf{r})e^{-i(\mathbf{q}+\mathbf{G})\cdot\mathbf{r}}\psi_{\mathbf{k}'N'}(\mathbf{r}) \tag{5.49}$$

is the integral over the *ith* muffin-tin sphere. To calculate this quantity, it's noted that the plane wave

$e^{-i(\mathbf{q}+\mathbf{G})\cdot\mathbf{r}}$ can be expanded using the Rayleigh expansion given by

$$e^{-i\mathbf{K}\cdot\mathbf{r}} = 4\pi \sum_{l=0}^{\infty} \sum_{m=-l}^{l} i^l j_l(Kr) Y_{lm}(\hat{\mathbf{K}}) Y_{lm}(\hat{\mathbf{r}}). \tag{5.50}$$

Plug Eq.(5.50) and Eq.(3.4) into Eq.(5.49) and regroup terms to get the new form of $\mathcal{I}_{NN'}(\mathbf{k},\mathbf{q},\mathbf{G})$ given by

$$\begin{aligned} \mathcal{I}_{NN'}(\mathbf{k},\mathbf{q},\mathbf{G}) &= \sum_{\tilde{N}'} \{ A_{N'\tilde{N}'}(\mathbf{k}') \sum_{\tilde{N}} [A^*_{N\tilde{N}}(\mathbf{k}) I(u,u,\mathbf{K}) + B^*_{N\tilde{N}}(\mathbf{k}) I(\dot{u},u,\mathbf{K})] \\ &+ B_{N'\tilde{N}'}(\mathbf{k}') \sum_{\tilde{N}} [A^*_{N\tilde{N}}(\mathbf{k}) I(u,\dot{u},\mathbf{K}) + B^*_{N\tilde{N}}(\mathbf{k}) I(\dot{u},\dot{u},\mathbf{K})] \}, \end{aligned} \tag{5.51}$$

with

$$I(u,u,\mathbf{K}) = 4\pi \sum_{L''} i^L Y^*_{L''}(\hat{\mathbf{K}}) G(L,L'',L') U_{l,l'',l'}(u,u,\mathbf{K}). \tag{5.52}$$

$$I(\dot{u},u,\mathbf{K}) = 4\pi \sum_{L''} i^L Y^*_{L''}(\hat{\mathbf{K}}) G(L,L'',L') U_{l,l'',l'}(\dot{u},u,\mathbf{K}). \tag{5.53}$$

$$I(u,\dot{u},\mathbf{K}) = 4\pi \sum_{L''} i^L Y^*_{L''}(\hat{\mathbf{K}}) G(L,L'',L') U_{l,l'',l'}(u,\dot{u},\mathbf{K}). \tag{5.54}$$

$$I(\dot{u},\dot{u},\mathbf{K}) = 4\pi \sum_{L''} i^L Y^*_{L''}(\hat{\mathbf{K}}) G(L,L'',L') U_{l,l'',l'}(\dot{u},\dot{u},\mathbf{K}). \tag{5.55}$$

where the Gaunt coefficients $G(L,L'',L')$ is given by

$$G(L,L'',L') = \int d\Omega Y^*_L(\hat{\mathbf{r}}) Y_{L''}(\hat{\mathbf{r}}) Y^*_{L'}(\hat{\mathbf{r}}), \tag{5.56}$$

and

$$U_{l,l'',l'}(u,u,\mathbf{K}) = \int_0^R r^2 dr u_l(r) j_{l''}(Gr) u_{l'}(r), \tag{5.57}$$

$$U_{l,l'',l'}(u,\dot{u},\mathbf{K}) = \int_0^R r^2 dr u_l(r) j_{l''}(Gr) \dot{u}_{l'}(r), \tag{5.58}$$

$$U_{l,l'',l'}(\dot{u},u,\mathbf{K}) = \int_0^R r^2 dr \dot{u}_l(r) j_{l''}(Gr) u_{l'}(r), \tag{5.59}$$

$$U_{l,l'',l'}(\dot{u},\dot{u},\mathbf{K}) = \int_0^R r^2 dr \dot{u}_l(r) j_{l''}(Gr) \dot{u}_{l'}(r). \tag{5.60}$$

5.4 Computational details

We first solve Kohn-Sham One-Particle Equation with mGGA self-consistently. The converged mGGA density will be used to compute the derivative of E_{xc} with respect to the kinetic energy density $\overline{\frac{\partial \epsilon_{xc}}{\partial \tau}}$ in

Eq. (5.2). Then results for materials we considered are listed in Table 5.1. The we use the converged Kohn-

Table 5.1: The derivative of E_{xc} with respect to the kinetic energy density

Si	Ge	GaAs	InAs	InP
0.0452	0.0784	0.0547	0.0404	0.0192

Sham eigenengergies and eigenfunctions from Chapter 4 to construct those quantities required in Eqs.(5.2), (5.3), (5.4) and (5.5). Then the dielectric function can be computed by Eq.(5.6).

5.4.1 Brillouin zone integration and convergence test

Here the summation over **k**-mesh will be evaluated directly and broadened with an appropriate width η when to calculate the dielectric function. The Monkhorst-Pack special points scheme [61, 62] is used to generate **k** points in the Brillouin zone (BZ). We'd better find a special **k**-mesh to do BZ integration accurately and efficiently. We can say that we need **k** points as many as possible to get converged results by intuition. However, it turns out that the larger number of **k** points is used in summation during the calculation, the more time will be consumed. It is because the number of the integral $\mathcal{T}_{\nu\nu'}(\mathbf{k}, \mathbf{G})$ and the size of the matrix increases proportionally to the square of the number of **k**. Besides of this, we found that the result converged when the number of **k** points reached some value. In addition, adding shift to **k** points during generation may improve the result. Albrecht et al. [68] used 2048 **k** points without shift in order to take advantage of the symmetry properties of the crystal, but the result didn't converge well and showed a wrong double peak behaviour. As a improvement, Albrecht and coworkers [69] obtained a much better and converged result with much less **k** points if appropriate shift was added. Benedict et al. [63], Arnaud et al. [65] and Puschnig et al. [66] applied shifted **k**-mesh in their calculation as well and got beautiful results. The reason is that shifting the mesh off the high symmetry directions could make **k** points so inequivalent that they all contribute to the final result. Meanwhile, the degenerate eigenstates can be avoided. For example, for a 10x10x10 **k**-mesh without shift, we can get only 47 independent **k** points in the irreducible BZ(IBZ) after symmetry operation, while 110 inequivalent **k** points can be obtained if an symmetric shift $(0.5, 0.5, 0.5)\frac{2\pi}{a}$ is applied during the generation. Furthermore, we can get a a denser **k**-mesh with 1000 nonequivalent points if the **k**-mesh is shifted by an arbitrary **k**-vector. In a word, we'd better adopt a shifted **k**-mesh in our calculation. For the summation over **q** points, we only need to consider $\mathbf{q} = 0$ in TDDFT calculation, i.e., the long wavelength limit.

To do the convergence test, we calculated Si spectra with a direct sum over **k**-mesh and Lorentzian-broadening. The number of **G** vectors is set to 65, and the number of valence bands 4, conduction bands 22.

The broadening η is set to 0.15 eV for Si and the rest materials in this chapter unless otherwise noted. With an arbitrary shift $(0.083333, 0.25, 0.416667)\frac{2\pi}{a}$, 8x8x8, 10x10x10, 12x12x12, 14x14x14 and 16x16x16 **k** mesh are tested. We choose this shift since it can generate homogeneous **k** points in the irreducible BZ(IBZ).The inequivalent **k** points and computational time corresponding to different k-mesh are listed in Table 5.2. From this table, all **k** mesh with an arbitrary shift can be handled in reasonable computation time. As

Table 5.2: The inequivalent **k** points and computational time corresponding to different k mesh. The first five mesh use the same shift $(0.083333, 0.25, 0.416667)\frac{2\pi}{a}$, while the mesh 8x8x8a is shifted by $(0.1, 0.2, 0.3)\frac{2\pi}{a}$.

	8x8x8	10x10x10	12x12x12	14x14x14	16x16x16	8x8x8a
k points	288	550	936	1470	2176	288
Time(s)	839.46	1584.04	2684.54	4204.48	6203.42	815.97

mentioned above, the convergence of spectra with different k-mesh may be different. Si spectra using 8x8x8, 10x10x10, 12x12x12, 14x14x14 and 16x16x16 **k** mesh are shown in Fig. 5.1. We can see that those spectra using different **k** mesh converge reasonably. The Figure shows that 12x12x12 **k** mesh for Si is enough in our calculation. For comparison, we also use another arbitrary shift $(0.1, 0.2, 0.3)\frac{2\pi}{a}$ to generate the 8x8x8

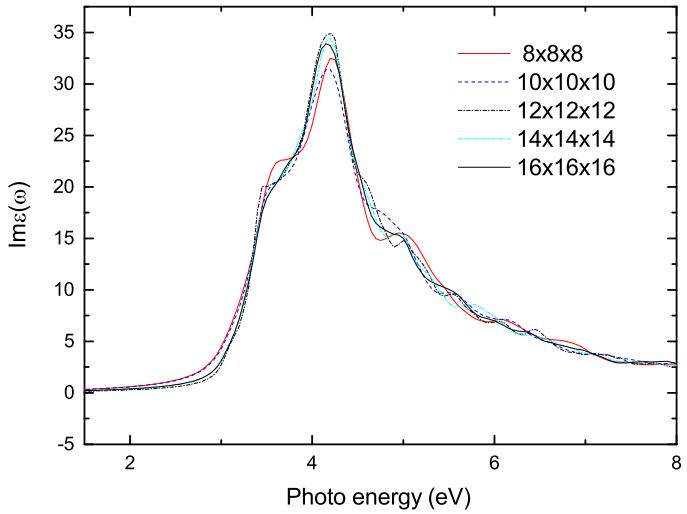

Figure 5.1: Si spectra in TDDFT level calculated with direct sum over **k** points under mGGA.

k mesh and compute the dielectric function for Si, see Fig. 5.2. It shows that with any arbitrary shift, one can get similar converged result.

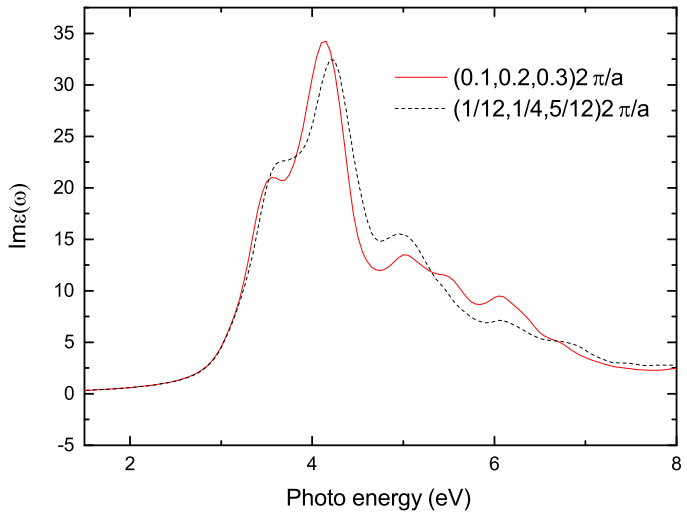

Figure 5.2: Si spectra in TDDFT level calculated with direct sum over **k** points with different arbitrary shift.

5.4.2 Optical spectrum with high angular momentum states

We compare the calculated optical absorption spectra of Si to experimental data [70] and find that the calculated peaks were weaker than the experimental ones, see Fig. 5.3. Let's look at those ζ values, which determines the basis set, used in Chapter 4 to solve the converged Kohn-Sham eigenengergies and eigenfunction under mGGA. These values tell that the basis set is a set of low angular momentum states which is good enough to solve band structures. However, it turns out that if we use the high angular momentum states as the basis set, we can improve the strength of those peaks, see Fig. 5.4, which compares Si optical absorption spectra calculated by the regular basis and high angular momentum **L** basis. From the figure, we see that the peaks are significantly improved by using latter. The optimized ζ values for Si, Ge, GaAs and InAs are listed in Table 5.3.

Table 5.3: Optimized ζ values for Si, Ge, GaAs and InAs

Si		3s	1.7	3p	1.4	3d	1.6	4e	0.5	5f	0.5
Ge		4s	1.2	4p	1.5	4d	1.8	4e	0.7	5f	0.9
GaAs	Ga	4s	1.2	4p	1.5	3d	1.5	4e	0.7	5f	0.7
	As	4s	1.2	4p	1.5	4d	1.8	4e	0.7	5f	0.96
InAs	In	5s	1.41	5p	1.69	4d	1.69	5e	0.9	6f	0.9
	As	4s	1.13	4p	1.41	4d	1.69	4e	0.9	5f	0.9

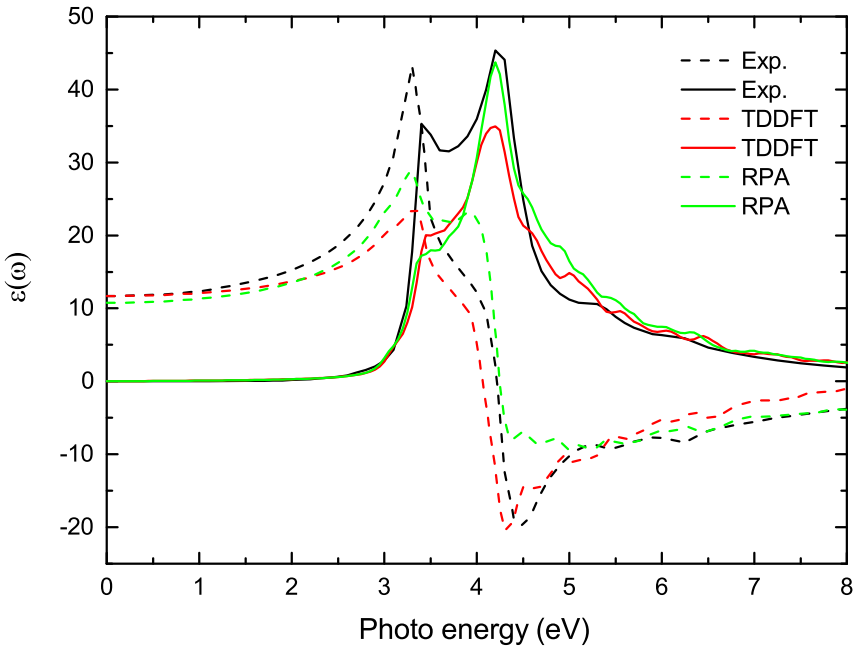

Figure 5.3: Calculated Si optical absorption spectra with excitonic effects compared to experimental data. Solid lines denote imaginary part while dashed lines denote real part.

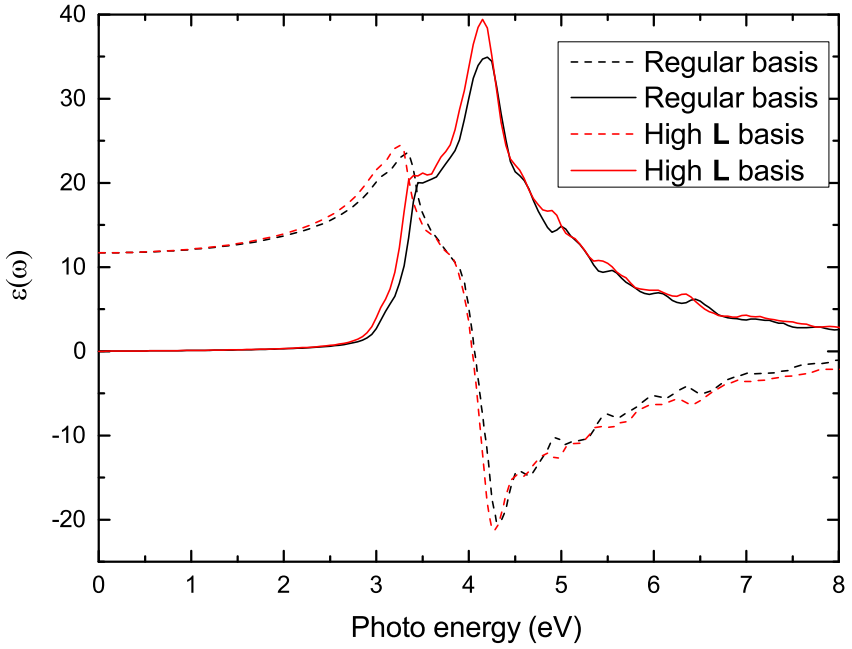

Figure 5.4: Compare Si optical absorption spectra calculated by the regular basis(black lines) and high angular momentum **L** basis(red lines). Solid lines denote imaginary part while dashed lines denote real part.

5.5 Results and discussion

We compare the calculated optical absorption spectra with excitonic effects of Si, Ge, InAs and GaAs in this section. The spectra of other materials, like alloys, will be discussed in the next chapter.

5.5.1 Si and Ge's optical absorption spectra

The spectra computed using 12x12x12 k mesh with an arbitrary shift $(1/12, 1/4, 5/12)\frac{2\pi}{a}$ and experimental spectrum are shown in Figs. 5.5 and 5.6. The experimental data [70] is denoted by dashed lines while the calculated ones denoted by only solid lines with different colors. These show that the calculated TDDFT spectrum with LDA p-matrix elements agrees better to the experimental one than the one using mGGA p-matrix elements since latter has weaker E_1 peak. It's noteworthy that the low frequency and high frequency parts are almost the same as the corresponding experimental ones. However, there are still notable discrepancies in the region between the E_1 and E_2 peaks. The difference of the E_2 peaks is less than 10% while the one of the E_1 peaks is a little big. We think that the main reason is that LASTO uses a smaller basis set which isn't accurate enough. Besides of this, the approximation for f_{xc} given by Eq. (2.33) discards many terms which could contribute to the spectrum.

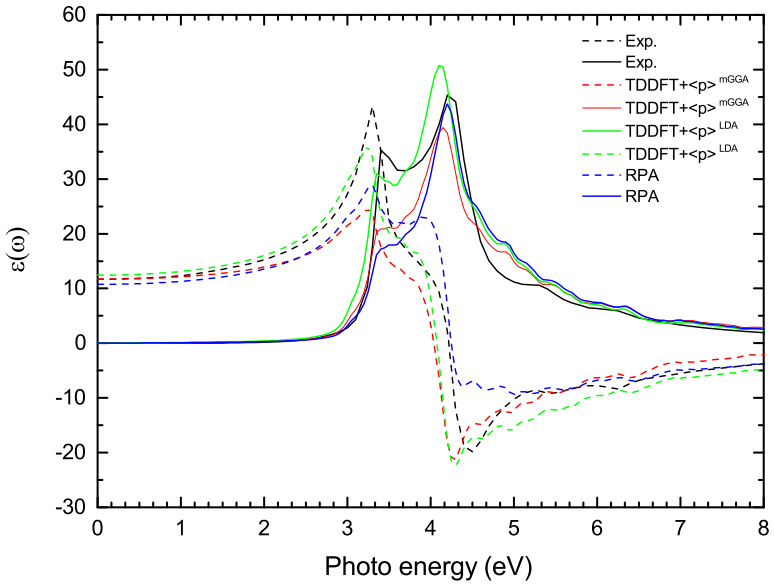

Figure 5.5: Calculated Si optical absorption spectra with excitonic effects compared to experimental data. Solid lines denote imaginary part while dashed lines denote real part.

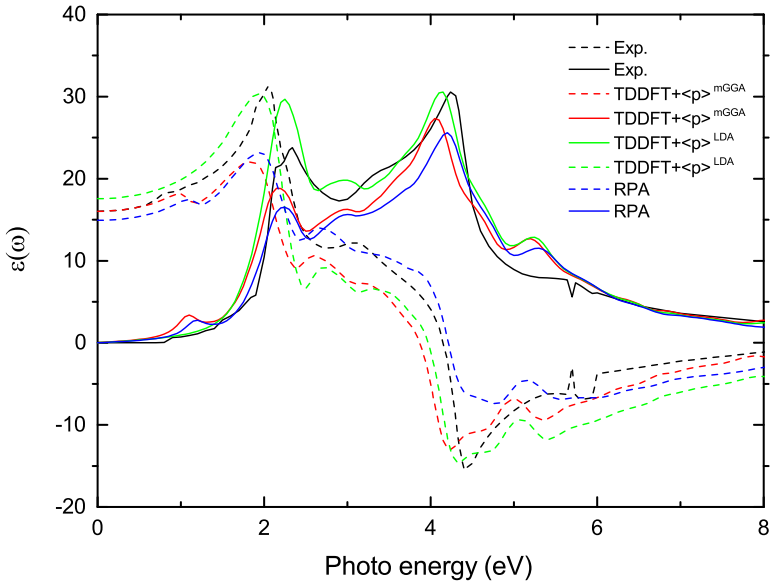

Figure 5.6: Calculated Ge optical absorption spectra with excitonic effects compared to experimental data. Solid lines denote imaginary part while dashed lines denote real part.

5.5.2 InAs and GaAs's optical absorption spectrum

The same 12x12x12 k mesh as Si's was used to compute InAs and GaAs's Kohn-Sham eigenfunctions and eigenenergies which are used to construct the spectrum. Figs. 5.8 shows the comparison of the calculated spectrum and the experimental data [70]. The experimental data [70] is denoted by dashed lines while the calculated ones denoted by solid lines with different colors. The calculated TDDFT spectra with LDA p-matrix elements agrees well to the experimental one as expected. Of course, small discrepancies still exist. The reasons are the same as Si and Ge's.

5.6 Conclusion

mGGA is a good approximation to generate band structure with approximately correct band gaps. This is the base of Nazarov and Vignale's theory [58]. Results show that their adiabatic TDDFT formalism can construct spectra for solids in good agreement with experimental data. The exchange-correlation kernel f_{xc} brings the required singularity of the type α/q^2, i.e., the nonlocality to the calculation, while the mGGA guarantee that the peaks are in the correct position. The TDDFT spectra with p-matrix approximated by the one under LDA agree great with the experimental data. Part of reason that Nazarov's result deviates from experimental data is that they didn't treat the p-matrix appropriately. The main discrepancies mainly

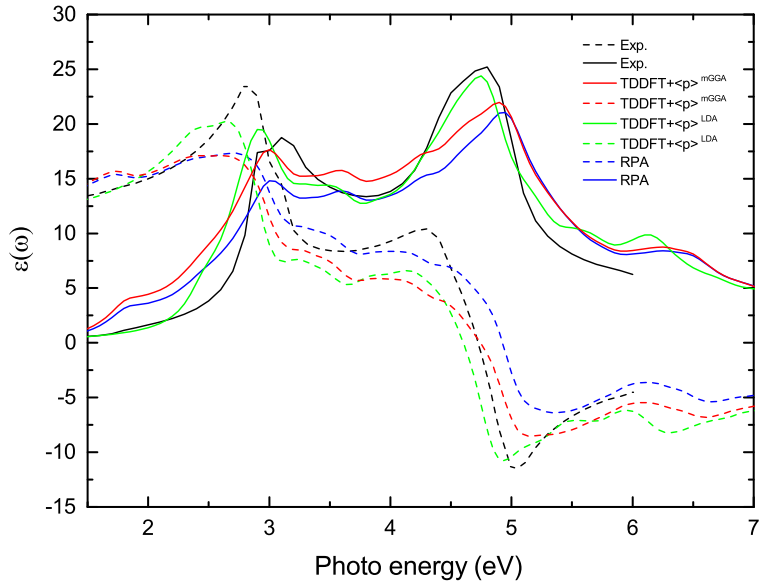

Figure 5.7: Calculated GaAs optical absorption spectra with excitonic effects compared to experimental data. Solid lines denote imaginary part while dashed lines denote real part.

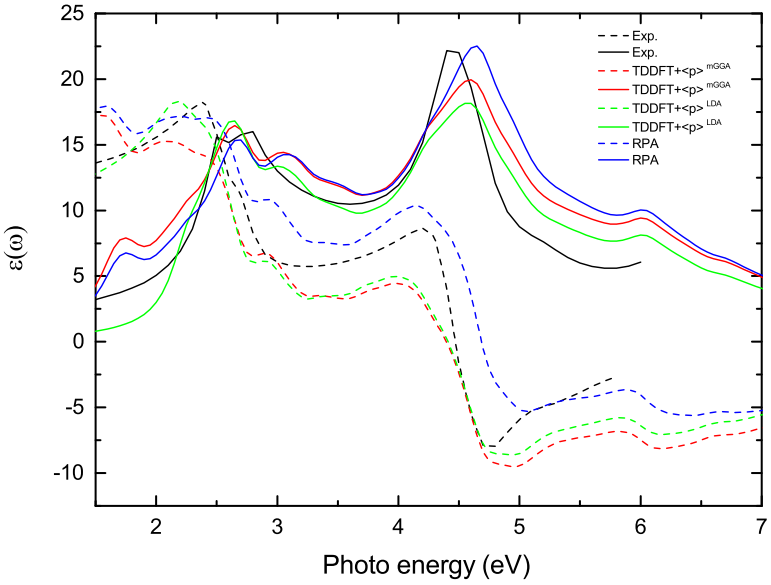

Figure 5.8: Calculated InAs optical absorption spectra with excitonic effects compared to experimental data. Solid lines denote imaginary part while dashed lines denote real part.

come from that (i) LASTO uses a smaller basis set which isn't accurate enough, and (ii) the approximation for f_{xc} given by Eq. (2.32) discards many terms which could contribute to the spectrum. Calculation of the exact mGGA exchange-correlation kernel f_{xc} given by Eq. (2.33) might solve the problem.

Chapter 6

Optical properties of semiconductors and alloys

III-V ternary alloys $A_xB_{1-x}C$ are promising materials for optoelectronic, high-speed electronic and microwave applications, such as infrared emitting diodes and detectors, high electron mobility transistors, heterojunction bipolar transistors, quantum-dot lasers, modulators and ultrafast switches [71–78]. The advantages of these alloys include high electron and hole mobility, large conduction band offset between the binary end points compounds AC and BC, better growth stability and design flexibility. The optical spectra of these alloys play an very important role in designing the devices. This work limits the discussion to isostructural and isovalent alloys only since physical properties of the alloy $A_xB_{1-x}C$ can be calculated by the analytical interpolation of the properties of constituents AC and BC. We put our focus on $In_xGa_{1-x}As$ and $InAs_xP_{1-x}$ alloys. $In_xGa_{1-x}As$ alloys can potentially outperform GaAs in electron transport properties and their room temperature band gaps are particularly well suited for applications in infrared emitting diodes and detectors [71]. Improved DC current gain and increased mobilities and saturation velocities make $InAs_xP_{1-x}$ a good material for heterojunction bipolar transistor [76]. The modulation-doped $InAs_xP_{1-x}$ shows better performance in quantum-well lasers [72]. High single-mode yield makes $InAs_xP_{1-x}$ showing competitive application in laser diodes [73]. Thus, it is highly desirable to have a better understanding of the electronic properties of these alloys. Kim et al. [79] and Choi et al. [80] reported the dielectric functions of selected compositions of different concentration x for $In_xGa_{1-x}As$ and $InAs_xP_{1-x}$, separately, including the endpoints values $x = 0$ and $x = 1$, which can be used as the database to analyze those with arbitrary concentration x.

On the other hand, people can use many theoretical methods, like Bethe-Salpeter equation (BSE) [20, 23–26] and time-dependent local density approximation (TDLDA) [81, 82], to calculate optical spectra for semiconductors and achieve good agreement with the experiment. These approaches focus on the response of the interacting system to a weak external perturbation and treat the exchange-correlation potential V_{xc} by local density approximation (LDA) [40]. However, severely underestimating the band gaps of materials has been a well-known difficulty about LDA and its semilocal extensions since the early 1980s [58]. A scissor operator $(\triangle E)P_{c\mathbf{k}}$ must be used to correct the band gap for their application in solids. The energy shift

($\triangle E$) is some constant which can be obtained either semiempirically [83] or by GW computation [84–86], and $P_{c\mathbf{k}}$ is the projection operator applied on conduction bands only. Unfortunately, it's impossible to use the scissor operator in alloy since it is a composition of two or more semiconductors and one can't determine which band gap should be corrected. One might be able to adopt GW correct to solve the gap problem, but it turns out that it is too expensive to be applied to big systems. Therefore, the notorious band gap problem from LDA prevents the application of those theoretical methods to alloys. Fortunately, the recent emerged meta-generalized gradient approximation(mGGA) [13–15] can fix the notorious underestimated band gaps caused by LDA [38, 39]. It expands the exchange-correlation potential in terms of not only the density, but also the gradient of the density $\nabla n_\sigma(\mathbf{r})$, the kinetic energy density $\tau(\mathbf{r})$ and(or) $\nabla^2 n_\sigma(\mathbf{r})$. Tran and Blaha's mGGA [14] shows great improvement in band gaps which can be in perfect agreement with experimental results.

Our studies provide some insight into the theoretical calculation of optical spectra of semiconductor alloys. The mGGA can be used to generate Kohn-Sham(KS) wave functions and eigenenergies with good band gaps for GaAs, InAs and their alloys. The idea of using time-dependent density functional theory (TDDFT) [19,53] with adiabatic mGGA to compute optical spectrum was adopted by Nazarov etc. [58]. They have implemented this approach into the full potential linearized augmented plane-wave (FPLAPW) [32] scheme to calculate optical spectrum for bulk Si and Ge with good success. FPLAPW needs a big number of plane waves as the basis which makes it not easy to be applicable to systems with large number of atoms. We will implement this approach into the linear augmented-slater-type orbits (LASTO) [27–30] scheme with adiabatic mGGA to compute optical spectra for alloys since LASTO uses less number of basis than FPLAPW, which we believe makes it more competitive to be applied to big systems than the latter.

In addition, recent ellipsometry measurement on various alloy systems have determined the compositional dependence of their optical spectra and several critical-point (CP) energies [87–90]. We are motivated to calculate the optical spectra of these ternary alloys theoretically and compare them to the experimental results. The LASTO method under mGGA will be adopted to calculate the required alloys' electronic structures with spin-orbit interactions included. Based on the calculated electronic structures, we use TDDFT to calculate dielectric functions for basic structures for a family of alloys. Then we adopt the cluster-averaging method, explained in section 6.2, to calculate the dielectric functions of alloys $\mathrm{In_xGa_{1-x}As}$ and $InAs_xP_{1-x}$ with arbitrary concentration x.

This chapter is organized as the following. First, the method to model alloys and the cluster-averaging method will be reviewed. Next, computational details such as parameters used during the calculation will be given. And then, calculated optical spectra of alloys $\mathrm{In_xGa_{1-x}As}$ and $InAs_xP_{1-x}$ will be compared to

experimental results.

6.1 Vegard's law and deviation

People know well properties of the binary end-point compounds AC and BC, while properties of the corresponding ternary alloys $A_xB_{1-x}C$, like the lattice constant, can be explained by Vegard's law [91] which states that there exists a linear relation which can describe the crystal physical properties of an alloy in terms of the concentration(x) of the constituent elements. According to this law, the lattice constant of a ternary alloy $A_xB_{1-x}C$ can be written as

$$a_{\mathrm{A_{1-x}B_xC}} = xa_{\mathrm{AB}} + (1-x)a_{\mathrm{AC}}. \tag{6.1}$$

However, the lattice constant of some alloys approximately abides by a quadratic form [93], but the deviation to the linear form given above is generally very small. Besides of the exceptions for lattice constant, alloy band gaps $E(x)$ are also found to deviate considerably from the composition average value of two end-point compounds AC and BC [94–96]. Furthermore, people found a quadratic form given by

$$F(x) = xF_{AC} + (1-x)F_{BC} - bx(1-x) \tag{6.2}$$

works well for many physical properties $F(x)$ of alloys $A_xB_{1-x}C$, where the general bowing parameter b is defined by [97]

$$b = 2[F_{AC}(a_{AC}) + F_{BC}(a_{BC}) - 2F_{A_{0.5}B_{0.5}C}(a_{A_{0.5}B_{0.5}C})], \tag{6.3}$$

where $F_{AC}(a_{AC})$ is the physical property of a end-point compound AC at its lattice constant a_{AC} and $F_{A_{0.5}B_{0.5}C}$ $(a_{A_{0.5}B_{0.5}C})$ the one of a 50%-50% alloy $A_{0.5}B_{0.5}C$ (also ABC_2) at its equilibrium lattice constant $a_{A_{0.5}B_{0.5}C}$. Instead of using the quadratic form, the cluster-averaging method can also be used to compute physical property of alloys with arbitrary concentration x.

6.2 Cluster-averaging Method

To calculate the dielectric functions for a ternary alloy $A_xB_{1-x}C$ with arbitrary concentration(x) of the constituent elements, we adopt the cluster-averaging method. Firstly, five basic structures, AC, BC, A_3BC_4, AB_3C_4 and the 50%-50% alloy ABC_2, have to be modeled and calculated at the corresponding

lattice constants that can be computed by Vegard's law [91] given by Eq. (6.1).

We model the binary end points compounds AC and BC by zinc blende structure with Td symmetry. Their calculation was done before. The remaining thing is to model a 50%-50% alloy $InGaAs_2$ and two minority clusters A_3BC_4 and AB_3C_4. In general, atoms are randomly distributed over the sample in alloys. However, for symmetry purpose, we'd better adopt periodic unit cells with special symmetries for them so that the calculation can be simplified and applicable. We follow the procedure described in Ref. [97]. In this work, we assume that the alloy systems of our interest all have cubic structure. The 50%-50% alloy can be approximately considered as a even mixture of compounds AC and BC. We model its unit cell by a supercell of four atoms with the primitive tetragonal structure whose symmetry is defined by space group No. 115 in the International Tables for Crystallography or point group D_{2d}. The primitive vectors of this structure are given by

$$\begin{aligned} \mathbf{a}_1 &= (\frac{1}{2}, -\frac{1}{2}, 0)a, \\ \mathbf{a}_2 &= (\frac{1}{2}, \frac{1}{2}, 0)a, \\ \mathbf{a}_3 &= (0, 0, 1)a, \end{aligned} \tag{6.4}$$

where a is the face-centered cubic lattice constant. Here we plot the unit cell of $InGaAs_2$ to show the primitive structure, see Fig. 6.1.

For both 25%-75% alloy AB_3C_4 and 75%-25% alloy A_3BC_4, we model them by a larger supercell of eight atoms with the primitive cubic structure whose symmetry is defined by space group No. 215 or point group T_d. Their primitive vectors are defined by

$$\begin{aligned} \mathbf{a}_1 &= (1, 0, 0)a \\ \mathbf{a}_2 &= (0, 1, 0)a \\ \mathbf{a}_3 &= (0, 0, 1)a. \end{aligned} \tag{6.5}$$

Here we use In_3GaAs_4 as an example to plot the unit cell, see Fig. 6.2. The one of $InGa_3As_4$ is similar to Fig. 6.2 with symbols In and Ga switched only.

As described above, we only need three different unit cells for the five basic structures, the typical Zincblende unit cell for AC and BC, the primitive tetragonal unit cell for 50%-50% alloy ABC_2, and the primitive cubic unit cell for 25%-75% and 75%-25% alloys, AB_3C_4 andA_3BC_4. However, to avoid systematic

Figure 6.1: $InGaAs_2$ primitive tetragonal unit cell

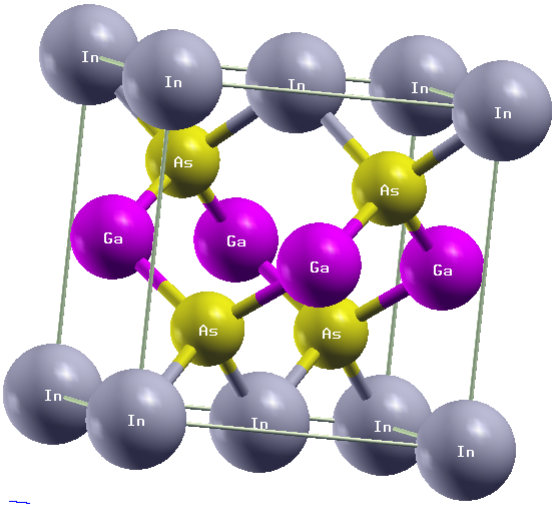

Figure 6.2: In_3GaAs_4 primitive cubic unit cell

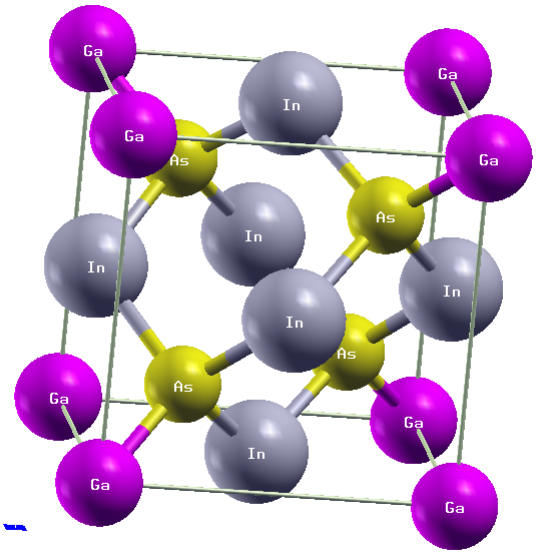

errors, the largest unit cell, specified by Eq. (6.5) and Fig. 6.2, is used to model the latter three alloys, that is, the unit cell of ABC_2 is twice bigger than the one defined by Eq. (6.4) and Fig. 6.1. Additionally, we need to specify the Cartesian coordinates of atoms in the unit cells. In general, their constituent atoms can move independently and are allowed to relax in such a way that they must keep the required symmetry as described above. To decide their equilibrium positions, we call WIEN2K [46] to do atomic relaxation for them since LASTO uses less number of basis functions than LAPW so it can't do such kind of job. Please note that we don't use supercell for AC and BC since we found results from supercell unit cell and WignerCSeitz cell were the same through comparison.

Then, their electronic structures can be computed based on the unit cells defined above. When KS eigenfunctions and eigenenergies are ready, the TDDFT+mGGa method with p-matrix approximated by the one under LDA (described in Chapter 5) is adopted to calculate their dielectric functions. Their contributions to the one of the alloy of interest are incorporated with occurrence probabilities $P^{(n)}(x)$

$$\varepsilon_M(\mathbf{q},\omega,a_x) = \sum_n P^{(n)}(x_n)\cdot\varepsilon_M(A_nB_{4-n}C_4,a_{x_n})\,, \tag{6.6}$$

where $a_x \equiv a_{\mathrm{A_{1-x}B_xC}}$. These probabilities are assumed to be random and can be calculated by the equation

$$P^{(n)}(x) = \begin{pmatrix} 4 \\ n \end{pmatrix} x^n(1-x)^{4-n}\,, \tag{6.7}$$

Table 6.1: The lattice constants(Bohr) of basic ternary alloys $InGaAs_2$, $InGa_3As_4$, In_3GaAs_4, In_2AsP, In_4As_3P and In_4AsP_3.

$InGaAs_2$	$InGa_3As_4$	In_3GaAs_4	In_2AsP	In_4As_3P	In_4AsP_3
11.06586	10.87443	11.25710	11.26939	11.35896	11.17981

where $n = 0, 1, ..., 4$.

6.3 Parameters and Structural Properties

Now We calculate the optical spectra of alloys $In_xGa_{1-x}As$ and $InAs_xP_{1-x}$ and fit them to experimental results. The SO coupling is considered during the calculation.

6.3.1 Band Structures

As mentioned above, five basic structures needs to be calculated first. The self-consistent KS band structures of $GaAs$, $InGa_3As_4$, $InGaAs_2$, In_3GaAs_4, $InAs$, InP, In_2AsP, In_4As_3P and In_4AsP_3 were computed with TB09 [14] mGGA and LASTO basis scheme. The three endpoint compounds $InAs$, $GaAs$ and InP are bulk structure with Td symmetry. The reference from which their experimental lattice constants at room temperature were taken is Ref. [92]. Their other parameters and dielectric functions were done in Chapter 5. Here we'll redo this part with only SO interaction added. For the 50%-50% alloys , 25%-75% alloys and 75%-25% alloys, their lattice constants were computed by Vegard's law and are listed in Table 6.1. The unit cell for all six alloys are supercell with basis vectors given by Eq. (6.5). Since LASTO uses point group to do the calculation, we use D2d symmetry for the 50%-50% alloys $InGaAs_2$ and In_2AsP, and Td symmetry for the primitive cubic structure for 25%-75% alloys $InGa_3As_4$ and In_4AsP_3 and 75%-25% alloys In_3GaAs_4 and In_4As_3P. The relaxed coordinates of atoms of the alloys are listed in Tables 6.2 and 6.3.

Table 6.2: The Cartesian coordinates of atoms of relaxed alloys $InGaAs_2$, $InGa_3As_4$ and In_3GaAs_4.

$InGaAs_2$	$InGa_3As_4$	In_3GaAs_4
In_1(0, 0, 0)	In_1(0, 0, 0)	Ga_1(0, 0, 0)
In_2(0.5, 0.5, 0)	Ga_1(0, 0.5, 0.5)	In_1(0, 0.5, 0.5)
Ga_1(0.5, 0, 0.5)	Ga_2(0.5, 0, 0.5)	In_2(0.5, 0.5, 0)
Ga_2(0, 0.5, 0.5)	Ga_3(0.5, 0.5, 0)	In_3(0.5,0, 0.5)
As_1(0.7503, 0.7503, 0.2705)	As_1(0.2596, 0.2596, 0.2596)	As_2(0.2395, 0.2395, 0.2395)
As_2(0.2497, 0.2497, 0.2705)	As_2(0.2596, 0.7404, 0.7404)	As_2(0.2395, 0.7605, 0.7605)
As_3(0.7503, 0.2497, 0.7295)	As_3(0.7404, 0.7404, 0.2596)	As_3(0.7605, 0.7605, 0.2395)
As_4(0.2497, 0.7503, 0.7295)	As_4(0.7404, 0.2596, 0.7404)	As_4(0.7605, 0.2395, 0.7605)

Table 6.3: The Cartesian coordinates of atoms of relaxed alloys In_2AsP, In_4As_3P and In_4AsP_3.

In_2AsP	In_4As_3P	In_4AsP_3
As_1(0, 0, 0)	P_1(0, 0, 0)	As_1(0, 0, 0)
As_2(0.5, 0.5, 0)	As_1(0, 0.5, 0.5)	P_1(0, 0.5, 0.5)
P_1(0.5, 0, 0.5)	As_2(0.5, 0, 0.5)	P_2(0.5, 0.5, 0)
P_2(0, 0.5, 0.5)	As_3(0.5, 0.5, 0)	P_3(0.5,0, 0.5)
In_1(0.7502, 0.7502, 0.2581)	In_1(0.2466, 0.2466, 0.2466)	In_2(0.2544, 0.2544, 0.2544)
In_2(0.7502, 0.2498, 0.7419)	In_2(0.2466, 0.7534, 0.7534)	In_2(0.2544, 0.7456, 0.7456)
In_3(0.2498, 0.2498, 0.2581)	In_3(0.7534, 0.7534, 0.2466)	In_3(0.7456, 0.7456, 0.2544)
In_4(0.2498, 0.7502, 0.7419)	In_4(0.7534, 0.2466, 0.7534)	In_4(0.7456, 0.2544, 0.7456)

The optimized ζ values for the LASTO basis functions of the constituent astoms are listed in Tables 6.4 and 6.5. The band structures of $GaAs$, $InAs$, InP,$InGaAs_2$ and In_2AsP are shown in Figs. 6.3, 6.4, 6.5,

Table 6.4: Optimized ζ values for $InGaAs_2$, $InGa_3As_4$ and In_3GaAs_4

$InGaAs_2$						$InGa_3As_4$						In_3GaAs_4					
In		Ga		As		In		Ga		As		In		Ga		As	
5s	1.5	4s	1.2	4s	1.2	5s	1.4	4s	1.2	4s	1.2	5s	1.5	4s	1.2	4s	1.2
5p	1.8	4p	1.5	4p	1.5	5p	1.7	4p	1.5	4p	1.5	5p	1.8	4p	1.5	4p	1.5
4d	2.3	3d	1.8	3d	1.5	4d	2.4	3d	1.9	3d	1.6	4d	2.3	3d	2.0	4d	1.5
5s	1.0	4s	0.8	4s	1.7	5s	0.9	4s	1.8	4s	1.8	5s	1.0	4s	1.6	4s	1.7
5p	1.2	4p	1.0	4p	2.2	5p	1.1	4p	2.3	4p	2.3	5p	1.2	4p	2.3	4p	2.2

Table 6.5: Optimized ζ values for In_2AsP, In_4As_3P and In_4AsP_3

In_2AsP						In_4As_3P						In_4AsP_3					
In		As		P		In		As		P		In		As		P	
5s	1.1	4s	1.1	3s	0.9	5s	1.4	4s	2.0	3s	0.9	5s	1.4	4s	1.2	3s	0.9
5p	1.7	4p	1.4	3p	0.8	5p	1.7	4p	1.4	3p	1.1	5p	1.7	4p	1.4	3p	1.2
4d	2.7	4d	1.7	3d	0.5	4d	1.7	4d	1.7	3d	1.4	4d	1.9	4d	1.7	3d	1.4
5s	1.0	4s	1.7	3s	1.3	5s	0.9	4s	1.7	3s	1.3	5s	1.0	4s	1.7	3s	2.2
5p	1.1	4p	2.1	3p	1.7	5p	1.1	4p	2.1	3p	1.7	5p	1.2	4p	2.1	3p	1.7

6.6 and 6.7, computed by both LASTO and WIEN2K for comparison. We can see that LASTO still keeps the required accuracy for band structures even if it uses a contracted basis set of LAPW.

6.3.2 Spectra

Based on the band structures, We calculated optical spectra for five basic structures, using TDDFT with the transition matrix elements approximated by the LDA p-matrix elements, as described by Eq. (5.12), via mGGA. We used a 8x8x8 k-mesh for supercells and 10x10x10 k-mesh for bulk structures, generated by

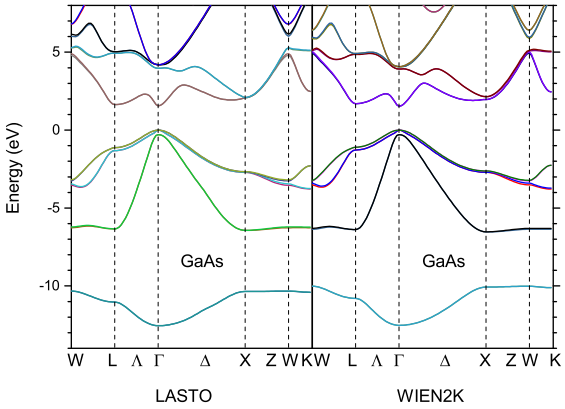

Figure 6.3: Band structures of GaAs.

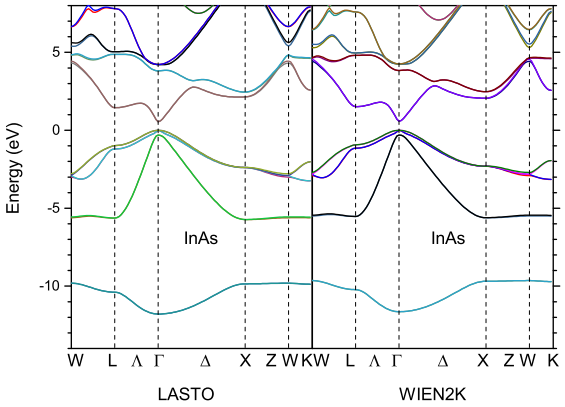

Figure 6.4: Band structures of InAs.

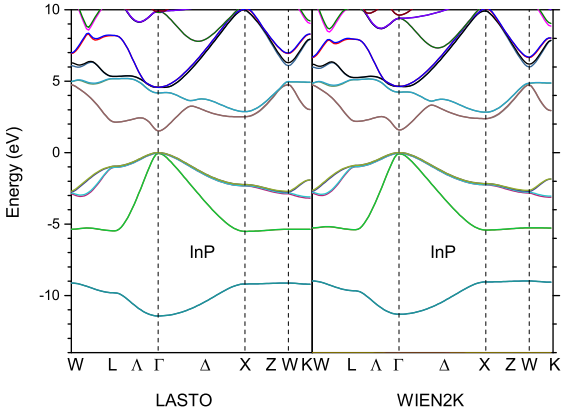

Figure 6.5: Band structures of InP.

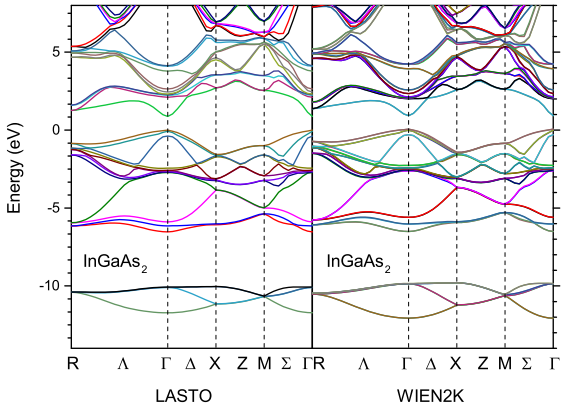

Figure 6.6: Band structures of $InGaAs_2$.

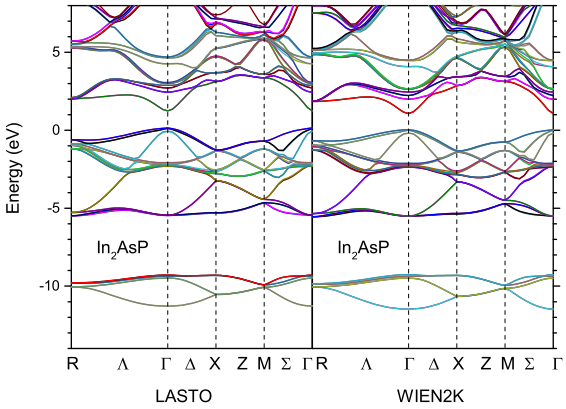

Figure 6.7: Band structures of In_2AsP.

Monkhorst-Pack [61] method with shift $(0.083333, 0.25, 0.416667)\frac{2\pi}{a}$, to do the Brilloin zone integration. The cutoffs of the reciprocal vectors were set to 2.3 for bulk structures and 1.5 for supercells. The average value of the derivative of the XC energy with respect to the kinetic energy density in Eq. (2.24) were computed by Voorhis and Scuseria's XC functional [15]. Their spectra are presented in Figs. 6.8 and 6.9.

6.4 Results and discussion

Once we get the dielectric functions for the basic five structures, we can use Eq. (6.6) to calculate the spectrum at any concentration x. The theoretical results are compared to the experimental ones at concentration $x = 0.17, 0.34, 0.49, 0.52, 0.56, 0.66$ for $\mathrm{In_xGa_{1-x}As}$(see Reference [79]), and at concentration $x = 0.13, 0.40, 0.60, 0.80$ for $InAs_xP_{1-x}$(see Reference [80]). The experimental spectra were determined

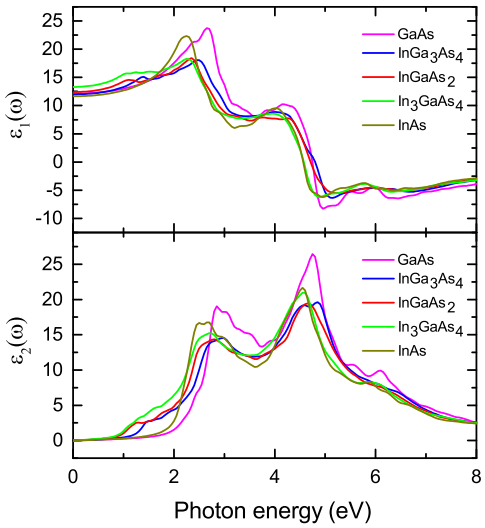

Figure 6.8: Optical spectra of five basic structures.

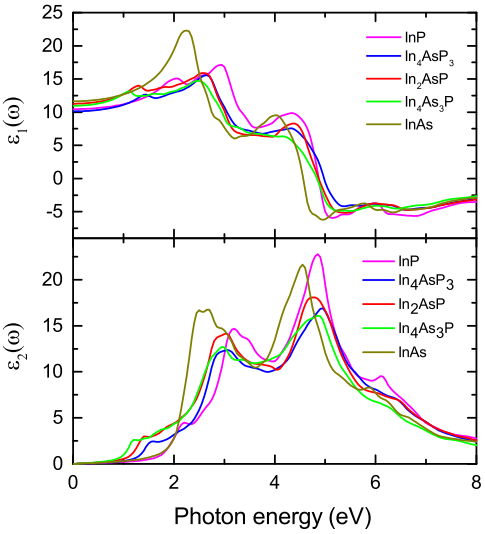

Figure 6.9: Optical spectra of five basic structures.

by ellipsometry psedodielectric functions. Here we present the occurrence probabilities of the five basic structures of $In_xGa_{1-x}As$ for different concentrations x, listed in Table 6.6. This table shows that the dielectric function of a arbitrary concentration x is mainly determined by the structures with concentration close to it while other structures only modify the behavior a little bit. Those of $InAs_xP_{1-x}$ shows similar behaviour.

Table 6.6: The occurrence probabilities of the five basic structures GaAs, $InGa_3As_4$, $InGaAs_2$, In_3GaAs_4 and InAs in a alloy with concentration x.

	GaAs	$InGa_3As_4$	$InGaAs_2$	In_3GaAs_4	InAs
x=0.17	0.47458	0.38882	0.11945	0.01631	0.00835
x=0.34	0.18974	0.39099	0.30213	0.10376	0.01336
x=0.49	0.06765	0.25999	0.37470	0.24000	0.05765
x=0.52	0.05308	0.23003	0.37380	0.26996	0.07312
x=0.56	0.03748	0.19081	0.36427	0.30908	0.09834
x=0.66	0.01336	0.10376	0.30213	0.39099	0.18975

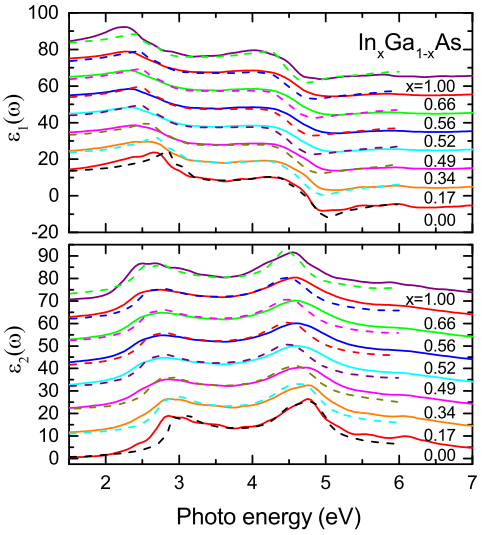

Figure 6.10: Optical spectra of alloys $In_xGa_{1-x}As$. Colored and solid lines are results obtained with cluster averaging method, except for $x = 0$ and $x = 1$ whose results are computed with mGGA band structures including the many-body interactions through f_{XC} given by Eq. (2.24). Colored and dashed lines are experimental data from Ref. [79].

The comparison of theoretical and experimental spectra is plotted in Figs. 6.10 and 6.11. The curves show that low energy parts of the spectra, especially the E_1 peaks, agree greatly with experimental data while some E_2 peaks deviate the experimental ones. Some discrepancies exist in the energy range above E_2 peaks. Note that our theoretical results have two peaks around E_1 which are very similar to the ones from experiment. This is because our calculation includes SO interaction so the SO splitting is shown in the figure. The great agreement of experimental and theoretical results proves the success of the TDDFT theory with LDA p-matrix and the cluster averaging method.

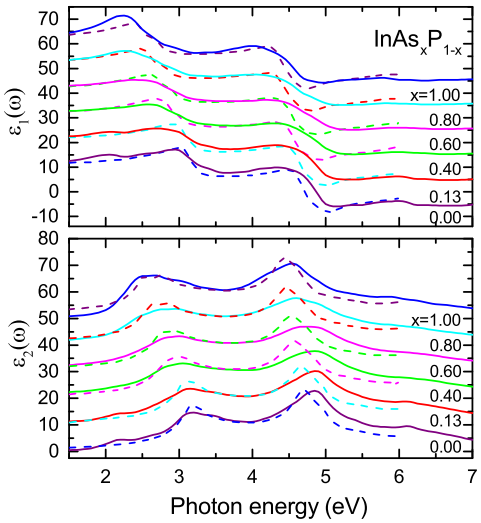

Figure 6.11: Optical spectra of alloys $InAs_xP_{1-x}$. Colored and solid lines are results obtained with cluster averaging method, except for $x = 0$ and $x = 1$ whose results are computed with mGGA band structures including the many-body interactions through f_{XC} given by Eq. (2.24). Colored and dashed lines are experimental data from Ref. [80].

6.5 conclusion

We used the TDDFT theory with LDA p-matrix and the cluster averaging method to compute the spectra of $In_xGa_{1-x}As$ and $InAs_xP_{1-x}$ with arbitrary concentration x and compared them to experimental results. It turns out the great success of this method. This method is simple and time saving. The main reason is that mGGA provides correct band structures for alloys so that the expensive GW correction or inapplicable rigid scissor operator is no longer needed in our calculation. We believe this method can be applied in more materials, especially some with special structures, like superlattice, in the future.

Chapter 7

BSE Calculation of Optical properties of semiconductors with electron-hole interactions

7.1 Introduction

Density functional theory(DFT) [8,9] provides a promising method which reduces the usually unresolvable interacting many-body Schrödinger equation to the solvable one-particle Kohn-Sham(KS) equation. Within the KS framework, although the many-body interactions are replaced by the effective potential, the many-body effects still exist through the exchange-correlation potential V_{xc} which doesn't have an analytic form and must be approximated when to solve the KS equation. In general, V_{xc} is a functional of the density $n_\sigma(\mathbf{r})$. A simple approximation is to expand V_{xc} only in terms of the density, i.e., the so called local density approximation (LDA) [40] which is good for a system with slowly varying density. A serious problem with it is that it severely underestimate the band gaps compared to experiment for semiconductors and insulators [38, 39]. A scissor operator $(\triangle E)P_{c\mathbf{k}}$ must be used to correct the band gap for its application in solids. The energy shift $(\triangle E)$ is some constant which can be obtained either semiempirically [83] or by GW computation [84–86], and $P_{c\mathbf{k}}$ is the projection operator applied on conduction bands only. Unfortunately, it's impossible to use the scissor operator in alloy and superlattice since one has to correct band gaps for two or more materials at the same time. To improve the accuracy of the band gap, meta-generalized gradient approximation(mGGA) [13–15] expands the exchange-correlation potential in terms of not only the density, but also the gradient of the density $\nabla n_\sigma(\mathbf{r})$, the kinetic energy density $\tau(\mathbf{r})$ and(or) $\nabla^2 n_\sigma(\mathbf{r})$. Tran and Blaha's mGGA [14] shows great improvement in band gaps which can be in perfect agreement with experimental results. Armed with true band gaps, one can easily compute the spectra of superlattice made of two semiconductor materials with different band gaps, like $(GaAs)_m(AlAs)_m$. The electron transport can be studied which was barely done because of incorrect electron tunneling rates caused by wrong band gaps. One can also combine mGGA with tight-binding method to predict the correct positions of the defect levels in InAs, HgTe and CdTe.

DFT is widely used in ab-initio framework to study electronic structure of solids. However, DFT is a ground state theory whose eigenenergy are neither the addition nor the removal energies of electrons from

the interacting many-body system, that is, the excitation energies can't be obtained by the difference of the KS eigenenergies. On the other hand, the excitation levels play a very important role in the application of solid materials. Fortunately, the response of the interacting system to an external perturbation contains enough information for them. Therefore, one can compute the excitations via dynamical response theory based on the KS eigenfunctions and eigenenergies.

For weak external perturbations, Nazarov etc. [58] reported that time-dependent density functional theory (TDDFT) [19,53] with adiabatic mGGA could generate accurate optical spectrum for bulk Si and Ge. They brilliantly approximated the exchange-correlation kernal f_{xc} to be linearly dependent on the inverse of the static KS density response function $\chi_s(\mathbf{r}, \mathbf{r}', \omega)$ which solved the notorious "ultranonlocality" problem, just the one preventing TDDFT's application to extended systems [98]. The further application of their approach maybe requires a full numerical implementation of the exact mGGA f_{xc}, see Eq. (5) in Ref. [58]. Alternatively, Puschnig etc. [66] implemented the Bethe-Salpeter equation (BSE) [20,23–26] for the electron-hole interaction to compute the absorption spectrum and got impressive agreement with the experimental data. Since they used LDA to generate KS eigenfunctions and eigenenergies, a GW correction or a rigid scissors operator should be used to correct the band gaps. Note that both approaches were implemented into the full potential linearized augmented plane-wave (FPLAPW) [32] scheme which uses a big number of plane waves as the basis which makes them not easy to be applicable to systems with large number of atoms. In addition, FPLAPW maybe a reason that makes BSE computationally demanding. In this work, we will implement the BSE method into the linear augmented-slater-type orbits (LASTO) scheme with adiabatic mGGA to compute optical spectra for bulk and superlattice semiconductors. LASTO uses less number of basis than FPLAPW, which we believe makes it more competitive to be applied to big systems than the latter.

This chapter is organized as follows. In Sec. 7.2 we briefly review the BSE concepts and formulas on which our calculation is based. In Sec. III we apply the BSE approach to compute the optical absorption spectra of bulk Si and GaAs. The results are compared to and gotten good agreement with experimental data. Finally, a short summary and outlook is presented to conclude this chapter in Sec. IV.

7.2 Theoretical methods

To describe optical excitations correctly, we should go beyond the independent particle approximation and include electron-hole interactions in the dielectric function. It has been shown that the inclusion of electron-hole interactions via the Bethe-Sapleter equation (BSE) significantly improves the optical spectra [20,23–26].

Let's start from the integral form of the BSE for the electron-hole correlation function L given by

$$L(1,2;1',2') = L_0(1,2;1',2') + \int d(3456) L(1,4;1',3)\Xi(3,5;4,6)L(6,2;5,2')\,, \tag{7.1}$$

where

$$L(1,2;1',2') \equiv -G_2(1,2;1',2') + G(1,1')G(2,2')\,, \tag{7.2}$$

L_0 describes the free motion of an electron and an hole given by

$$L_0(1,2;1',2') = G(1,2')G(2,1')\,, \tag{7.3}$$

Ξ is the effective electron-hole interaction kernel, and the labels $1, 2, ...$ mean the combination of variables of space, spin, and time. In principle, we can get all required information about electron-hole by solving Eq. (7.1). However, it's not trivial to solve it directly. Instead, following some suitable algorithm, it can be transformed into a generalized eigenvalue problem. We follow the derivation of Strinati [26] and obtain,

$$(E_{c\mathbf{k}+\kappa} - E_{v\mathbf{k}})A^{\lambda}_{vc\mathbf{k}} + \sum_{v'c'\mathbf{k}'} \Xi_{vc\mathbf{k},v'c'\mathbf{k}'+\kappa} A^{\lambda}_{v'c'\mathbf{k}'} = E^{\lambda} A^{\lambda}_{vc\mathbf{k}}\,, \tag{7.4}$$

where $v(c)$ denotes a valence band index(a conduction band index) of an quasiparticle at Bloch vector $\mathbf{k}$, and κ is the momentum of an absorbed photon. In this work, we consider zero-momentum excitations only, i.e., $\kappa = 0$. $E_{c\mathbf{k}}$ and $E_{v\mathbf{k}}$ are quasiparticle eigenvalues in conduction bands and valence bands respectively. The matrix elements of the kernel Ξ are evaluated on the basis given by the single-particle KS wavefunctions of the electron and hole states given by [64],

$$\Xi^{dir}_{vc\mathbf{k},v'c'\mathbf{k}'} = -\int d\mathbf{x}\; d\mathbf{x}' \psi^*_{c,\mathbf{k}}(\mathbf{x})\psi_{c',\mathbf{k}'}(\mathbf{x}) W(\mathbf{r},\mathbf{r}')\psi_{v\mathbf{k}}(\mathbf{x}')\psi^*_{v'\mathbf{k}'}(\mathbf{x}')\,, \tag{7.5}$$

$$\Xi^{ex}_{vc\mathbf{k},v'c'\mathbf{k}'} = \int d\mathbf{x}\; d\mathbf{x}' \psi^*_{c,\mathbf{k}}(\mathbf{x})\psi_{v,\mathbf{k}}(\mathbf{x}) v(\mathbf{r},\mathbf{r}')\psi_{c'\mathbf{k}'}(\mathbf{x}')\psi^*_{v'\mathbf{k}'}(\mathbf{x}')\,, \tag{7.6}$$

where $\psi_{n\mathbf{k}}$ denotes the one-particle state at wave vector $\mathbf{k}$ and band index n with a corresponding eigenvalue $E_{n\mathbf{k}}$ and $v(\mathbf{r},\mathbf{r}')$ is the bare Coulomb interaction. The direct term $\Xi^{dir}_{vc\mathbf{k},v'c'\mathbf{k}'}$ results from the screened Coulomb interaction and dynamic screening effects $W(\mathbf{r},\mathbf{r}')$ while the exchange term $\Xi^{ex}_{vc\mathbf{k},v'c'\mathbf{k}'}$ results from the bare Coulomb interaction. It is obvious that the former describes the attractive part of the electron-hole

interactions while the latter represents the repulsive part. Their Fourier transform is given by [99]

$$\langle vc\mathbf{k}|\Xi^{dir}|v'c'\mathbf{k}'\rangle = -\frac{1}{\Omega}\sum_{\mathbf{G},\mathbf{G}'} W_{\mathbf{G}\mathbf{G}'}(\mathbf{q}) \times \langle v'\mathbf{k}'|e^{i(\mathbf{q}+\mathbf{G})\cdot\mathbf{r}}|v\mathbf{k}\rangle\langle c\mathbf{k}|e^{-i(\mathbf{q}+\mathbf{G}')\cdot\mathbf{r}}|c'\mathbf{k}'\rangle\delta_{\mathbf{q},\mathbf{k}'-\mathbf{k}}\,, \quad (7.7)$$

$$\langle vc\mathbf{k}|\Xi^{ex}|v'c'\mathbf{k}'\rangle = 2\times\frac{4\pi}{\Omega}\sum_{\mathbf{G}\neq 0}\frac{1}{|\mathbf{G}|^2}\langle c\mathbf{k}|e^{i\mathbf{G}\cdot\mathbf{r}}|v\mathbf{k}\rangle\langle v'\mathbf{k}'|e^{-i\mathbf{G}\cdot\mathbf{r}}|c'\mathbf{k}'\rangle\,, \quad (7.8)$$

where $W_{\mathbf{G}\mathbf{G}'}(\mathbf{q})$ is the Fourier transform of the screened Coulomb interaction and can be expressed in terms of the microscopic dielectric function $\varepsilon_{\mathbf{G}\mathbf{G}'}$,

$$W_{\mathbf{G}\mathbf{G}'}(\mathbf{q}) = \frac{4\pi\varepsilon^{-1}_{\mathbf{G}\mathbf{G}'}(\mathbf{q})}{|\mathbf{q}+\mathbf{G}||\mathbf{q}+\mathbf{G}'|}\,. \quad (7.9)$$

The microscopic dielectric function relates the longitudinal component of an external field to the longitudinal component of the total electric field. It can be obtained in terms of the irreducible polarizability $\chi^0_{\mathbf{G}\mathbf{G}'}$ given by

$$\epsilon_{\mathbf{G},\mathbf{G}'}(\mathbf{q},\omega) = \delta_{\mathbf{G},\mathbf{G}'} - \frac{4\pi}{|\mathbf{G}+\mathbf{q}||\mathbf{G}'+\mathbf{q}|}\chi^0_{\mathbf{G}\mathbf{G}'}(\mathbf{q},\omega)\,. \quad (7.10)$$

Via the Adler-Wiser formula [100, 101], $\chi^0_{\mathbf{G}\mathbf{G}'}$ is of the form given by

$$\chi^0_{\mathbf{G}\mathbf{G}'}(\mathbf{q},\omega) = \frac{1}{V}\sum_{\nu,\nu',\mathbf{k}}\frac{f_{\nu'\mathbf{k}+\mathbf{q}}-f_{\nu\mathbf{k}}}{E_{\nu\mathbf{k}}-E_{\nu'\mathbf{k}+\mathbf{q}}-\omega-i\eta}\langle\nu\mathbf{k}|e^{-i(\mathbf{q}+\mathbf{G})\cdot\mathbf{r}}|\nu'\mathbf{k}+\mathbf{q}\rangle\langle\nu'\mathbf{k}+\mathbf{q}|e^{i(\mathbf{q}+\mathbf{G}')\cdot\mathbf{r}}|\nu\mathbf{k}\rangle \quad (7.11)$$

Here $f_{\nu\mathbf{k}}$ is the Fermi distribution, η is a positive infinitesimal and V is the crystal volume. At zero temperature, $f_{\nu\mathbf{k}}$ can only be either 0 or 1. The transition matrix element is symmetric. Therefore, equation (7.11) can be reduced to [18]

$$\chi^0_{\mathbf{G}\mathbf{G}'}(\mathbf{q},\omega) = \frac{2}{V}\sum_{v,c,\mathbf{k}}\frac{1}{E_{c\mathbf{k}+\mathbf{q}}-E_{v\mathbf{k}}-\omega-i\eta}\langle v\mathbf{k}|e^{-i(\mathbf{q}+\mathbf{G})\cdot\mathbf{r}}|c\mathbf{k}+\mathbf{q}\rangle\langle c\mathbf{k}+\mathbf{q}|e^{i(\mathbf{q}+\mathbf{G}')\cdot\mathbf{r}}|v\mathbf{k}\rangle\,. \quad (7.12)$$

Note that this equation is only applicable to a systems with finite band gap. For systems with zero or negative band gap, one may set up a small energy cut to avoid the divergence.

Now the eigenfunction (7.4) can be solved to get the eigenvalues E_λ and the eigenvectors A^λ of the exciton. Then we can construct the $(\mathbf{G}=0,\mathbf{G}'=0)$ component of the response function [68]

$$\chi_{00}(\mathbf{q},\omega) = \frac{1}{V}\sum_{\lambda}\left|\sum_{vc\mathbf{k}}\langle v\mathbf{k}|e^{-i\mathbf{q}\cdot\mathbf{r}}|c\mathbf{k}\rangle A^\lambda_{vc\mathbf{k}}\right|^2\frac{1}{E^\lambda-\omega+i\eta}\,. \quad (7.13)$$

The macroscopic dielectric function can be calculated by [68]

$$\varepsilon_M(\omega) = 1 - \lim_{\mathbf{q}\to 0} v(q)\chi_{00}(\mathbf{q},\omega)\,. \tag{7.14}$$

One can evaluate the above equation to get the macroscopic dielectric function. Instead of doing it, people find that it is easy to evaluate the imaginary part of ε_M first while the real part can be computed by KramersCKronig relation. Using the identity,

$$Im\frac{1}{E^\lambda - \omega + i\eta} = -\pi\delta(E^\lambda - \omega)\,, \tag{7.15}$$

we obtain

$$\epsilon_2(\omega) = \lim_{\mathbf{q}\to 0}\ \frac{8\pi^2}{V\mathbf{q}^2}\sum_\lambda \left|\sum_{vc\mathbf{k}} \left\langle v\mathbf{k}\middle|e^{-i\mathbf{q}\cdot\mathbf{r}}\middle|c\mathbf{k}\right\rangle A^\lambda_{vc\mathbf{k}}\right|^2 \delta(E^\lambda - \omega)\,. \tag{7.16}$$

During the calculation, the matrix element $\left\langle v\mathbf{k}\middle|e^{-i\mathbf{q}\cdot\mathbf{r}}\middle|c\mathbf{k}\right\rangle$ appears many times and is very important. We should be very careful to evaluate it. According to $\mathbf{k}\cdot\mathbf{p}$ perturbation theory, we have the identity

$$\langle v\mathbf{k} \mid e^{-i\mathbf{q}\cdot\mathbf{r}} \mid c\mathbf{k}\rangle = \frac{1}{\epsilon^{QP}_{c,\mathbf{k}+\mathbf{q}} - \epsilon^{QP}_{v,\mathbf{k}}}\langle v\mathbf{k} \mid \mathbf{q}\cdot\mathbf{v} \mid c\mathbf{k}\rangle^{QP}. \tag{7.17}$$

at the limiting of vanishing $\mathbf{q}$. Similar to the TDDFT under mGGA, the transition matrix $\langle c\mathbf{k} \mid \mathbf{v} \mid v\mathbf{k}\rangle^{QP}$ should be approximated by Eq. (5.12). Since we're using mGGA in our computation, no scissor operator is required to get the correct band gap, so we can say that the quasiparticle(QP) wave functions are the same as KS mGGA orbitals. Therefore, we arrive at

$$\epsilon_2(\omega) = \frac{8\pi^2}{\Omega}\sum_\lambda \left|\sum_{vc\mathbf{k}} \frac{\left\langle v\mathbf{k}\middle|\hat{\mathbf{e}}\cdot\mathbf{v}\middle|c\mathbf{k}\right\rangle^{LDA}}{E^{LDA}_{c\mathbf{k}} - E^{LDA}_{v\mathbf{k}}} A^\lambda_{vc\mathbf{k}}\right|^2 \delta(E^\lambda - \omega)\,. \tag{7.18}$$

This work uses the Linear augmented Slater-type orbital method, developed by Davenport and co-workers [27–30], to solve the KS equations. LASTO was explained in Chapter 3.

To calculate the dielectric function, Eq. (7.18), we follow the implementation on the LAPW method [66] closely. Since the LASTO method is similar to the LAPW method except the difference in treatment of the interstital part, here we only list the interstitial contribution to the optical matrix elements $\left\langle v\mathbf{k}\middle|\hat{\mathbf{e}}\cdot\mathbf{p}\middle|c\mathbf{k}\right\rangle$

given by

$$I^{\mathbf{G}}_{NN'} = \sum_{ij} \widetilde{\phi}^{*}_{N\mathbf{k}}(\mathbf{K}_i)\widetilde{\phi}_{N'\mathbf{k}'}(\mathbf{K}_j)\widetilde{\Theta}(\mathbf{K}_i - \mathbf{K}_j + \mathbf{G}) \tag{7.19}$$

where $\widetilde{\Theta}(\mathbf{G})$ is the Fourier transform of the step function $\Theta(\mathbf{r})$.

7.3 Results and Discussion

In this section, absorption spectra of Si, GaAs obtained from the solution of the BSE will be shown. We compare our results with experimental data as well as with theoretical work recently appearing in the literature. During evaluating the dielectric function and the irreducible polarizability, the summation over $\mathbf{k}$ mesh needs to be done directly and broadened with an appropriate width η (eV). The Monkhorst-Pack special points scheme [61, 62] is used to generate $\mathbf{k}$ points in the Brillouin zone (BZ). $\mathbf{k}$ mesh shifted by an arbitrary vector is used through all calculation. However, the symmetry of $\mathbf{q}$ points will be same as the symmetry of unshifted $\mathbf{k}$ mesh since $\mathbf{q}$ must be equal to the difference between two $\mathbf{k}$ points because of momentum conservation. Besides of summation over $\mathbf{k}$ mesh in BZ, another summation over the reciprocal lattice vectors $\mathbf{G}$ must be cut off to save computational resource according to convergence. We found that for 10x10x10 $\mathbf{k}$-mesh with an arbitrary shift, Eq. (7.4) can be directly diagonalized, while for higher dense $\mathbf{k}$ mesh, the quasi-minimal residua (QMR) method [103] should be adopted to diagonalize it since the related matrix size is too large to diagonalize directly.

7.3.1 The spectra of Si

We calculated the spectra of Si using the 10x10x10 $\mathbf{k}$-mesh with an arbitrary shift $(0.1, 0.3, 0.5)\frac{2\pi}{a}$, and the parameters $N_{\mathbf{G}} = 59$, $N_v = 3$, $N_c = 4$, $N_{ce} = 20$. The spin-orbit interaction is not included. Fig. 7.1 shows the comparison of the BSE results, RPA results and experimental data. The calculated spectra are broadened by 0.15 eV. Similar to the TDDFT under mGGA, we computed the optical spectra by two ways. The first way used the momentum operator matrix to replace the transition matrix $\langle \nu\mathbf{k} \mid \mathbf{v} \mid \nu'\mathbf{k}\rangle^{QP}$ directly, called approximation I. The calculated absorption spectrum of Si is plotted by red solid line. Another way was to approximate the qusiparticle transition matrix by the LDA transtion matrix given by Eq. (5.12), called approximation II. The result computed by this way is plotted by olive solid line. The RPA spectrum is plotted by green solid line and the experimental data [70] by dashed line.

Comparing the spectra computed by the two ways, we can see that the spectrum computed by the

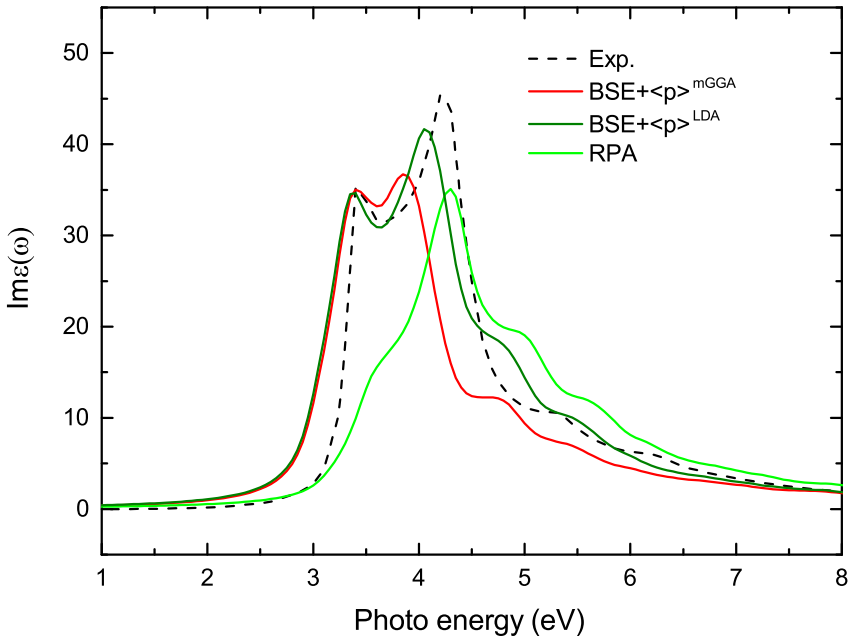

Figure 7.1: Calculated optical absorption spectra of Si with (red and olive solid lines) and without (green solid line) excitonic effects compared to the experimental data (black dashed line)

approximation II is much better. The E_1 peak of both results was enhanced more than twice as that of the RPA one, fitted to the experimental one through both the position and strength. It is noteworthy that the E_2 of approximation II was shifted more than the one of the approximation I and the strength is enhanced a little bit. The fine splittings on the peaks due to the spin-orbit(SO) interaction were mingled together because of no SO interaction included in the calculation. All these effects work together to make the resulting spectra agree better to the experimental data. The inclusion of the electron-hole interactions significantly improves the spectra.

For the notable discrepancy in the region the around the E_2 peak, we think it might be because the BSE approximation needs to be improved upon mGGA and the transition matrix elements needs to be directly evaluated (see Eq.(5.11)). Nonetheless, the inclusion of excitonic effects via BSE based on mGGA provides a crucial step forward in improving the optical spectra from the RPA level.

7.3.2 The spectra of Ge

We calculated the spectra of Ge using the 10x10x10 **k**-mesh with an arbitrary shift $(0.1, 0.3, 0.5)\frac{2\pi}{a}$, and the parameters $N_{\mathbf{G}} = 59$, $N_v = 3$, $N_c = 4$, $N_{ce} = 12$. The spin-orbit interaction is not included. Fig. 7.2

shows the comparison of the BSE results, RPA results and experimental data. The calculated spectra are broadened by 0.15 eV. The calculated absorption spectrum computed by approximation I is plotted by red solid line, the one from approximation II by olive solid line. The RPA spectrum is plotted by green solid line, and the experimental data [70] by dashed line.

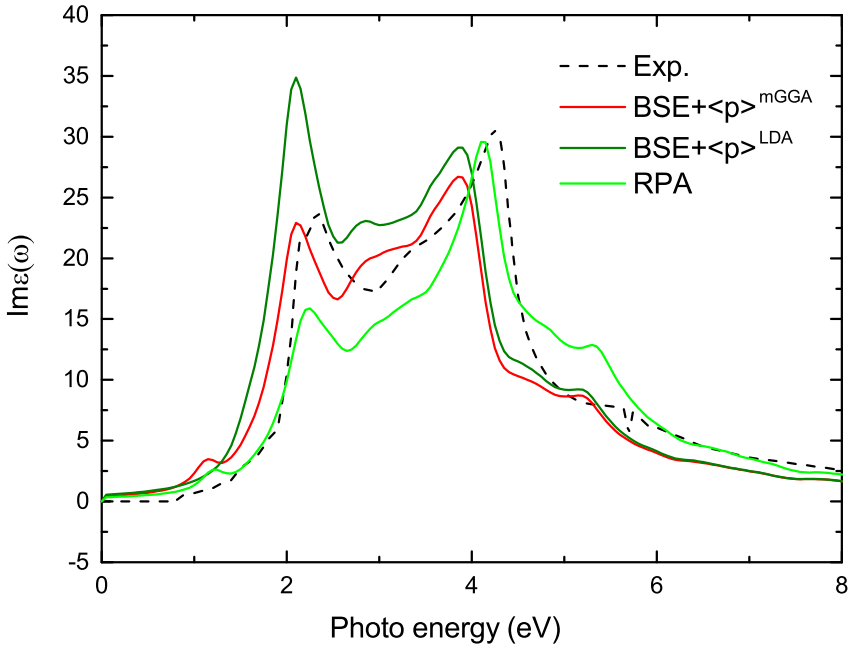

Figure 7.2: Calculated optical absorption spectra of Ge with (red and olive solid lines) and without (green solid line) excitonic effects compared to the experimental data (black dashed line)

Comparing the spectra computed by the two ways, we do see the improvement of the spectrum computed by the approximation II. Similar to the bulk Si case, we also see the enhancement of the position and the strength of the E_2 peak due to approximation II while the E_1 peak is overcorrected. This means that the oscillator strength is redistributed excessively between the E_1 and the E_2 peaks for BSE. As mentioned in Section7.3.1, we may need to improve mGGA and evaluate the transition matrix elements directly(see Eq.(5.11)).

7.3.3 The spectra of GaAs

We calculated the optical spectra of GaAs using the same 10x10x10 **k**-mesh as the one used by Si, and the parameters used are $N_{\mathbf{G}} = 65$, $N_v = 3$, $N_c = 4$, $N_{ce} = 20$. The spin-orbit interaction is not included, too. Figs. 7.3 shows the comparison of the BSE results, RPA results and experimental data

[70, 102]. The theoretical spectra are broadened by 0.15 eV. The calculated absorption spectrum computed by approximation I is plotted by red solid line, the one from approximation II by olive solid line. The RPA spectrum is plotted by green solid line, and the experimental data [70] by dashed line.

Compareing the spectra computed by the two ways, we do see the improvement of the spectrum computed by the approximation II. Similar to the bulk Si case, we also see the enhancement of the position and the strength of the E_2 peak due to approximation II while the E_1 peak is overcorrected. fitted to the experimental one through both the position and strength. The fine splittings on the peaks due to the spin-orbit interaction were mingled together because of no SO interaction included in the calculation. This means that the oscillator strength is redistributed excessively between the E_1 and the E_2 peaks for BSE. As mentioned in Section7.3.1, we may need to improve mGGA and evaluate the transition matrix elements directly(see Eq.(5.11)).

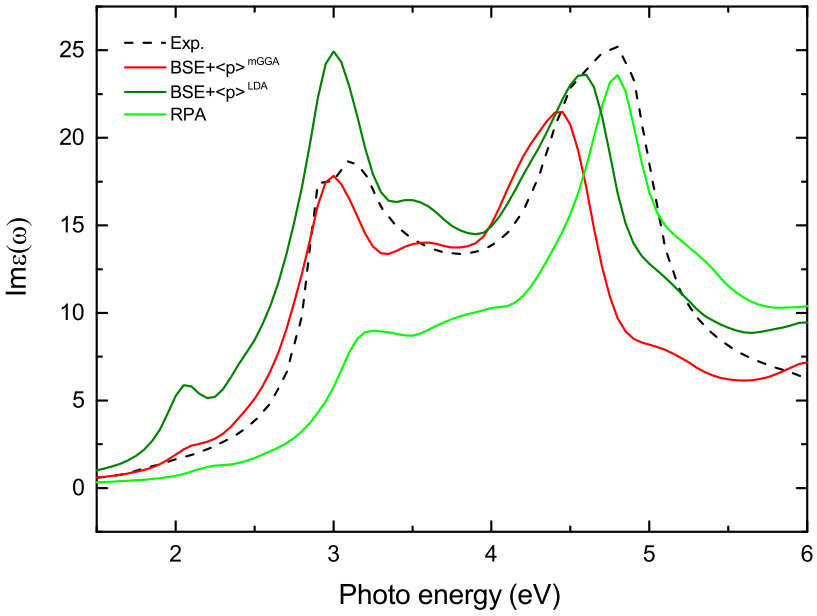

Figure 7.3: Calculated optical absorption spectra of GaAs with (red and olive solid lines) and without (green solid line) excitonic effects compared to the experimental data (black dashed line)

References

[1] R. Lam, M. Chen, E. Pierstorff, H. Huang, E. Osawa and D. Ho, ACS Nano 2, 2095(2008).

[2] C. W. Tang and S. A. VanSlyke, Appl. Phys. Lett. 51, 913 (1987).

[3] J. H. Burroughes, D. D. C. Bradley, A. R. Brown, R. N. Marks, K. Mackay, R. H. Friend, P. L. Burns and A. B. Holmes,Nature 347, 539(1990).

[4] N. S. Sariciftci, L. Smilowitz, A. J. Heeger, F. Wudl, Science 258, 1474(1992).

[5] J. J. M. Halls, C. A. Walsh, N. C. Greenham, E. A. Marseglia, R. H. Friend, S. C. Moratti and A. B. Holmes, Nature 376,498(1995).

[6] F. Garnier, G. Horowitz, X. Peng, D. Fichou, Adv. Mater. 2, 592(1990).

[7] F. Garnier, R. Hajlaoui, A. Yassar, P. Srivastava, Science 265, 1684(1994).

[8] P. Hohenberg and W. Kohn, Phys. Rev. 136, B864 (1964).

[9] W. Kohn and L. J. Sham, Phys. Rev. 140, A1133 (1965).

[10] D. C. Langreth and M. J. Mehl, Phys. Rev. B 28, 1809(1983).

[11] A. D. Becke, Phys. Rev. A 38, 3098 (1988).

[12] J. P. Perdew, J. A. Chevary, S. H. Vosko, K. A. Jackson, M. R. Pederson, D. J. Singh, and C. Fiolhais, Phys. Rev. B46, 6671 (1992); 48, 4978(E) (1993).

[13] A. D. Becke and E. R. Johnson, J. Chem. Phys. 124, 221101 (2006).

[14] F. Tran and P. Blaha, Phys. Rev. Lett. 102, 226401 (2009).

[15] T.V. Voorhis and G.E. Scuseria, J. Chem. Phys. 109, 400 (1998).

[16] J.P. Perdew, J. Tao, V.N. Staroverov and G.E. Scuseria, Phys. Rev. Lett. 91, 146401 (2003).

[17] J.P. Perdew, J. Tao, V.N. Staroverov and G.E. Scuseria, J. Chem. Phys. 120, 6898 (2004).

[18] M. S. Hybertsen and S. G. Louie, Phys. Rev. B 35, 5585 (1987).

[19] E. Runge and E. K. U. Gross, Phys. Rev. Lett. 52, 997 (1984).

[20] L.J. Sham and T.M. Rice, Phys. Rev. 144, 708 (1966).

[21] W. Hanke and L.J. Sham, Phys. Rev. B 12, 4501 (1975).

[22] W. Hanke, Adv. Phys. 27, 287 (1978).

[23] W. Hanke and L.J. Sham, Phys. Rev. Lett. 43, 387 (1979).

[24] W. Hanke and L.J. Sham, Phys. Rev. B 21, 4656 (1980).

[25] G. Strinati, Phys. Rev. Lett. 49, 1519 (1982).

[26] G. Strinati, Phys. Rev. B 29, 5718 (1984).

[27] Davenport, J.W. , Physical Review B 29, 2898(1984).

[28] Davenport, J.W., Weinert, M. and Watson, R.E., Physical Review B 32, 4876(1985).

[29] J. W. Davenport, R. E. Watson, and M. Weinert, Phys. Rev. B 32, 4883 (1985).

[30] Fernando, G.W., Davenport, J.W., Watson, R.E. and Weinert, M., Physical Review B 40, 2757(1989).

[31] T. L. Loucks, Augmented Plane Wave Method (Benjamin, New York, 1967); J. O. Dimmock, Solid State Physics (Academic, New York, 1971), Vol. 26.

[32] O.K. Andersen, Phys. Rev. B 12, 3060(1975).

[33] M. Born and J. R. Oppenheimer, Ann. Physik 84, 457(1927).

[34] D. R. Hartree,Proc. Cambridge Phil. Soc. 24, 89,111,426(1928).

[35] V. Fock, Z.Phys. 61, 126(1930).

[36] L.H. Thomas, Proc. Cambridge Phil. Roy. Soc. 23,542-548(1927).

[37] E.Fermi, Rend. Accad. Naz. Lincei 6, 602-607(1927).

[38] J. P. Perdew, Int. J. Quantum Chem. S19 497(1985).

[39] J. P. Perdew, Int. J. Quantum Chem. 30 451(1986).

[40] L. Hedin and B.I. Lundqvist, J. Phys. C 4, 2064 (1971).

[41] S.H. Vosko, L Wilk, and M. Nusair, Can. J. Phys. 58, 1200 (1980).

[42] D.M. Ceperley and B.J. Alder, Phys. Rev. Lett. 45, 566(1980).

[43] A.D. Becke and M.R. Roussel, Phys. Rev. A 39, 3761 (1989).

[44] J.P. Perdew and Y. Wang, Phys. Rev. B 45, 13244 (1992)

[45] P. Haas, F. Tran, and P. Blaha, Phys. Rev. B 79, 085104 (2009)

[46] P. Blaha, K. Schwarz, G. K. H. Madsen, D. Kvasnicka, and J. Luitz, WIEN2K: An Augmented Plane Wave and Local Orbitals Program for Calculating Crystal Properties, edited by K. Schwarz, Vienna University of Technology, Austria, 2001.

[47] Mascovic, D:R., Vukajlovic, F. R., Zekovic, S.: J. Phys. C 16, 6731(1983).

[48] Bludau, W., Onton, A., Heinke, W. J. Appl. Phys. 45, 1846(1974).

[49] Zwerdling, S., Lax, B., Roth, L. M., Button, K. J.: Phys. Rev. 114, 80(1959).

[50] Sell, D. D.: Phys. Rev. B6, 3750(1972).

[51] Varfolomeev, A. V., Seisyan, R. P., Yakimova, R. N.: Sov. Phys. Semicond. (English Transl.) 9, 530(1975); Fiz. Tekh. Poluprovodn. 9 (1975) 804.

[52] Mathieu, H., Chen, Y., Camassel, J., Allegre, J., Robertson, D. S.: Phys. Rev. B 32, 4042(1985).

[53] E. K. U. Gross and W. Kohn, Phys. Rev. Lett. 55, 2850 (1985).

[54] R. van Leeuwen, Phys. Rev. Lett. 72, 3863 (1999).

[55] G. Onida,L. Reining and A. Rubio, Rev. Mod. Phys.74,601(2002).

[56] A. Zangwill and P. Soven, Phys. Rev. Lett. 45, 204(1980); A. Zangwill, and P. Soven, Phys. Rev. B 24, 4121(1981).

[57] J. F. Dobson, Phys. Rev. Lett.73, 2244(1994).

[58] V.U. Nazarov and G. Vignale, Phys. Rev. Lett. 107, 216402(2011).

[59] J.C. Slater, Phys. Rev. 51, 846(1937).

[60] J.C. Slater, Phys. Rev. 36, 57(1930).

[61] H.J. Monkhorst and J.D. Pack, Phys. Rev. B 13, 5188(1976).

[62] H.J. Monkhorst and J.D. Pack, Phys. Rev. B 16, 1748(1977).

[63] L. X. Benedict, E. L. Shirley, and R. B. Bohn, Phys. Rev. B 57, R9385 (1998).

[64] M. Rohlfing and S. G. Louie, Phys. Rev. B 62, 4927 (2000).

[65] B. Arnaud and M. Alouani, Phys. Rev. B 63, 085208 (2001).

[66] P. Puschnig and C. Ambrosch-Draxl, Phys. Rev. B 66, 165105 (2002).

[67] H. Stoll, C.M.E. Pavlidou, and H. Preuss, Theor. Chim. Acta 49,143(1978).

[68] S. Albrecht, L. Reining, R. Del Sole, and G. Onida, Phys. Rev. Lett. 80, 4510 (1998).

[69] S. Albrecht, L. Reining, G. Onida, V. Olevano, and R. Del Sole, Phys. Rev. Lett. 83, 3971 (1999).

[70] D. E. Aspnes and A. A. Studna, Phys. Rev. B 27, 985 (1983).

[71] L. Geelhaar, R. A. Bartynski, F. Ren, M. Schnoes, and D. N. Buckley, J. Appl. Phys. 80, 3076 (1996).

[72] H. Shimizu, K. Kumada, N. Yamanaka, N. Iwai, T. Mukaihara, and A. Kasukawa, IEEE J. Quantum Electron. 36, 728 (2000).

[73] S. W. Park, C. K. Moon, J. C. Han, and J.-I. Song, IEEE Photonics Technol. Lett. 16, 1426 (2004).

[74] M. A. Remennyi, N. V. Zotova, S. A. Karandashev, B. A. Matveev, N. M. Stus, and G. N. Talalakin, Sens. Actuators B 91, 256(2003).

[75] Y. Qiu, D. Uhl, and S. Keo, Appl. Phys. Lett. 84, 263(2004).

[76] K. L. Averett, X. Wu, M. W. Koch, and G. W. Wick, J. Cryst. Growth 251, 852 (2003).

[77] N. Georgiev and T. Mozume, J. Appl. Phys. 89, 1064 (2001).

[78] H. Yoshida, T. Mozume, T. Nishimura, and O. Wada, Electron. Lett. 34, 913 (1998).

[79] T. J. Kim, T. H. Ghong, Y. D. Kim, S. J. Kim, D. E. Aspnes, T. Mori, T. Yao, and B. H. Koo, Phys. Rev. B 68, 115323 (2003).

[80] S. G. Choi, C. J. Palmstrøm, Y. D. Kim, D. E. Aspnes, H. J. Kim, and Y.-C. Chang, App. Phys. Lett. 91, 041917 (2007).

[81] Z.H. Levine and D.C. Allan, Phys. Rev. Lett. 63, 1719 (1989).

[82] Z.H. Levine and D.C. Allan,Phys. Rev. B 43, 4187 (1991).

[83] G. A. Baraff and M. Schlüter, Phys. Rev. 8 30, 3460 (1984).

[84] G. Stinati, H. J. Mattausch, and W. Hanke, Phys. Rev. Lett. 45, 290 (1980); Phys. Rev. B 25, 2867 (1982).

[85] M. S. Hybertsen and S. G. Louie, Phys. Rev. B 34, 5390(1986).

[86] R. W. Godby, M. Schlüter, and L. J. Sham, Phys. Rev. B 37, 10159 (1988).

[87] S. G. Choi et al., Applied Physics Letters 91, 041917 (2007).

[88] J. J. Yoon et al., Applied Physics Letters 92, 151907 (2008).

[89] T. J. Kim et al., Phys. Rev. B 68, 115323 (2003).

[90] T. J. Kim et al., Applied Physics Letters 95, 111902 (2009).

[91] L. Vegard, Zeitschrift fr Physik A Hadrons and Nuclei 5, 17 (1921).

[92] Landolt-Börnstein database,Group III Condensed Matter (Springer-Verlag, Berlin, 2006).

[93] B. Jobst, D. Hommel, U. Lunz, T. Gerhard, and G. Landwehr, Applied Physics Letters 69, 97 (1996).

[94] A. G. Thompson, M. Cardona, K. L. Shaklee, and J. C. Woolley, Phys. Rev. 146, 601 (1966).

[95] S. Larach, R. E. Shrader, and C. F. Stocker, Phys. Rev. 108, 587 (1957).

[96] J. A. Van Vechten and T. K. Bergstresser, Phys. Rev. B 1, 3351 (1970).

[97] J. E. Bernard and A. Zunger, Phys. Rev. B 36, 3199 (1987).

[98] L. Reining, V. Olevano, A. Rubio, and G. Onida, Phys. Rev. Lett. 88, 066404(2002).

[99] B. Arnaud,S. Lebègue and M. Alouani, Phys. Rev. B 71, 035308 (2005).

[100] S. L. Adler, Phys. Rev. 126, 413 (1962).

[101] N. Wiser, Phys. Rev. 129, 62 (1963).

[102] M. Garriga, M. Kelly, and K. Ploog, Thin Solid Films 233, 122 (1993).

[103] R. W. Freund and N. M. Nachtigal, Numerische Mathematik 60, 315 (1991).